Cloud shortwave spectral radiative properties: Airborne hyperspectral measurements and modeling of irradiance

by

Bruce C. Kindel

B.A., University of Colorado at Boulder, 1992

A thesis submitted to the

Faculty of the Graduate School of the

University of Colorado in partial fulfillment

of the requirements for the degree of

Doctor of Philosophy

Department of Atmospheric and Oceanic Sciences

2010

This thesis entitled:
Cloud shortwave spectral radiative properties: Airborne hyperspectral measurements and modeling of irradiance
written by Bruce C. Kindel
has been approved for the Department of Atmospheric and Oceanic Sciences

Peter Pilewskie

O. Brian Toon

Date

The final copy of this thesis has been examined by the signatories, and we find that both the content and the form meet acceptable presentation standards of scholarly work in the above mentioned discipline.

Kindel, Bruce C. (Ph.D.)

Cloud shortwave spectral radiative properties: Airborne hyperspectral measurements and modeling of irradiance

Thesis directed by Professor Peter Pilewskie

The design, construction, and performance of a solar spectral irradiance system for the National Center for the Atmospheric Research (NCAR) High Performance Instrumented Airborne Platform for Environmental Research (HIAPER) aircraft is described. The redesign of the integrating sphere baffling system used to for the measurement of solar irradiance is also described. The new baffle has improved the cosine response, reducing the error three-fold from the maximum error of the original design. Two aircraft studies from the Tropical Composition, Cloud and Climate Coupling Experiment (TC4) of cloud spectral (400-2100 nm) radiative properties are presented. Ice cloud single-scattering properties are validated with detailed radiative transfer modeling of ice cloud spectral albedo and aircraft measurements of the same. Liquid water cloud absorption is examined with spectrally resolved flux divergence (layer absorption) measurements of marine stratus clouds. Mie calculations of cloud single-scattering properties are combined with radiative transfer calculations predict spectral absorptance. Model results are compared with cloud absorptance derived from aircraft measurements. Model results illustrate the spectral dependence of cloud absorption on optical thickness, effective radius, and the absorbing aerosols. Spectral measurements demonstrate the dependence of integrated cloud absorption on varying water vapor amount. A novel technique for single aircraft measurements of flux divergence is described.

Dedication

To my family, for their support and good humor, especially Sara, who was a constant source of encouragement.

Acknowledgements

The work presented in this thesis were the results of close collaboration between groups from the University of Colorado, NCAR, and NASA Ames. I am grateful to the members of all of them. Peter Pilewskie and Sebastian Schmidt were involved with all aspects of the work and provided guidance and support throughout. Odele Coddington developed the radiative transfer model used in this thesis and patiently answered countless questions. Scott Kittelman constructed the integrating sphere baffles with great skill and meticulous workmanship. Patrick McBride, Yolanda Roberts and Samuel LeBlanc were always willing to help with a science or software question. Sara Martinez-Alonso was always available to answer an IDL question and helped with figures. Sam Hall from NCAR taught me about actinic flux measurements and integrating instruments on aircraft. The NCAR group also provided the calibration test facility where all of the integrating sphere testing was performed. Warren Gore from NASA Ames provided support during numerous field campaigns and helped with many aspects of the design of the spectral irradiance system for NCAR. Finally, lunches with Zoltan Sternovsky, Sebastian Schmidt, Patrick McBride, and Eike Bierwirth provided welcome daily relief, with conversations that usually included some combination of science, music, film, food, literature, or the latest soccer match. Over the years, I found that hour to be invaluable.

Contents

Chapter

1 Introduction 1

1.1 Airborne measurements of spectral irradiance 2

1.2 Design and development of the HIAPER Atmospheric Radiation Package (HARP) 4

1.3 Ice cloud measurements and modeling 6

1.4 Solar spectral absorption by marine stratus clouds 8

2 Design and Performance of HIAPER Atmospheric Radiation Package (HARP) Solar Spectral Irradiance System 11

2.1 HARP spectral irradiance calibration and noise characterization 15

2.2 Radiometric stability of HARP 16

2.3 HARP platform stabilization 19

2.4 Comparison of HARP measured and modeled zenith spectrum 25

3 Integrating sphere baffle design for improved cosine response. 28

3.1 Introduction 28

3.2 Integrating sphere design 31

3.3 Laboratory testing of sphere cosine response 33

3.4 Baffle construction 35

3.5 Monte Carlo modeling 36

3.6 Empirical testing of various baffle designs 39

3.7 An improved baffle design 42

3.8 Summary and conclusions 44

4 Observations and modeling of ice cloud shortwave spectral albedo during the Tropical Composition, Cloud and Climate Coupling Experiment 48

4.1 Introduction 49

4.2 Measurements of radiance and irradiance during TC^4 53

4.2.1 Solar Spectral Flux Radiometer (SSFR) 53

4.2.2 MODIS Airborne Simulator (MAS) 54

4.2.3 Radiative transfer calculations of irradiance 55

4.2.4 Ice particle single scattering models 57

4.3 Retrieval of optical thickness and effective radius from SSFR and MAS . 60

4.4 Analysis of spectral albedo properties 62

4.5 Comparison of irradiance and radiance derived optical properties 71

4.6 Summary 79

5 Solar spectral absorption by marine stratus clouds: Measurements and modeling 84

5.1 Introduction 85

5.2 The Solar Spectral Flux Radiometer 88

5.3 Marine stratus cases 89

5.4 Sampling strategy for cloud absorption measurements 91

5.4.1 Observations of cloud spectral absorptance 93

5.5 Radiative transfer modeling of cloud absorptance 96

5.5.1 Mie calculations of cloud droplet optical properties 98

5.6 Retrieval of cloud optical thickness and effective radius 101

5.7 Comparison of measured to modeled cloud spectral absorptance 103

5.8 Spectral cloud absorption with absorbing aerosol 110

5.9 Summary and conclusions 114

6 Summary and Outlook 117

Bibliography 120

Tables

Table

4.1 Summary of Optical Thickness and Effective Radius for the Four Cases. 76

Figures

Figure

2.1 A schematic of the Zeiss monolithic spectrometer is shown. 12

2.2 A computer rendering of the HARP irradiance system is shown. The tray is rack mounted in HIAPER and there are two trays for HARP, (one zenith, one nadir). The fiber optic carrying the light from the light collector to the spectrometers connects at the shutter. 14

2.3 On the left the comparison from the Optronic and Oriel standards of irradiance are plotted. The black line is the HARP irradiance spectrum of the Optronic standard calibrated by the Oriel standard. The red diamonds are the published Optronic values. On the right, the noise equivalent irradiance spectrum is plotted. 17

2.4 The ratio of the field calibration spectra taken at the beginning of PACDEX (26 April 2007) and the end of the experiment (25 May 2007) from the zenith instrument is shown. 20

2.5 A time series of aircraft roll data (black line) and several irradiance channels (various colors) are plotted. Note the stability of the irradiances despite the changes in roll of up to 5°. 22

2.6 For the same time period as Figure 2.5 the expected error if the platform had been fixed to the aircraft instead of stabilized is shown. 23

2.7 The same plot as Figure 2.6 with the percent deviation of the irradiance data from 1600 nm overplotted in blue. The green values are the predicted error after subtracting 5° from the fixed platform calculation. This is the expected error in irradiance when the aircraft exceeded 5° in roll, the range limit of the platform. 24

2.8 On the left an example HARP zenith spectrum from clear sky conditions at 12.5 km altitude is plotted in black and a model spectrum in red. On the right, the ratio spectrum of measurement and model is plotted. . . . 27

3.1 The schematic drawing of the integrating sphere based on the design of Crowther and then reduced in size for use on aircraft. 32

3.2 The layout of the cosine testing system is shown. The enclosures containing the swivel stage and bulb are painted ultra flat black to reduce scattered light. 34

3.3 The scaled down (flight) version cosine response of the original integrating sphere. 35

3.4 Plotted on the left panel are the measured and ZEMAX modeled cosine response of the integrating sphere based on the Crowther design and reduced in size for aircraft measurements. On the right is the ratio (model divided by measurement) of the integrating sphere responses. 38

3.5 A simple schematic drawing illustrates the cause of the hotspot. 40

3.6 Several designs tested to examine the effect of the baffle shape on the cosine response. In the lower right hand corner of each plot is a simple cross sectional view of the baffle shape. The cross hatching is meant to indicate the baffle was constructed from PTFE (Fluorilon-99W™). Specular cones were made from polished aluminum. 41

3.7 The narrow gap cone allows some light to pass the cone at normal incidence to the bottom of the sphere, scatter directly to the base of the cone, and into the fiber optic. 43

3.8 On the left panel the model predicted cosine response is plotted, on the right panel the laboratory measured response of the narrow gap cone is plotted. 45

3.9 A direct comparison of the original design and the narrow gap cone design is plotted on the left panel. On the right panel the is ratio (model divided by measured) of the two designs. 47

4.1 Phase functions of 870 nm from the C5 library for the largest (90μm, solid line) and smallest (10μm, dash-dot line)(right). Single-scattering albedo spectra for the largest (solid line) and the smallest (dash-dot) effective radii from the C5 library. 61

4.2 The results of the C5 library in the radiative transfer calculations of albedo spectra for three different effective radii and four different optical thicknesses. The spectra cluster by color (optical thickness) in the 400-1000 nm wavelength range, and by line style (effective radius) in the 1500-2150 nm wavelength range. 61

4.3 Two-dimensional representations of the μ=0.82 case (a) MAS radiance at 650 nm. (b) SSFR-measured albedo with wavelength on the x-axis. (c) Calculated albedo using optical thickness and effective radius retrieved from SSFR. (d) Difference image between Figures 4.3b and 4.3c. 64

4.4 A typical SSFR cloud albedo spectrum is plotted with the major water vapor band centers (940, 1140, 1400, and 1900 nm) overplotted with vertical lines. The approximate band widths are the shaded regions bounded by the dashed lines. 65

4.5 For each of the four cases the differences between modeled (C5) and measured albedo using optical thickness and effective radius derived from SSFR are shown. The black dots which aggregate to form lines are the differences for every line in the MAS flight track, and the red diamonds are the mean differences. 67

4.6 For cases μ=0.60 and μ=0.82 the highest and lowest optical thickness and effective radius albedo spectra are plotted with the full wavelength spectra as predicted from the single-scattering properties from C5 (red) and C4 (blue). Note the excellent agreement in all cases in the longer wavelengths. As the optical thickness increases, the agreement becomes worse in the shorter wavelengths and in the 1200-1300 nm range. 69

4.7 Same as Figure 4.6 but for the cases μ=0.88 and μ=0.92. 70

4.8 The MAS retrieval of optical thickness and effective radius are shown (μ=0.88) with the SSFR half-power point (circle) overplotted. 72

4.9 The time series of optical thickness and effective radius retrieved by SSFR (black) and MAS (red) are shown for the four cases. 73

4.10 For each of the four cases the differences between modeled (C5) and measured albedo using MAS-derived optical thickness and effective radius are shown. The black dots are the differences for every line in the MAS flight track, and the red diamonds are the mean differences. 77

4.11 Optical thickness and effective radius as retrieved by SSFR and MAS are plotted against each other as is the ratio from SSFR and MAS against optical thickness. The first row is μ=0.60, the second row μ=0.82, the third row μ=0.88, and the fourth row μ=0.92. 80

5.1 Images taken from the NASA DC-8 forward video camera above (a) and below (b) the marine stratus cloud deck encountered on 29 July 2007 during TC^4. 90

5.2 The mean (solid black lines) and ± one standard devaition (dashed red lines) SSFR albedo spectra are plotted for the two cases. The 06 August case was thinner and more heterogeneous, thus the higher variations in the measurements. 90

5.3 The mean (solid black lines) and ± one standard deviation (dashed red lines) SSFR absorptance spectra for the two cases are shown. 94

5.4 The mean (solid black lines) and ± one standard deviation (dashed red lines) for the absorptance (a) and albedo (b) for the 29 July case as measured by the ER-2. The DC-8 data were used for the under cloud measurements of absorptance. 97

5.5 The asymmetry parameter spectra (a) for the smallest and largest effective radii used in the modeling are plotted on the left. On the right (b) are single-scattering albedo spectra for the same sizes. 100

5.6 The range of modeled cloud absorptances due to the coupled effects of optical thickness and effective radius are shown. The absorptance for an effective radius of 5 μm and optical thickness of 5 and 100 are plotted on the left (a). The same plot but for and effective radius of 30 μm is shown on the right (b). 100

5.7 The mean SSFR albedo spectra are plotted (solid black line) for the 29 July (a) and 06 August (b) cases. The model albedo values for the 19 retrieval wavelengths are plotted with black circles. The retrieved optical thickness and effective radius is given in the upper right corner of each plot. 102

5.8 The SSFR measured absorptance spectra (solid black lines) and ± one standard deviation (dashed red lines) for the 29 July (a) and 06 August (b) are plotted. The results of the model predicted absorptance, using the optical thickness and effective radius retrieved from the albedo measurements, are plotted with diamonds. 105

5.9 The absorptance residual spectra (measurement minus model) are plotted for the two cases. The approximate band centers and widths of water vapor are shaded. The variation in shading indicates relative band absorption strength with stronger bands shaded more darkly. 106

5.10 The model absorbed irradiance for the 29 July is separated into its various components. Total cloud absorbed irradiance is plotted in (a). This is the identical spectrum to Figure 5.8(a) before normalization by the above cloud downwelling irradiance. The clear sky spectrum (b) is the model absorbed irradiance for the same atmospheric layer without a cloud. The enhanced gaseous absorbed irradiance is (c) and the cloud liquid water (d). The cloud spectrum (a) is the sum of (b), (c) and (d).. 109

5.11 The results of the 29 July cloud case with varying amounts of an absorbing aerosol embedded in the cloud. The six spectra correspond to the six aerosol optical thicknesses used in the model; the highest absorptance is for the largest aerosol optical thickness. 113

Chapter 1

Introduction

Clouds exert a strong influence on the Earth's albedo and thus have a profound effect on climate. Their influence on climate has been recognized for more than a century [*Abbot and Fowle*, 1908]. It is estimated that Earth's broadband planetary albedo, approximately 0.30 [*Wielicki et al.*, 1995], would be halved in the absence of clouds. The modification of radiation in the presence clouds depends on many factors including: cloud fraction and vertical distribution, thickness, thermodynamic phase, and particle size and shape. All of these influence the flow of solar and thermal radiation from the top of the atmosphere to the surface and back to space. Cloud radiative properties are the result of and an influence on atmospheric dynamical, thermodynamical, chemical, and hydrological processes. This coupling leads to a more difficult question and the one agreed upon as having the largest uncertainty in climate change: what is the role of cloud feedbacks in climate change ? (See, for example, *Stephens* [2005]; *Soden and Held* [2006]; *Bony et al.* [2006]) Temperature change in response to the increase of greenhouse gases will almost certainly impact all of the cloud properties listed above.

The focus of the work presented in this thesis is on airborne measurements of solar spectral irradiance and the associated detailed atmospheric radiative transfer calculations to address fundamental questions about cloud spectral radiative properties. Included in this is the further refinement of the measurement of solar spectral irradiance and measurement techniques that use spectral irradiance. The first topic is the design,

construction and testing of an airborne solar spectral irradiance system for the NCAR High-Performance Instrumented Airborne Platform for Environmental Research (HIAPER) Gulfstream V aircraft [*Laursen et al.*, 2006]. A substantial portion of this work focused on the improvement of the cosine response of the light collectors used to measure irradiance. The second topic was the validation of ice single-scattering properties from measurements of spectral ice cloud albedo made during the Composition, Cloud and Climate Coupling Experiment (TC^4) [*Toon et al.*, 2010]. The third topic was liquid water cloud solar spectral absorption measurements also made during TC^4. These are discussed further in the remainder of the introduction, following, a brief discussion on the unique role of airborne solar spectral irradiance measurements.

1.1 Airborne measurements of spectral irradiance

In the past decade, NASA Earth Observing System (EOS) satellites like the Moderate Resolution Imaging Spectroradiometer (MODIS) Terra and its follow-up MODIS Aqua have been used operationally for retrieving cloud properties, including: cloud height and temperature (and thus emission), cloud phase, and directly related to the work presented here, optical thickness and effective radius [*King et al.*, 1992, *Platnick et al.*, 2003]. Optical thickness, effective radius, and cloud particle thermodynamic phase, determine cloud spectral albedo and cloud absorption, two subjects examined in great depth in this thesis. Satellites provide the global spatial and temporal coverage necessary for climate studies that cannot be achieved by aircraft studies. However, there are limitations to satellite measurements that can only be addressed by aircraft. These limitations include the finite angular extent of radiance measurements that are necessitated by measurements from space and the limited spectral sampling for nearly all currently orbiting satellites. The fundamental unit of energy balance is irradiance (often called flux and, more accurately, flux density), a quantity that can be measured from aircraft but not by space-borne instruments. Airborne irradiance provides an important bridge

connecting the remote sensing measured quantity of radiance to the energetically important quantity irradiance. Comparisons of cloud properties derived from radiance and irradiance are made in chapter 3 of this thesis. Although there is no physical limitation on spectral sampling from satellites (such as there is with irradiance), currently, only HYPERION and SCHIAMACHY (Scanning Imaging Absorption spectrometer for Atmospheric CartographHY) provide solar reflected radiance data with contiguous spectral sampling. HYPERION is a land surface imaging instrument and SCHIAMACHY is used for the retrieval of atmospheric trace gases. Neither of these hyperspectral instruments routinely measure cloud properties although studies are currently being undertaken using SCHIAMACHY for cloud and surface properties in the Arctic [Y. Roberts, personal communication, 2010].

During TC^4, the Solar Spectral Flux Radiometer (SSFR) and the MODIS Airborne Simulator (MAS) were flown on the high altitude NASA ER-2 aircraft. The MAS instrument, a discrete wavelength, multispectral imager provided a proxy to the measurements made by the space-borne MODIS Terra and Aqua instruments. The algorithms for the retrieval of cloud optical thickness and effective radius were identical for MAS and MODIS. While there was substantial effort in coordinating aircraft with MODIS satellite overpasses during TC^4, these opportunities were limited to usually only one per flight [M. D. King, personal communication, 2010]. Aircraft greatly expanded the number and conditions (e.g. cloud type, solar geometry, aerosol loading, etc) of cases that could be examined. Additionally, aircraft can follow the development of clouds through the course of a day with a high sampling rate and provide vertically resolved measurements of radiation. It is through field campaigns like TC^4, with aircraft equipped to make measurements of in situ cloud properties, multispectral radiance, and hyperspectral irradiance, that we validate global scale satellite retrievals of cloud radiative properties. Satellite retrievals are used to produce cloud climatologies e.g. *Schiffer and Rossow* [1983] and the single-scattering properties validated from field campaigns like TC^4 are

used for the parameterization of cloud optical properties for climate modeling e.g. *Fu* [2007], *Hong et al.* [2009].

Lastly, the measurement of cloud flux divergence (cloud layer absorption) requires irradiance measurements above and below a cloud layer, observations that cannot be achieved from satellites. It is only with aircraft observations that direct measurement of cloud absorption can be made. It is only through spectrally resolved measurements, such as the ones presented in this thesis, that the mechanisms of absorption can be delineated.

1.2 Design and development of the HIAPER Atmospheric Radiation Package (HARP)

The development of the HARP system was a collaborative effort between the NCAR Atmospheric Radiation Investigation and Measurement (ARIM) group who specialize in actinic flux measurements and the Atmospheric Radiation Group (ARG) at the University of Colorado, experts in hyperspectral solar irradiance measurements. The design and performance of the solar irradiance component of the HARP system is the subject of Chapter 2. The construction of HARP system included a substantial effort to address the largest source of error in the measurement of spectral irradiance, the cosine response of the light collector. This is the topic of Chapter 3.

The following is a general discussion of the sources of error when making spectral irradiance measurements and provides the motivation and context for the light collector cosine response work. This is not an exhaustive study of error sources, but an overview of known errors and their quantification. With HARP, as with any scientific instrument, improving precision and accuracy are constant goals.

The errors were dominated by four sources. The first two sources were the radiometric precision of spectrometers and the accuracy of the absolute radiometric calibration. Here precision is defined to be a measure of the repeatability of the measurements,

equivalent to noise. The relative precision is quantified by the inverse of the signal-to-noise-ratio (SNR) of an instrument. A related quantity to the precision and relative precision is the repeatability over a longer time, in the case of an airborne field mission, one to two months. This is the instrument stability. The accuracy is determined from the absolute radiometric calibration. It was realized in the laboratory with a NIST-traceable irradiance standard (1000 W quartz-halogen lamp). This produced the conversion factor to go from digital number (DN) output by the spectrometer to physical units of irradiance (e.g. W $m^{-2}nm^{-1}$). Radiometric accuracy required high spectrometer precision. The third error source was due to the aircraft attitude during flight. Irradiance is defined with respect to a horizontal plane. Non-level aircraft flight produced by turns, ascents, descents, and turbulence, if uncompensated for, introduce error into the measurement of irradiance. The last error was produced by non-ideal cosine response by the light collectors.

The precision and absolute radiometric calibration of the spectrometers were dependent on: the manufacturer (Zeiss Optics for the work presented here) for a high SNR spectrometer; the quality of the NIST-traceable irradiance standard; the ability to reliably transfer the calibration in the laboratory; and ultimately NIST for the accuracy of the absolute values of irradiance. The absolute radiometric calibration from two calibration standards and power supplies from separate vendors were compared and the results are discussed in Chapter 2. The agreement was generally within 1 to 2% between the two vendors in wavelength intervals where the SNR is high. This is similar to the NIST-published 1% uncertainty for absolute irradiance in the visible wavelength range. In the near-infrared the NIST quoted uncertainties were 2-3%. The SNR of the Zeiss spectrometers used in the HARP system were on the order of one thousand, less than 1% error measurement-to-measurement. Field calibration of from several field experiments has demonstrated radiometric stability to the 1-2% level over the course of several weeks.

For light collectors mounted on a fixed platform, the data must be corrected or

filtered with the aircraft navigation data for periods of non-level flight. For low solar elevation angle, departures from level flight of 5° produce errors as large as 50% in zenith direct solar beam irradiance. Filtering was not an ideal solution to non-level flight because it introduces some unknown error from offsets between the aircraft navigation data and true level flight for the light collector. Moreover, filtering results in the loss of data. The error produced by non-level flight has been successfully mitigated with the use of a stabilized platform [*Wendisch et al.*, 2001]. A stabilized platform for the irradiance light collector was constructed [*Franke and Schell*, 2007] and tested to compensate for aircraft attitude deviations for the HARP system. In Chapter 2, the results from aircraft testing of the stabilization system are presented that show that the HARP stabilization system successfully corrected for departures from level flight of up to 5°.

The error due to non-ideal cosine response of the light collector, an integrating sphere, was the largest current source of error in the measurement of solar spectral irradiance. The design of the integrating sphere originally used for solar spectral irradiance measurements deviated from ideal cosine by as much as 15-20% at some angles. Although a large amount of the error due to non-ideal cosine response can be removed in post processing, a direct avoidance of the error by improving the geometrical design of the light collector is preferred.

The errors in radiometric precision and accuracy are small, and the errors in non-level flight while potentially large, have been solved with platform stabilization. The largest remaining error source was in the non-ideal cosine response of the integrating spheres. The redesign of the integrating sphere baffle to improve the cosine response is the topic of Chapter 3.

1.3 Ice cloud measurements and modeling

A substantial focus of the TC^4 experiment was on the outflow of tropical convective systems [*Toon et al.*, 2010]. Accordingly, many of the flight hours for the DC-8 and ER-

2 aircraft (both flying SSFR systems) were spent sampling the cirrus (ice cloud) anvils that are ubiquitous in the tropics as a result of strong convection. Cirrus clouds, which cover 20-30% of the Earth, are an important component of the Earth's radiation budget and were identified by *Hartmann et al.* [1992] as having one of the largest impacts on top of the atmosphere radiative fluxes. The impact of cirrus clouds on radiation has two effects: solar radiation is reflected back to space by cirrus clouds which can cool the atmosphere and surface below; conversely, ice clouds absorb and emit thermal radiation and because they are at a lower temperature than the surface, they can warm.

The cloud thickness, temperature, ice crystal shape, and size distribution all contribute to the the magnitudes of heating and cooling. Of these factors, cloud microphysics, including ice particle single-scattering properties are perhaps the least well understood. The role of clouds in the Earth's radiative balance depends on the accurate representation of cloud single-scattering properties, namely the single-scattering albedo and the scattering phase function, both of which are wavelength dependent. For liquid water clouds, the shape of the particle is spherical and the theory (Lorenz-Mie) to calculate the scattering and absorption of liquid water spheres is exact and has been available since the publication of Mie's seminal work more than 100 years ago [*Mie*, 1908]. Ice particle shape is far more complicated. Ice particles display a myriad of shapes and sizes due to temperature and supersaturation conditions during formation as well as collision and coalescence after formation [*Lynch*, 2002]. These shapes are categorized into a small number of idealized shapes representative of variety of shapes observed when sampling cirrus clouds in situ.

The theoretical calculation of the phase function and single scattering albedo for non-spherical particles such as ice is accomplished through a variety of numerical techniques and is an area of active research [*Yang and Liou*, 1998]. Previous studies that assumed "equivalent" spheres have been shown to give poor results because the strongly forward-peaked phase function could not be reproduced, resulting in erroneously low

albedo [*Takano and Liou*, 1989]. The current computational techniques to derive ice crystal single-scattering properties include: geometric optics (for particles large compared to the wavelength of radiation), finite-difference time domain (FDTD), T-matrix, and the improved geometric optics method (IGOM). Additionally, the various shapes and sizes found in ice clouds must be modeled with representative mixtures of shape types and sizes [*Baum et al.*, 2005]. The wavelength dependent phase functions and single-scattering albedoes from commonly used single-scattering ice cloud libraries were used in the radiative transfer modeling to construct cloud spectral albedo presented in Chapter 4 of this thesis. These single-scattering properties were tested against observed hyperspectral irradiance for a number of cases encountered during TC^4 to determine how well they model the spectral ice cloud spectral albedo from both MAS derived optical thickness and effective radius and from SSFR derived quantities of the same.

1.4 Solar spectral absorption by marine stratus clouds

Absorption of solar radiation is the principal energy source that drives, dynamical, thermodynamical, and photo-chemical atmospheric processes on Earth. It is a quantity that is not directly observable from satellites alone. It must be inferred from a combination of satellite and ground based instruments, derived from aircraft measurements, or estimated from models.

Estimates made from the Earth Radiation Budget Experiment (ERBE) satellite from five years of data showed that the annually and globally average solar absorption (expressed as a percentage of the incident top-of-the-atmosphere solar irradiance) as 24.3% in the atmosphere and 46% at the surface [*Li and Leighton*, 1993]. These values have been updated by *Trenberth et al.* [2009], to 23% absorbed in the atmosphere and 47% absorbed at the surface. The Earth's albedo, about 30%, is well constrained by satellite measurements [*Wielicki et al.*, 1995]. It is the partitioning between atmospheric and surface absorption that is most difficult to constrain because both satellite, in situ,

and surface measurements are required. Surface observations are lacking over the oceans and are difficult to combine with satellite measurements. Historically, GCMs have given atmospheric absorption values that are low relative to measured values. This bias, too much downwelling solar irradiance at the surface, has been reduced with the inclusion of aerosols and updated water vapor spectroscopy into GCMs but has not been completely resolved [*Wild et al.*, 2006, *Wild*, 2008].

Cloud absorption has been invoked as an explanation for some of the bias when comparing surface irradiance measurements to model predicted irradiance [*Wild*, 2008]. The controversy surrounding cloud absorption began with the first attempts at direct measurements from aircraft [*Fritz and MacDonald*, 1951]. The controversy resurfaced in the middle part of the 1990s with a series of papers claiming more absorption of solar radiation by clouds than in models, the so called anomalous absorption (e.g. *Cess et al.* [1995], *Ramanathan et al.* [1995]). If clouds absorbed substantially more than is predicted by theory, this would alter considerably our understanding of climate. The results from a GCM indicate that cloud absorption, of the magnitude reported in the mid 1990s, would result in a reduction in Hadley circulation, a lessening of surface winds in the tropics, and a reduction (25 W m^{-2}) in surface latent heat flux [*Kiehl et al.*, 1995].

The source of difficulty in deriving cloud absorption stems from several factors. First among them is cloud heterogeneity. To accurately determine cloud absorption from vertical flux divergence derived from aircraft measurements of net irradiance, requires that the net horizontal divergence is zero. A homogenous, semi-infinite cloud layer satisfies this requirement. However, clouds are always inhomogeneous and finite in extent. The vast range in cloud type exhibits a similarly large range in cloud morphology. Marine stratus are perhaps the closest to the idealized plane-parallel, horizontally homogeneous cloud type and thus represent the best case for flux divergence. These low level, liquid water clouds are large in horizontal extent and as homogenous a cloud system that exists.

Another difficulty in making these measurements is the absolute radiometric calibration of the radiometers or, in the cases presented in this thesis, the spectrometers. Cloud flux divergence is the small difference of four larger quantities. An accurate measurement requires not only spectrometers that have high precision, but also that the absolute radiometric calibration is identical or near identical for all (four) instruments.

In Chapter 5, spectrally resolved measurements of absorption in large tropical marine stratus systems encountered during TC^4 is presented. These are compared with the calculated absorption from a state-of-the-art radiative transfer code combined with Mie calculations of liquid water cloud optical properties. The advantage of single aircraft measurements is demonstrated, as are the advantages of making spectrally resolved measurements in distinguishing and quantifying the mechanisms of absorption in clouds.

Chapter 2

Design and Performance of HIAPER Atmospheric Radiation Package (HARP) Solar Spectral Irradiance System

The design of the spectral irradiance component of HIAPER Atmospheric Radiation Package (HARP) closely followed the design of the Solar Spectral Flux Radiometer (SSFR) developed at NASA Ames [*Pilewskie et al.*, 2003]. For spectrometer hardware, both the NASA Ames group and the NCAR group had independently arrived at the same solution, the Zeiss monolithic spectrometer, for making measurements of irradiance and actinic flux.

The Zeiss spectrometer consisted of a fixed grating and detector array encased in a solid housing (Figure 2.1). All parts were cemented to the body of the spectrometer which produces a robust instrument in terms of its spectral and radiometric stability and low scattered light. The detector arrays were thermoelectrically cooled and order sorting filters were placed on top of the detector arrays to remove diffracted higher order light. To cover the solar spectrum, the HARP spectral irradiance system was comprised of two Zeiss spectrometers, a visible-near infrared (VIS-NIR) 1024 element silicon diode array instrument that nominally measured in the wavelength range 260 to 1090 nm, and the PGS (NIR) 256 element InGaAs array spectrometer that measured 903 to 2217 nm. The absolute wavelength accuracy was <0.5 nm and was reproducible to <0.1 nm for VIS-NIR. For the NIR, the wavelength accuracy was $\pm$ 0.6 nm. The stray light was 0.1% for both spectrometers. In the VIS-NIR the spectrometer had sampling resolution of

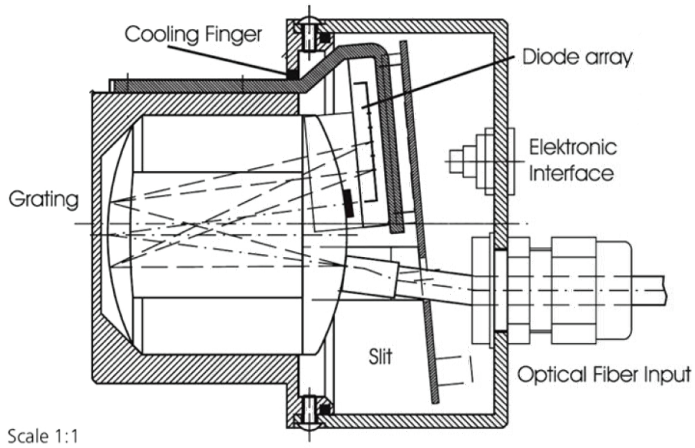

Figure 2.1: A schematic of the Zeiss monolithic spectrometer is shown.

0.8 nm and a spectral resolution, as defined by its full-width-at-half-maximum (FWHM), of ≈3 nm. The NIR spectrometer had sampling resolution of ≈5 nm and a FWHM of ≈16 nm. The technical specifications of wavelength resolution, accuracy, stability, and stray light rejection were published values from Zeiss. The values of resolution and wavelength accuracy were tested and found to be accurate with measurements of a low pressure mercury line source. The stray light rejection value has also been independently verified [P. Pilewskie, personal communication, 2010].

The HARP spectrometers were contained in two separate boxes each with its own signal electronics. The signal was digitized by a 16 bit analog-to-digital converter from -32768 to 32768 in digital number (DN). Each spectrometer was controlled by its own PC-104 stack that includes a 700 MHz computer running Windows XP and an IRIG-B card to acquire highly accurate (GPS) times from the aircraft navigational system. Computer and software control of the irradiance system were written in Labview to make it compatible with the National Center for Atmospheric Research (NCAR) Atmospheric Radiation Investigation and Measurement (ARIM) group's design for spectral actinic flux, the other radiative quantity measured by HARP. The controlling software allowed

for the complete control of the spectrometer (e.g sampling rate, integration times, dark current sampling, and shutter control).

The system included a shutter that opened and closed periodically to measure the dark current. During flight operation the shutter was closed every five minutes for a period of 30 seconds to record dark current data. These dark current spectra were linearly interpolated over the periods between the dark current measurements before subtraction from the irradiance spectra. Past performance of the SSFR and the Short Wave Spectrometer (SWS) systems, which used similar spectrometers, indicated the NIR dark current was sensitive to external fluctuations of temperature. For this reason extensive thermal testing of the spectrometers was performed using the NCAR thermal chamber. From these data, it was decided to place two thermistors inside the spectrometer housing to measure the ambient air temperature and spectrometer casing external temperature. These measurements will be used to refine the dark current interpolated values.

Attached to the shutter was 15 m fiber optic (low OH for transmission in the NIR water bands) bundle connected to a cosine-response optical collector (integrating sphere). The light collector was mounted to the exterior of the HIAPER aircraft. The optical collector is the subject of the next chapter. Figure 2.2 is a computer rendering of spectral irradiance spectrometers and computer stacks with each of the components labeled.

The spectral irradiance measurement system on HARP consisted of four spectrometers, two VIS-NIR and NIR pairs to measure both the downwelling irradiance (zenith system) and the upwelling irradiance (nadir system). The two systems were synchronized with the aircraft IRIG-B signal to start recording at the beginning of every second. Although the nominal sampling rate was one hertz, some drift was noted. Based on laboratory and field tests, the integration time for the VIS-NIR spectrometer was set at 400 ms and the NIR at 300 ms to optimize their full dynamic ranges. These were the longest integration times obtainable and thus they provided the greatest signal-to-

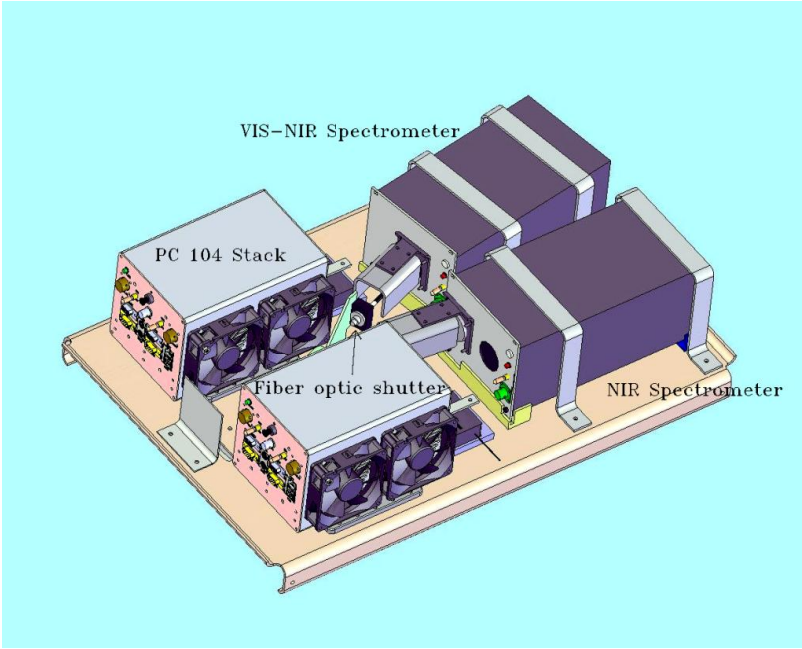

Figure 2.2: A computer rendering of the HARP irradiance system is shown. The tray is rack mounted in HIAPER and there are two trays for HARP, (one zenith, one nadir). The fiber optic carrying the light from the light collector to the spectrometers connects at the shutter.

noise ratios (SNR) while maintaining one hertz sampling and avoiding saturation from the field radiometric calibration unit. Each spectrum was time stamped and thermistor temperatures were recorded along with the raw uncalibrated spectral irradiance. Zenith and nadir spectra were matched according to their time stamps in post-processing of the data to produce, for instance, albedo spectra.

2.1 HARP spectral irradiance calibration and noise characterization

Prior to integration on the aircraft, the system was calibrated to physical units of spectral irradiance (W m^{-2} nm^{-1}), the so-called primary calibration. The calibration system consisted of highly stable power supplies, standards of spectral irradiance, and a mounting jig for alignment of the irradiance standard and HARP light collectors. The NCAR-ARIM calibration facility had calibration units (power supplies and irradiance standards) from Oriel and Optronic Laboratories. The standards of irradiance were 1000 W (tungsten-halogen lamp) NIST-traceable lamps with vendor-provided values of spectral irradiance for a specified power input and distance from the standard to the light collector. The standard of irradiance was aligned with the light collector and placed 50 cm apart. Both the zenith and nadir HARP systems were calibrated with each calibration system. Values for the eighteen published wavelengths from Oriel or Optronic Laboratories were interpolated using a NIST recommended interpolation technique [*Walker et al.*, 1987] to the HARP wavelengths.

In Figure 2.3 shows the results from some of these calibrations. Plotted in the left panel, the continuous line is the irradiance spectrum of the Optronic standard as measured by HARP zenith spectrometer system calibrated by the Oriel standard. Overplotted with red diamonds are the published values of the Optronic standard at selected wavelengths. The level of agreement (better than 1% at 500 nm and 1.5% at 1540 nm) was as good as or better than the NIST spectral irradiance scale uncertainties: 1% in the

visible and 3% at 2000 nm. The precision of the spectrometers was better than 1% when measured in the laboratory and was 1-2% during the course of a field campaign. Thus, the precision of the HARP measurements was better than the accuracy. It also indicates that we were able to transfer the calibration from the standards to the instrument in a highly repeatable manner. This did not preclude systematic errors but they would seem to be unlikely as the geometry was straightforward. Of course, these results were from testing only two standards; firmer conclusions would require the testing of several standards.

Another important metric of spectrometer performance, the noise equivalent radiance, was derived from the primary calibration. This is defined as the radiance required to change the signal by an amount equal to the noise, that is, to generate a signal-to-noise ratio of one. Because our primary measurement was irradiance, we altered the definition to noise equivalent irradiance and note that the two are simply related by the constant π. In Figure 2.3 in the panel on the right, we can see that SNR was substantially reduced at the wavelength extremes of the VIS-NIR spectrometer and at the longest wavelengths of the NIR spectrometer. This is also evident in the plot of the primary standards (left panel) as the spectrum became noisy near 350 nm, 1000 nm and 2200 nm. The performance of the NIR spectrometer was considerably better where the two spectrometers overlapped (not surprisingly because the FWHM was more than five times larger) at 900-1100 nm. For this reason, despite the coarser spectral resolution, a decision was made to use the NIR data in the majority of the overlap region for the final data product.

2.2 Radiometric stability of HARP

The first flight deployment of the HARP system took place from April to May of 2007 for the PACific Dust EXperiment (PACDEX) [*Stith et al.*, 2009]. PACDEX was a Langrangian type experiment to track dust and black carbon aerosols from their origins

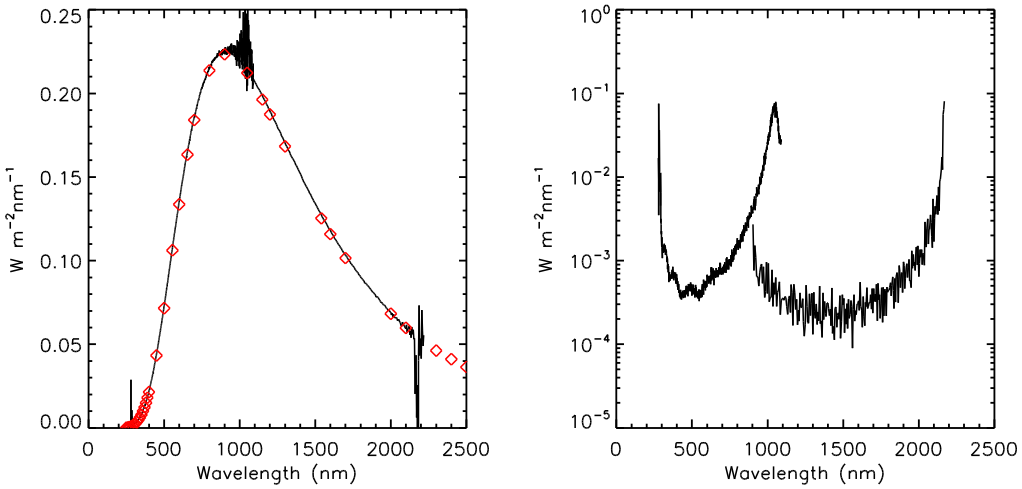

Figure 2.3: On the left the comparison from the Optronic and Oriel standards of irradiance are plotted. The black line is the HARP irradiance spectrum of the Optronic standard calibrated by the Oriel standard. The red diamonds are the published Optronic values. On the right, the noise equivalent irradiance spectrum is plotted.

in Asia across the Pacific Ocean to North America. The HIAPER aircraft flew a total of 115 hours and collected nearly one million spectra, providing a rigorous test of the radiometric stability of the HARP spectral irradiance system. During any field experiment, frequent radiometric calibration is essential to insure that the instrument is functioning properly and to track possible response degradation over the course of an experiment. Previous measurements with spectrometers of this type have shown that during the course of several weeks of a field experiment the spectrometers have maintained their calibration within 1-2% of the primary calibration. However, unexpected changes in the radiometric calibration are occasionally encountered and need to be identified as quickly as possible during a field experiment.

This was done during PACDEX with a portable field calibration unit. The field calibration unit consisted of three stable 250 W tungsten halogen lamps and a power source similar to those used in the laboratory for the primary calibration. In the laboratory these field lamps were measured by the HARP system at the time that the primary calibrations were made, which served to transfer the calibration from the primary standard to the field standards. Three field standards were used to provide redundancy and thus distinguish between changes in the HARP system from changes in the field standards themselves.

During PACDEX the field calibration unit was attached to the aircraft over the light collectors and field calibration measurements were collected to determine the radiometric stability of the HARP system. For the duration of PACDEX, field radiometric calibrations were undertaken as frequently as logistics allowed. If time and circumstances allowed, each spectrometer system (zenith and nadir) were calibrated with all three standards. During PACDEX the zenith system was calibrated four times and the nadir system nine times. In most cases however, time only allowed for one or at most, two field standards to be used. Figure 2.4 shows, the ratio of zenith spectrometer response for two calibrations, one made at the beginning of the experiment and the other

at the conclusion. The results are as expected, with the ratio over most of the spectral range falling within 1-2% of unity. Noisy data at the extreme wavelength ranges of the spectrometers were not included in the final data product. A calibration performed at the midpoint of the experiment (not shown) also falls within this range. Note that the deviations in NIR around 1400 nm and 1900 nm are due to changes in the water vapor path within the calibration unit.

2.3 HARP platform stabilization

One particularly challenging aspect of making irradiance measurements on moving aircraft arises from the changing attitude of the radiometric reference area. Aircraft flight is frequently non-level. Data from light collectors fixed- mounted to aircraft must be filtered or the data must be corrected for attitude deviations from level flight but there is uncertainty associated with these procedures. The preferred solution to this problem is to avoid post-processing filtering or correction by using a stabilized platform that actively compensates for the roll and pitch changes during flight [*Wendisch et al.*, 2001].

Two stabilized platforms for the, zenith and nadir light collectors were designed and constructed by Enviscope Inc. specifically for the HIAPER aircraft [*Franke and Schell*, 2007]. The stabilized platform contained two stacked goniometers and servo motors to drive them. The goniometers were orthogonal to each other with; one compensating for changes in roll, the other for changes in pitch. The changes in attitude of the aircraft were measured by an Inertial Navigation System (INS) mounted to the base of the HARP instrument rack. The system included static inclinometers attached to the platforms that determined the level point offsets between the INS and the platforms while the aircraft was on the ground. The INS was corrected with GPS for drift inherent in these systems. Corrections to aircraft attitude deviations from level flight by the stabilized platform were made 400 times per second [D. Schnell, personal communication, 2010].

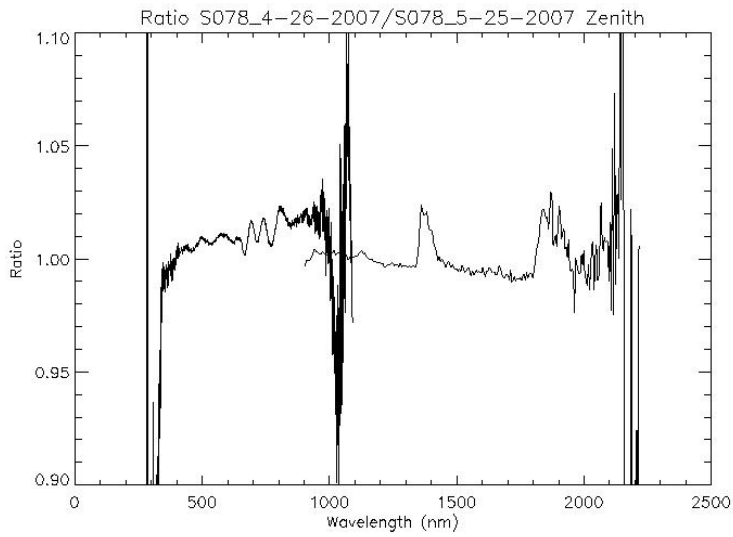

Figure 2.4: The ratio of the field calibration spectra taken at the beginning of PACDEX (26 April 2007) and the end of the experiment (25 May 2007) from the zenith instrument is shown.

The HARP stabilized platform with the HARP irradiance spectrometers were integrated on the HIAPER aircraft twice for testing, during the HIAPER Evaluation Flight Testing 2008 (HEFT 2008) experiment and the HEFT 2010 experiment. The stabilized platform was not completed in time for PACDEX. During the HEFT 2008 experiment a problem with the communication timing between aircraft GPS and the HARP INS was discovered. This problem seriously degraded the accuracy and reliability of stabilization. After HEFT 2008 it was decided to incorporate a GPS receiver directly into the HARP INS, instead of relaying the GPS signal from the aircraft to the INS. Several software upgrades to the INS software as recommended by the manufacturer were also done. These improvements were tested during the HEFT 2010 experiment and some of the results are presented below.

A flight period with cloud-free conditions above the aircraft and low solar elevations was identified from the HEFT 2010 experiment. Low solar elevation zenith data were used because small changes in aircraft attitude produce much larger relative changes in irradiance than for overhead Sun. Three plots from one such case are shown in Figures 2.5, 2.6, and 2.7. The top plot shows a time series of several HARP irradiance channels while flying under clear skies and at a solar elevation angle of 9°. The black line shows the roll data for the same time period. The limit switches used to regulate the maximum angular deviation that the platform could maintain were set to ± 5° in both pitch and roll. It is evident from Figure 2.5 that the time series of irradiance was stable to within 3%, especially in the longer wavelengths (e.g. 1600 nm) where the signal is almost entirely due to the directly transmitted solar irradiance and the atmosphere's optical thickness is small. The small variations in the irradiance time series may be the result of changes in the atmosphere and not related to the instrument attitude; at this level of variability the two cannot be unambiguously separated.

The expected change in irradiance due strictly to attitude deviation has been calculated. These are shown in Figure 2.6 and 2.7. In Figure 2.6 the expected percentage

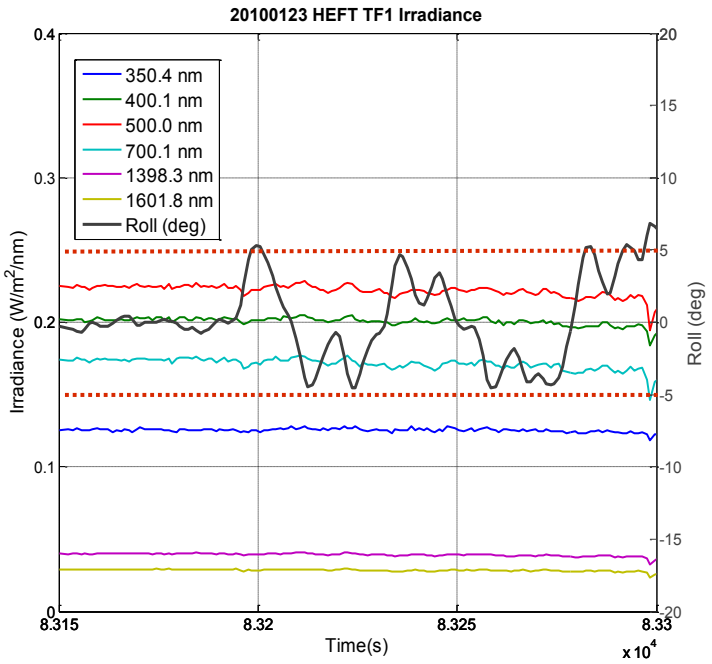

Figure 2.5: A time series of aircraft roll data (black line) and several irradiance channels (various colors) are plotted. Note the stability of the irradiances despite the changes in roll of up to 5°.

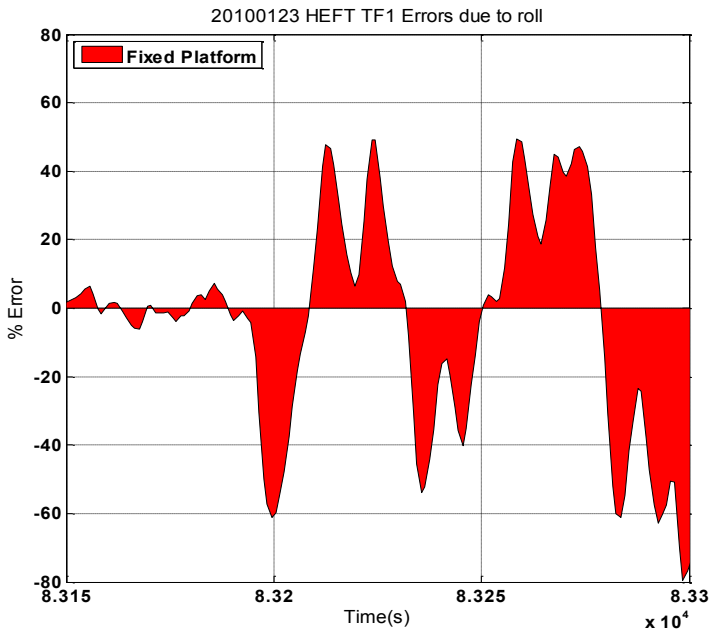

Figure 2.6: For the same time period as Figure 2.5 the expected error if the platform had been fixed to the aircraft instead of stabilized is shown.

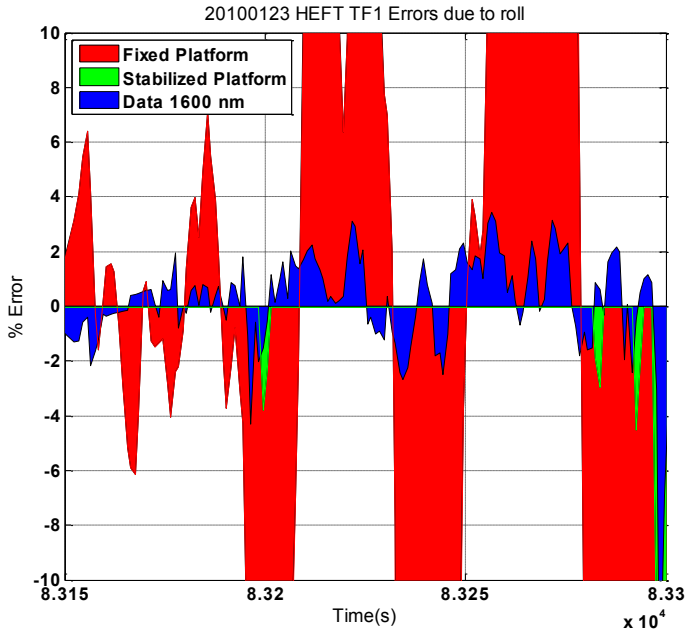

Figure 2.7: The same plot as Figure 2.6 with the percent deviation of the irradiance data from 1600 nm overplotted in blue. The green values are the predicted error after subtracting 5° from the fixed platform calculation. This is the expected error in irradiance when the aircraft exceeded 5° in roll, the range limit of the platform.

error due to changes in attitude are plotted. These are the errors from cosine response, that would be expected to occur for a fixed platform. In the Figure 2.7 the same plot as Figure 2.6 is shown together with irradiance time series at 1600 nm in blue. To create the deviation from the expected irradiance, a line was fit over the time range shown in the plot and the deviation from the line was calculated. Note that the deviation from the expected value has been reduced to the 2-4% level even for attitude changes of 5° which, at this solar elevation angle, would change the irradiance by as much as 50%. The green line is the calculated deviation from a fixed platform after subtracting 5° from the roll data. This is the expected error after the stabilized platform has reached the limits of its range of motion.

2.4 Comparison of HARP measured and modeled zenith spectrum

An additional check of the performance of the HARP spectral irradiance system was made by comparing a zenith-viewing irradiance spectrum from high altitude flight legs to a computed spectrum from a radiative transfer model. (The details of the model are presented in Chapters 4 and 5.). The downwelling irradiance (zenith viewing) was chosen because at high altitude, it is expected be the most straightforward case to model. At 12.5 km the downwelling irradiance contains little water vapor absorption (the main absorber over solar wavelengths), the underlying surface albedo has little effect on the signal, and the molecular scattering is only 14% of that at the surface. All that was required of the model was that it properly account for some molecular scattering and absorption by oxygen, carbon dioxide, and ozone. Perhaps most importantly, this provided the most direct comparison of the absolute radiometric calibration realized in the laboratory compared to the model top of the atmosphere (TOA) solar spectrum, a boundary condition for radiative transfer models. The TOA solar spectrum used in the model was that from *Kurucz* [1992].

In Figure 2.8 a single spectrum from HARP is plotted on the left. On the right

are spectra of the HARP irradiance and the predicted solar spectral irradiance from the radiative transfer model in red for a solar zenith angle of 62.2°. The agreement is generally in the 1-2% range in ranges where the spectrometers have good SNR. The HARP spectral resolution has been degraded by convolution to the slit function of a lower resolution spectrometer for which this model was developed; a higher resolution band model (new k-distribution) will be developed in the future for use with the HARP system. Also notable was the spectral registration as indicated by the agreement in the assorted Fraunhofer lines as well as the oxygen-A band (762 nm).

This model-measurement comparison completed the characterization of the HARP spectral irradiance system prior to the final delivery of the HARP system to NCAR. The known errors from all the sources (spectrometer, absolute calibration, radiometric stability, and stabilized platform) discussed up to this point were generally in the 1-3% range. The errors from non-ideal cosine response of the light collector can introduce additional uncertainty. The redesign of the light collector to reduce these errors is the subject of the next chapter.

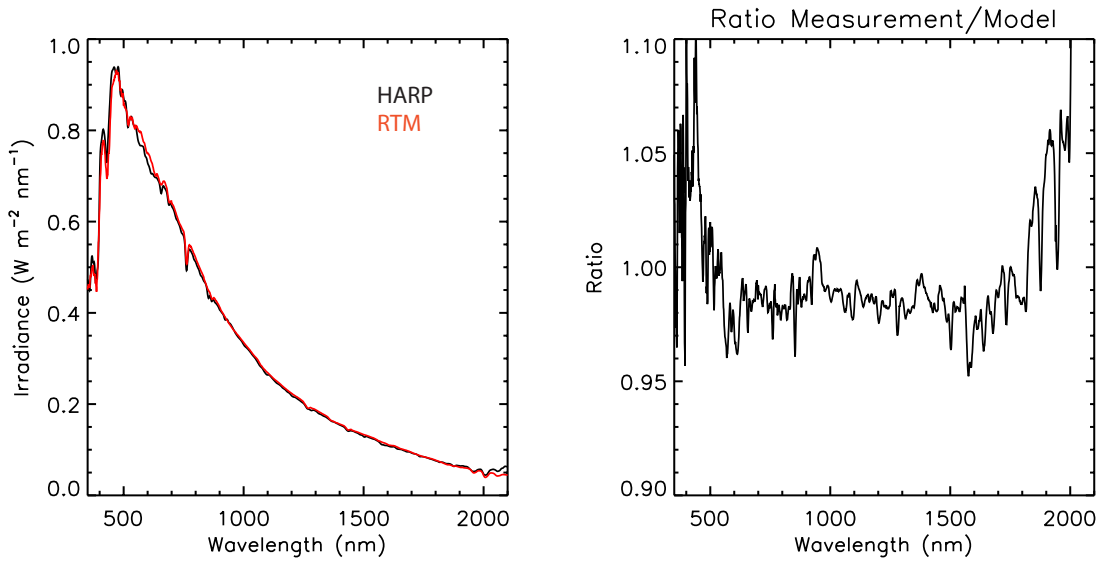

Figure 2.8: On the left an example HARP zenith spectrum from clear sky conditions at 12.5 km altitude is plotted in black and a model spectrum in red. On the right, the ratio spectrum of measurement and model is plotted.

Chapter 3

Integrating sphere baffle design for improved cosine response.

3.1 Introduction

The accurate measurement of solar spectral irradiance, the hemispherically integrated rate of radiative energy transfer in a direction normal to a plane surface (sometimes called total or global irradiance) requires that incoming radiation is properly weighted by the cosine of the incidence angle by means of an appropriately designed light collecting device. The "cosine response" of an instrument is the angular weighting function of the light collector. In practice, cosine response of instruments that utilize spectrometers to make spectrally resolved measurements of irradiance has been achieved utilizing three different methods: a transmissive diffusing material (for example, frosted glass or plastic), an isotropically scattering (Lambertian) diffuser panel, or an integrating sphere coated or constructed with a highly reflective material.

Transmissive diffusers have shown very good cosine response over a range of incidence angles for wavelengths in the visible to very near infrared (<1000 nm) [*Harrison et al.*, 1994, *Murrow et al.*, 1994]. Beyond 1000 nm the cosine response becomes poor at various wavelengths for many diffusive materials. For example, Teflon, a plastic occasionally used for transmissive diffusers, contains strong absorption features in the 2200 to 2500 nm wavelength range that degrade the signal. Frosted glass or opal also exhibits poor cosine response in the near-infrared. [A. F. H. Goetz, personal communication, 2010]. Additionally, the cosine response for transmissive diffusers is poor at large angles

from normal incidence [*Michalsky et al.*, 2003]. Transmissive diffusers may also exhibit polarization sensitivity [*Born and Wolf*, 1999].

Diffuser panels, made of highly reflective, near-Lambertian materials, viewed by a fiber optic or optical inlet also exhibit good cosine response over the range of solar wavelengths [*de la Casiniere et al.*, 1995, *Biggar et al.*, 1994]. However, the fiber optic bundle obscures some portion of the radiation field. The deviation of the panel from a perfect Lambertian reflector, its bidirectional reflectance factor, is characterized in the laboratory [*Jackson et al.*, 1992] and deviations from cosine can be corrected, at least for the directly transmitted component of downward solar irradiance. The diffuse component of solar radiation cannot be corrected because its angular distribution is rarely known. This is true for all three types of cosine collectors: no irradiance measurement can be perfectly corrected for the non-ideal cosine response even with laboratory characterization of the light collector. Thus, for the most accurate measurements of solar spectral irradiance the angular response of the cosine receptor should be as close to ideal over the wide range of wavelengths in the solar spectrum as is possible.

Integrating spheres constructed with highly reflective interiors have also been used as cosine-response light receptors. Perhaps the greatest advantage of integrating spheres is that the cosine response is generally invariant with respect to wavelength. Integrating spheres with near ideal cosine response, $<1\%$ error, have been constructed but have very low throughput ($\approx 0.01\%$) [*Budde*, 1964] requiring a photomultiplier tube detector (essentially, a photon counter). This low level of throughput is unacceptable for the measurements made by current aircraft spectrometers.

Previous work on spectral measurements of solar irradiance with integrating spheres has focused exclusively on measurements made at stationary ground sites. These were used, for example, in vicarious calibration of satellites [*Slater et al.*, 1996, *Biggar et al.*, 1994, *Thome et al.*, 1997]. More recently, measurements of solar spectral irradiance have been made on a variety of aircraft for energy budget studies [*Pilewskie et al.*, 2003],

cloud and aerosol remote sensing [*Coddington et al.*, 2010, *Kindel et al.*, 2010, *Schmidt et al.*, 2009] and surface spectral albedo studies [*Coddington et al.*, 2008]. The use of cosine collectors on aircraft imposes restrictions on the design and type of cosine collectors. Transmissive diffusers have been used in the past on aircraft and for surface measurements [*Pilewskie et al.*, 1998, 2003, *Rabbette and Pilewskie*, 2002], but because of the poor cosine response at low solar elevation angles have fallen out of favor. The use of a reflecting panel on aircraft is not practical; thus, integrating spheres have become the most frequent cosine collector of choice for aircraft measurements of solar spectral irradiance [*Pilewskie et al.*, 2003, *Bierwirth*, 2008].

The current integrating sphere design used for aircraft measurements is based on a design by *Crowther* [1997] and was intended for stationary surface measurements. This design was subsequently reduced in size for use on aircraft [*Pilewskie et al.*, 2003]. The original sphere exhibited non-ideal cosine response over a narrow range of incident angles. In particular, the design exhibited larger than ideal cosine response, a "hotspot", at zenith incidence angles between 20 and 25° [*Crowther et al.*, 1997, *Crowther*, 1997]. This same hotspot was also observed with the miniaturized sphere design for use on aircraft. This chapter describes an improvement to the cosine response of the *Crowther* [1997] design, chiefly through modification of the primary light baffle of the flight version of the sphere.

This investigation consists of three main parts: the empirical testing of some simple baffle shapes and surfaces, Monte Carlo modeling of various sphere baffle designs to predict the cosine response, and the fabrication and laboratory testing of the most promising modeled designs. The design changes consisted of changing the shape, size, and position of the baffle. Some additional experiments with specular baffles were also undertaken. This chapter describes the integrating sphere general design, the Monte Carlo modeling, results from laboratory tests of the various designs, a new design that substantially reduces the hotspot, and a summary and outlook for future work.

3.2 Integrating sphere design

The integrating sphere design first proposed by *Crowther* [1997] consisted of an entrance aperture at the top of the sphere, a conical baffle located near the center of the sphere, the principal axis of which was aligned with the center of the entrance aperture, and an exit aperture located at the bottom of the sphere, 180° from the entrance aperture. A simple schematic of the basic elements of the flight sphere are shown in Figure 3.1 along with the dimensions which are scaled to the original *Crowther* [1997] design. The exit aperture allows for the placement of a fiber optic to connect the integrating sphere to the aircraft rack-mounted spectroradiometer which may be several meters away from the integrating sphere. The field-of-view (FOV) of the fiber optic (25° full angle) is filled by the base of the conical baffle, preventing photons entering the fiber optic directly from the entrance aperture. In the work originally describing this design several baffle types were investigated using a Monte Carlo photon tracing model, developed specifically to address the sphere cosine response problem [*Crowther*, 1996]. A conical baffle, placed near the center of the sphere was found to be the best of the different types investigated. This design meets the critical requirement of azimuthally independent response. This limited the baffle shapes investigated to those with azimuthal symmetry, e.g. cones, spheres, hemispheres, cylinders, etc.

The *Crowther* [1997] sphere had an inner diameter of 10.16 cm, and entrance aperture of 2.54 cm, a conical baffle with a base diameter of 3.22 cm and a height of 3.81 cm. These dimensions were reduced to 37.5% of its original size for mounting on aircraft, resulting in a sphere with a diameter of 3.81 cm (Figure 3.1). The sphere is capped by a water-free quartz dome. For the remainder of this chapter the *Crowther* [1997] design, adapted for flight for use with the Solar Spectral Flux Radiometer (SSFR) will be simply referred to as the integrating sphere unless otherwise noted.

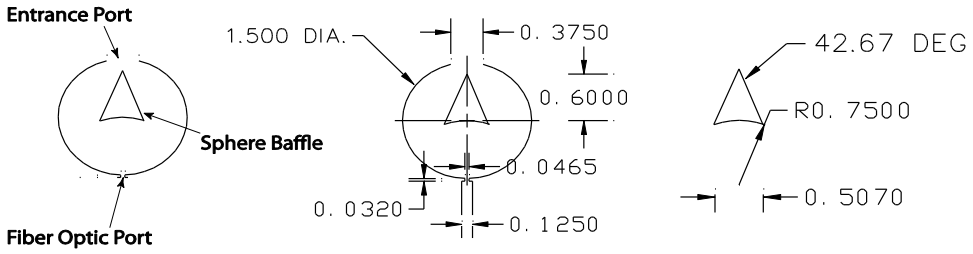

Figure 3.1: The schematic drawing of the integrating sphere based on the design of Crowther and then reduced in size for use on aircraft.

3.3 Laboratory testing of sphere cosine response

The laboratory testing of the cosine response of the integrating sphere employed a 1000 Watt quartz-halogen lamp powered by a highly stable power source. This is the same type of lamp used for absolute radiometric calibration but without NIST traceable calibration which is unnecessary for the relative measurements described here. The integrating sphere was mounted to a swivel stage that rotated through the range of angles from normal incidence (0°) to the horizon (90°). For this study measurements were made every five degrees from 0 to 85° eighteen angles in total. Both the source and the integrating sphere were in an enclosure with an ultra flat black interior to reduce error from scattered light. Figure 3.2 shows the design of the angular testing apparatus. The spectroradiometer used for the measurement of angular response was the same one used on aircraft missions, the Solar Spectral Flux Radiometer (SSFR). The instrument measured in the wavelength range from 350 to 2200 nm. The spectral resolution as measured full-width-half-maximum (FWHM) from a line source was 8 nm from 350 to 1000 nm with 3 nm sampling and 12 nm FWHM from 1000 to 2200 nm with 4.5 nm sampling. The SSFR recorded a complete spectrum every second. For this study 25 spectra were recorded at each angle of incidence and these spectra were averaged to enhance signal-to-noise ratio (SNR). The precision of the instrument, from measurement to measurement (second to second), was better than 0.1%. For a more complete description of the SSFR instrument see *Pilewskie et al.* [2003].

A typical result from a cosine response test is shown in Figure 3.3, at 550 nm. The response exhibited a substantial deviation from ideal cosine, with a maximum of approximately 17%, at incidence angles between 20-25° (0.94-0.90 in cosine of incidence angle). The angular response was calculated by normalizing the measured signal at each of the eighteen angles by the signal at normal incidence. Thus, the cosine response is identically one (ideal) at normal incidence for all designs. The hotspot was described in

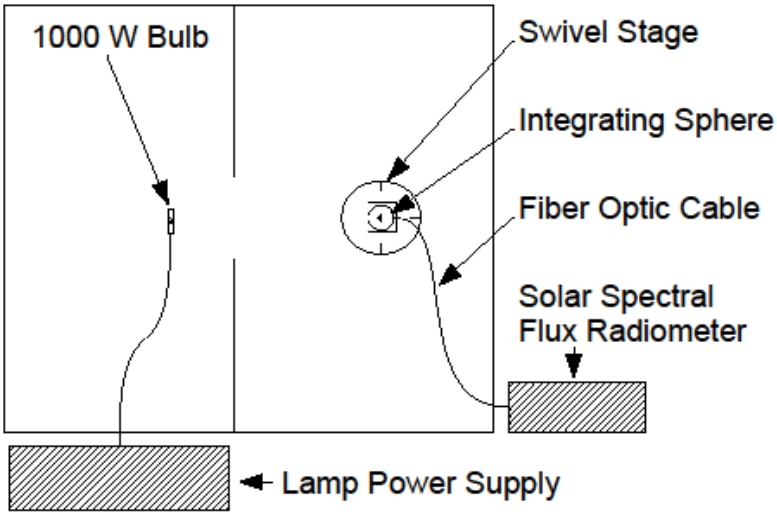

Figure 3.2: The layout of the cosine testing system is shown. The enclosures containing the swivel stage and bulb are painted ultra flat black to reduce scattered light.

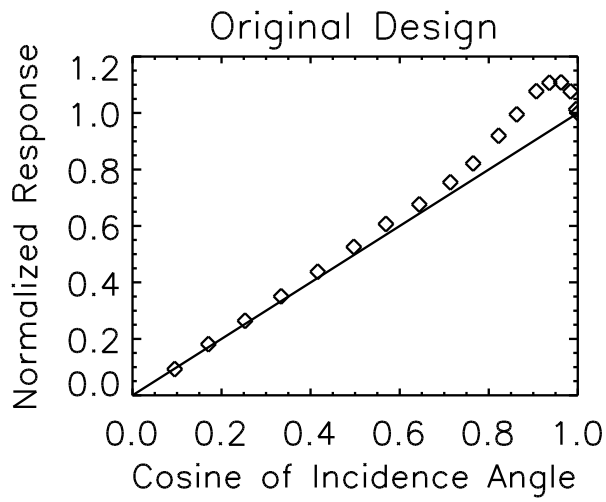

Figure 3.3: The scaled down (flight) version cosine response of the original integrating sphere.

the work on the original design although the magnitude was not as great, approximately 10%. It appears that the reduction in size of the *Crowther* [1997] design to flight size amplified the deviation from ideal cosine. Additionally, the measurement of several spheres of the same design indicates that there was some variation in the response which was most likely due to differences in sphere construction.

3.4 Baffle construction

The light scattering surfaces of the integrating sphere were constructed with a sintered polytetrafluoroethylene (PTFE) that goes under the commercial brand names, Spectralon® and Fluorilon-99W™ These materials are highly reflective, with reflectance of 99% or greater for wavelengths less than 1500 nm and greater than 95% reflectance for wavelengths throughout the spectral range of the SSFR. The high reflectance of PTFE and similar materials is essential for integrating spheres because even small changes in reflectance result in large changes of sphere throughput. The high order of multiple scattering in an integrating sphere amplifies absorption. Sintered PTFE is durable and does

not flake off like some coatings (for example, barium sulfate), a desirable feature in the vibrational environment during aircraft flight. Importantly, PTFE can be machined to create the sphere and various baffle designs. When machining this material, meticulous cleaning of the tools was done. Although hydrophobic, PTFE readily absorbs grease and oil which can degrade its optical scattering properties. In the original design, the baffle was held in place with four thin aluminum arms that were coated with barium sulfate, a highly reflective paint over the spectral range of the SSFR. For the purposes of the evaluation of new designs in the laboratory environment a single or double (uncoated) arm was used. This simplified and accelerated the construction-through-testing phase of the process. The best designs were later tested with all four arms.

3.5 Monte Carlo modeling

To guide the development of baffle design, the commercially available optical ray tracing program ZEMAX [*Zemax*, 2009] was used. Although closed form solutions to sphere throughput without internal baffling have been developed [*Goebel*, 1967], there is no such formulation for the angular response of a sphere with a baffle [*Crowther*, 1996]. For this reason, the approach in designing the sphere baffle was to construct a Monte Carlo model [*Crowther*, 1996]. The non-sequential ray tracing function of the ZEMAX software featured a similar Monte Carlo type simulation [*Zemax*, 2009]. Photons were traced throughout the sphere from the entrance aperture to their loss, either through absorption, exit back through the entrance aperture, or their contribution to the signal via their transit through the exit aperture (i.e. the fiber optic). The first step in the modeling process was to reproduce the cosine response of the current sphere design.

The ZEMAX model layout was an idealized version of the SSFR sphere containing a photon source, entrance aperture, conical baffle, and detector placed where the ferrule of the fiber optic bundle is located in the sphere. The dimensions of the sphere components between the SSFR sphere and the modeled sphere are identical. The model was

initialized with 10^7 photons and the angular response was modeled over the identical eighteen incidence angles that are measured in the lab - from 0 to 85° in five degree increments. The number of photons was identical (10^7) for each angle and the results were scaled by the cosine of the incidence angle after completing the calculation. The precision of the calculation using 10^7 photons was approximately 0.5%, estimated from repeated simulations of the same (original) sphere configuration. Figure 3.4 contains the results of the measured SSFR sphere and the ZEMAX model results of the same sphere. The model is able to reproduce the angular position and less accurately, the magnitude of the hotspot observed in laboratory. With the good agreement between the measured baffle and sphere response and the model of angular response ZEMAX could be trusted as a general guide to design new baffles in an effort to improve the cosine response.

The model simulations showed that the position of the hotspot was produced by photons with a large enough incidence angle (greater than 20°) to bypass the conical baffle and intersect the sphere near the bottom of the lower hemisphere. These photons are scattered to the base of the baffle and enter the fiber optic, thus undergoing only two scattering events before exit. All other angles of incidence require higher order scattering before entering the fiber optic because they either encounter the baffle first or intersect the sphere wall high enough that they cannot be directly scattered to the fiber optic. This is illustrated in Figure 3.5. The hotspot corresponds roughly to half angle of the conical baffle, 21.3°. This problem and its explanation, was included in the work describing the design of the sphere [*Crowther*, 1997]. The reason for this larger deviation from ideal cosine for the SSFR sphere is unknown. It may be related to the reduction in size of the sphere. Both the ZEMAX and the *Crowther* [1997] Monte Carlo model used in the original design of the sphere reproduced the hotspot at the same angles and both models under predicted the amplitude of the hotspot. Modeling errors may have resulted from several idealizations assumed in the model which included perfect Lambertian scattering by the PTFE, perfect sphere edges, and zero transmission through the baffle, even near

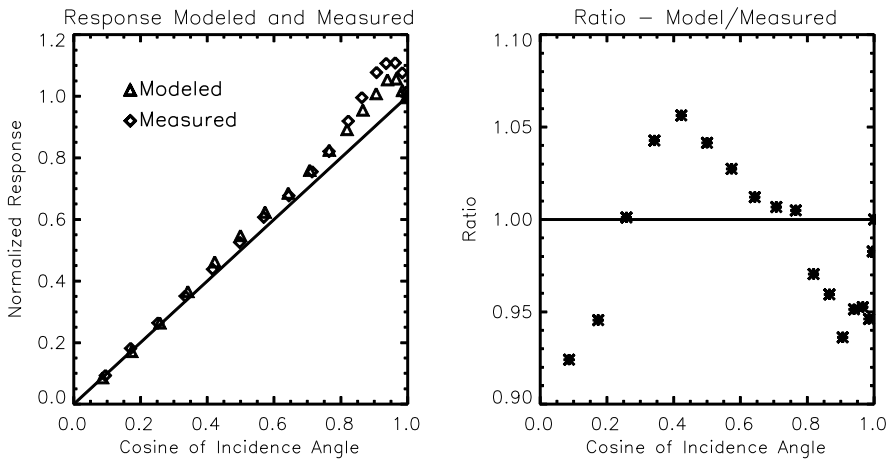

Figure 3.4: Plotted on the left panel are the measured and ZEMAX modeled cosine response of the integrating sphere based on the Crowther design and reduced in size for aircraft measurements. On the right is the ratio (model divided by measurement) of the integrating sphere responses.

its edges (as the baffle tapers in thickness near its edges, some light will be transmitted).

3.6 Empirical testing of various baffle designs

Prior to Monte Carlo modeling of baffle design, empirical testing of various baffle shapes was performed. These shapes included a sphere, hemisphere, cylinder, cones with varying aspect ratio, and cones with specular instead of diffuse surfaces. Ultimately, each of these designs was discarded because they did not improve the angular response. They are included to document the various effects on the cosine response with shape. A sampling of the various shapes tested is shown in Figure 3.6.

Two metrics of the error of the cosine response were devised and are shown in the upper left of each plot in Figure 3.6. The first metric (ϵ_{cos}) is the mean absolute percentage deviation across the eighteen incident angles (θ_x) measured, weighted by the cosine of each angle. The irradiance is $\mathbf{I}$ at each angle and the number of angles tested ($\mathbf{n}$) was fixed at eighteen. The cosine weighting of the error scales the error contribution of each angle to the overall signal. Percent differences are often highest at high incidence angles (e.g. $\theta = 85°$) because this is the ratio of two small numbers. However, the contribution to the overall signal for these angles is usually small except for cases when the dominant radiant source is close to the horizon. The second metric (ϵ) plotted is the mean absolute percent deviation without the cosine weighting. The formulae for computing the error metrics are given by equations (1) and (2).

$$\epsilon_{cos} = \frac{1}{n}\sum_{x=1}^{n}\left[\left[1 - \left|\frac{I(\theta_x)_{measured}}{I(\theta_x)_{ideal}}\right|\right] cos(\theta_x)\right] \tag{3.1}$$

$$\epsilon = \frac{1}{n}\sum_{x=1}^{n} 1 - \left|\frac{I(\theta_x)_{measured}}{I(\theta_x)_{ideal}}\right| \tag{3.2}$$

One of the first laboratory tests of the cone design was to simply change the aspect ratio of the cone by widening or narrowing the cone base with a fixed cone height. The

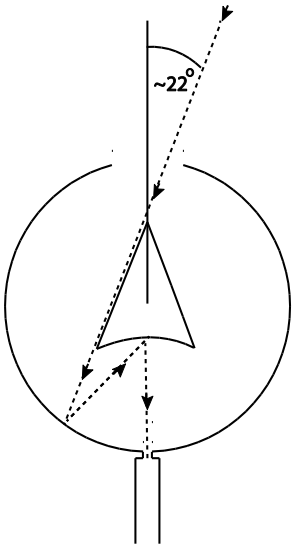

Figure 3.5: A simple schematic drawing illustrates the cause of the hotspot.

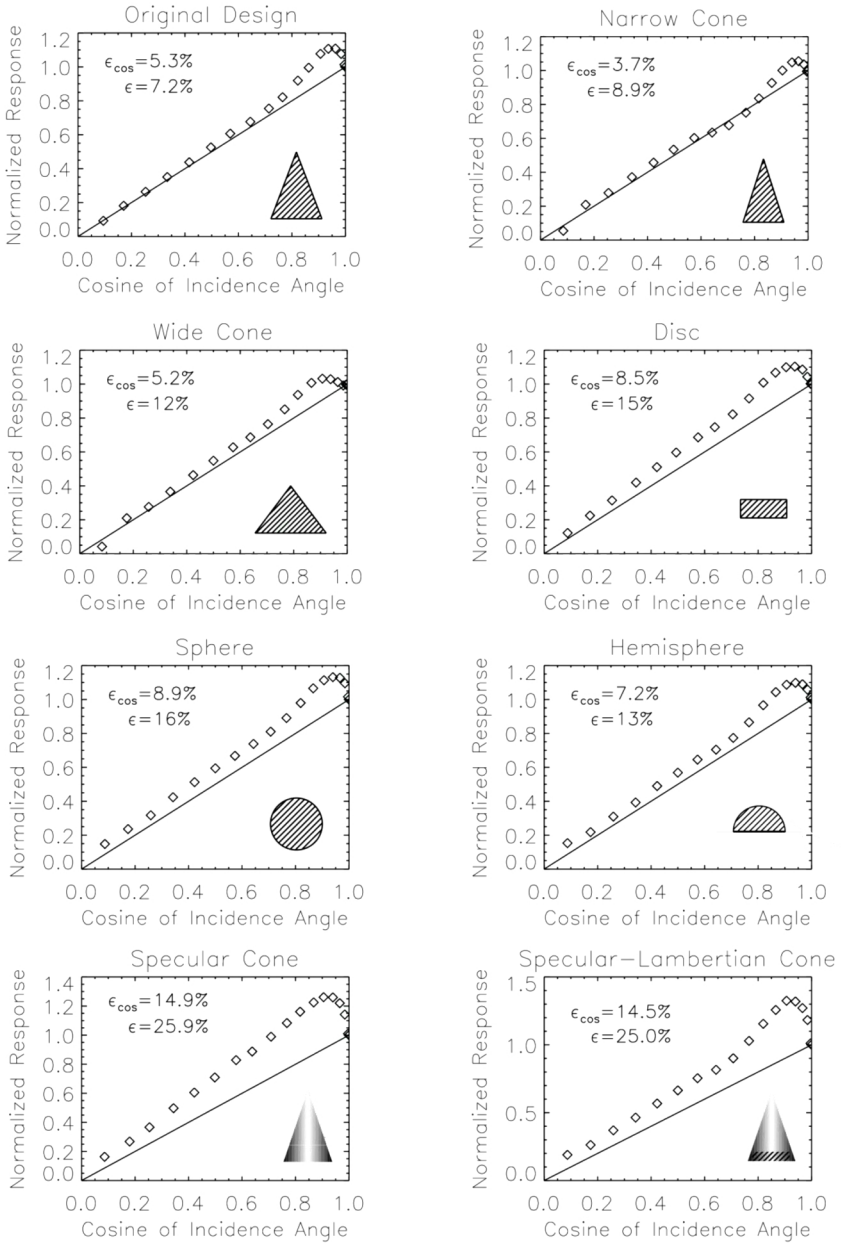

Figure 3.6: Several designs tested to examine the effect of the baffle shape on the cosine response. In the lower right hand corner of each plot is a simple cross sectional view of the baffle shape. The cross hatching is meant to indicate the baffle was constructed from PTFE (Fluorilon-99W^{TM}). Specular cones were made from polished aluminum.

change in aspect ratio supported the explanation of the hotspot proposed by *Crowther* [1997]. By widening or narrowing the base of the cone, the hotspot was moved closer to normal incidence (a narrower cone) or was pushed to angles farther away from normal incidence (a wider cone). This is evident in Figure 3.6 when comparing the results from the wide and narrow cones.

These various designs all produced cosine responses that were, in general, worse than the original design. Tests included a polished aluminum surface (i.e. a specular surface) and a specular-diffuse cone in which the base (viewed by the fiber optic) of the cone was a diffuse, Fluorilon-99W™ surface inserted into the polished aluminum cone base. The results of cones with specular surfaces were especially poor both in terms of angular response and sphere throughput.

3.7 An improved baffle design

Several variations in sphere baffle design were investigated with ZEMAX. Modeling was performed to determine the effect of various baffle shapes and their placement within the sphere.

One improvement in the modeled response was realized by narrowing the base of the cone to less than the diameter of the opening aperture. Unlike the original design, this allows some of the light at normal incidence to reach the bottom of the sphere directly, reflect off of the base of the cone and through the exit. Figure 3.7 illustrates the concept of leaving a gap between the entrance aperture and the base of the conical baffle. The base of the baffle still filled the field-of-view of the fiber optic preventing any photons entering directly from the entrance aperture.

The results of the ZEMAX model and laboratory testing of a cone with a base diameter of 8.7 mm and a cone full angle of 24° are shown in Figure 3.8. The area of the opening aperture is 71.2 mm^2 and the area of the base of the new cone is 59.4 mm^2 so that the base of the cone underfills the entrance aperture by 16.5%. The deviation

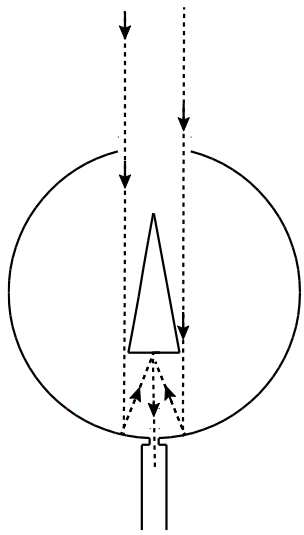

Figure 3.7: The narrow gap cone allows some light to pass the cone at normal incidence to the bottom of the sphere, scatter directly to the base of the cone, and into the fiber optic.

from ideal cosine was reduced to less than 5%, a better than three-fold improvement from the 17% deviation from ideal cosine of the original design. The errors were reduced from 5.3% to 2.0% for the cosine weighted error ϵ_{cos}, and from 7.2% to 5.1% for the unweighted error (ϵ). The response from the new design contained a second deviation from ideal cosine centered at 0.7 ($\approx 45°$) and in the opposite direction of the hotspot. Here the response is approximately 7-8% too low. Again the ZEMAX model reproduced the general angular response including this dip in response centered at 0.7, but the magnitudes of the deviations from true cosine were lower than the in the measurements. The hotspot was underestimated by ZEMAX as was the drop in signal around 0.7. This dip can be seen in the measurements of several designs including the hemisphere and the first narrow cone in Figure 3.6. Again the peak of the (reduced) hotspot corresponds roughly to the half angle (12° or 0.97 in cosine) of the cone; in agreement with the results and interpretation with cones of other widths. Recessing the fiber optic tip a few millimeters away from the exit aperture also reduced the magnitude of the hotspot.

3.8 Summary and conclusions

Achieving perfect cosine response for a light collector over a large range (>90%) of the solar spectrum is a challenging problem. Transmissive light collectors suffer from two drawbacks: 1) at high zenith angles the deviation from ideal cosine is large and 2) the materials used to construct them often have strong absorption features that degrade the signal at longer wavelengths. This has necessitated the use of miniaturized integrating spheres for aircraft measurements of solar spectral irradiance. Integrating spheres have the advantage that the cosine response is generally independent of wavelength and work well at high zenith angles. Near ideal cosine response has been achieved with integrating spheres, but with very low throughput (estimated at 0.01%). The fundamental challenge is to optimize high cosine-response fidelity without reducing the signal to unacceptably low levels.

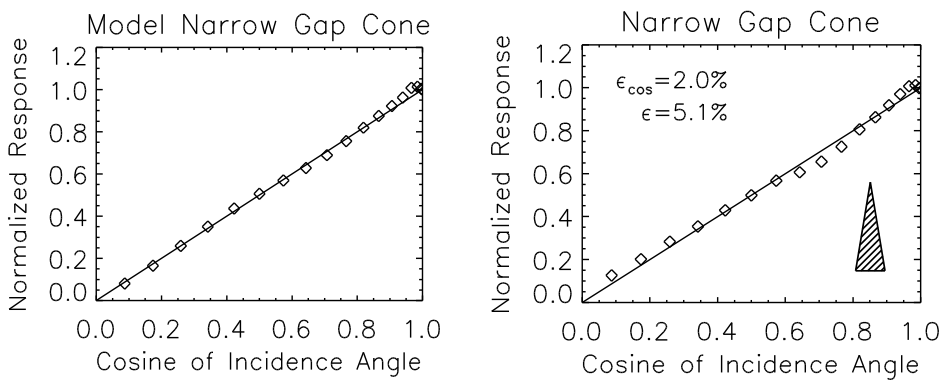

Figure 3.8: On the left panel the model predicted cosine response is plotted, on the right panel the laboratory measured response of the narrow gap cone is plotted.

The work here has focused on modifying the sphere design of [*Crowther*, 1997], specifically the baffle design. In the same way that *Crowther* [1996] design utilized a Monte Carlo ray tracing program to model the angular response of an integrating sphere this work has used the commercial software package ZEMAX to model the effects of the baffling on the angular response. Prior to the use of the ZEMAX model a variety of baffle shapes were tested but were not found to significantly improve the cosine response and in nearly all cases the response worsened. ZEMAX modeling indicated that by reducing the diameter of the baffle base to a diameter smaller than that of the opening aperture the hotspot would be substantially reduced in magnitude. A prototype cone was constructed and the results of ZEMAX were confirmed. The new cone reduced the hotspot from 17% above ideal cosine to less than 5% above ideal cosine. While mitigating one problem, the new design degraded performance at cosine 0.7 (45°) by 6-8%. At these angles, this is nearly the same percentage deviation from ideal cosine of the original design but in the opposite direction-the response is too low, not too high. The cosine response of the original and the new design are plotted together in Figure 3.9.

This work in improving the cosine response has focused solely on the design of the baffle. Although substantial improvement has been made, ideal cosine has yet to be realized. Other avenues of sphere modification, such as modifying the sphere walls will be investigated in the search for an ideal cosine light collector useful for airborne spectrometer measurements.

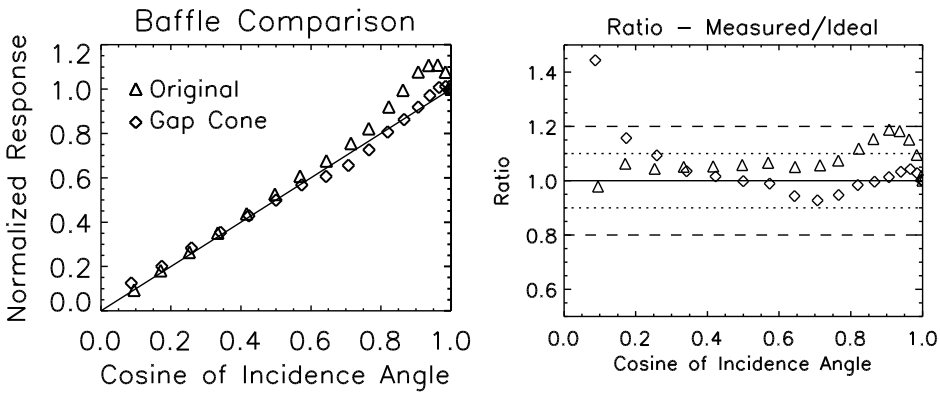

Figure 3.9: A direct comparison of the original design and the narrow gap cone design is plotted on the left panel. On the right panel the is ratio (model divided by measured) of the two designs.

Chapter 4

Observations and modeling of ice cloud shortwave spectral albedo during the Tropical Composition, Cloud and Climate Coupling Experiment

Ice cloud optical thickness and effective radius have been retrieved from hyperspectral irradiance and discrete spectral radiance measurements for four ice cloud cases during the Tropical Composition, Cloud and Climate Coupling Experiment (TC^4) over a range of solar zenith angle (23° to 53°) and high (46-90) and low (5-15) optical thicknesses. The retrieved optical thickness and effective radius using measurements at only two wavelengths from the Solar Spectral Flux Radiometer (SSFR) Irradiance and the MODIS Airborne Simulator (MAS) were input to a radiative transfer model using two libraries of ice crystal single scattering optical properties to reproduce spectral albedo over the spectral range from 400 to 2130 nm. The two commonly used ice single scattering models were evaluated by examining the residuals between observed spectral and predicted spectral albedo. The SSFR and MAS retrieved optical thickness and effective radius were found to be in close agreement for the low to moderately optically thick clouds with a mean difference of 3.42 in optical thickness (SSFR lower relative to MAS) and 3.79 μm in effective radius (MAS smaller relative to SSFR). The higher optical thickness case exhibited a larger difference in optical thickness (40.5) but nearly identical results for effective radius. The single scattering libraries were capable of reproducing the spectral albedo in most cases examined to better than 0.05 for all wavelengths.

Systematic differences between the model and measurements increased with increasing optical thickness and approached 0.10 between 400-600 nm and selected wavelengths between 1200-1300 nm. Differences between radiance- and irradiance-based retrievals of optical thickness and effective radius error sources in the modeling of ice single scattering properties are examined.

4.1 Introduction

Ice clouds play an important role in the radiative budget of the Earth's atmosphere see for example, *Chen et al.* [2000], *Ramanathan et al.* [1989]. The scattering and absorption of solar radiation reduces the amount of energy reaching the surface and thus has a cooling effect. Conversely, in the terrestrial thermal infrared wavelengths, ice clouds absorb radiation and emit at a lower temperature than the Earth's lower atmosphere and surface. This reduces the amount of energy radiated to space, increases the downward infrared radiation, and warms the surface. Whether ice cloud top of the atmosphere (TOA) net radiative effect is cooling or heating is dependent on several factors including cloud height, cloud thickness, and cloud microphysics [*Stephens et al.*, 1990, *Ebert and Curry*, 1992, *Jensen and Toon*, 1994, *Baran*, 2009], for example. Ice cloud microphysical, optical and ice bulk properties that determine the radiative properties of clouds are perhaps the least well understood of these.

Liquid water cloud radiative transfer calculations utilize Lorenz-Mie theory, an exact computational method for calculating the single scattering properties (e.g. single scattering albedo and phase function or its first moment, called the asymmetry parameter) of homogeneous spheres. In contrast to liquid water droplets, non-spherical ice cloud particles encompass a wide variety of shapes and sizes and thus computing their radiative properties must rely on more involved numerical techniques. To this end, extensive modeling and some measurements of ice crystal single scattering properties have been undertaken [*Takano and Liou*, 1989, *Macke et al.*, 1996, *Yang and Liou*, 1998, *Yang*

et al., 2003, 1997, *Mishchenko et al.*, 1996, *Baran and Labonnote*, 2007, *Havemann and Baran*, 2004, *Ulanowski et al.*, 2006] and continues to be an area of active research.

These models are used for satellite remote sensing retrievals of cloud optical properties (e.g. MODIS, AVHRR, etc) [*King et al.*, 1992, *Platnick et al.*, 2003]. Ultimately, these types of satellite retrievals are used: as inputs to climate models to properly parameterize ice cloud radiative effects [*Stephens et al.*, 1990, *Fu*, 2007, *Edwards et al.*, 2007], to potentially improve ice water parameterization in global circulation models [*Waliser et al.*, 2009], and to aid in the study of ice cloud processes [*Jiang et al.*, 2009].

One of the main purposes of this study was to examine how well the models of single scattering optical properties of ice particles can reproduce the spectral albedo of ice clouds encountered during TC^4. Satellite retrievals of cloud optical thickness and effective radius are typically retrieved at just two spectral bands, one in the visible to very near-infrared where ice and liquid water are non-absorbing and the other in the shortwave-infrared where ice and liquid water weakly absorb. The former is most sensitive to cloud optical thickness, the latter to cloud particle size. For a complete description of this type of retrieval see, for example, *Twomey and Cocks* [1989] or *Nakajima and King* [1990].

Current models of ice single scattering properties contain far more than two wavelengths. The models used in this study contains 140-150 wavelengths [*Yang and Liou*, 1998, *Baum et al.*, 2005] spread across the solar spectrum. In principle, if the model of the single scattering is spectrally accurate, then the retrieved optical thickness and effective radius from as few as two wavelengths should accurately predict the spectral albedo for the entire spectrum for plane-parallel, homogenous, single layer clouds. By retrieving the optical properties of ice clouds, using the classical two wavelength technique, one should be able to test, at the very least, how consistent the wavelength to wavelength albedo is modeled by comparing with spectral measurements of albedo from the Solar Spectral Flux Radiometer (SSFR).

A previous study was conducted comparing the retrieval of optical properties from solar wavelengths with thermal wavelengths [*Baran and Francis*, 2004]. It was shown that when the incorrect ice single scattering model was used the results were physically inconsistent; for the same cloud scene the incorrect ice model did not simultaneously retrieve the same values of optical thickness and effective radius across both the solar and thermal spectrum. This study argued for high resolution measurements across the spectrum (solar and thermal wavelengths) to discriminate between ice models. Here we have examined the spectral consistency at high spectral resolution and sampling over the majority of the solar spectrum, at optical thicknesses ranging from 3 to 46 and solar zenith angles ranging from 23° to 53°. Unlike the *Baran and Francis* [2004] study, we haven't examined the thermal portion of the spectrum but instead have focused solely on the solar portion of the spectrum, extending the wavelength range further into the near-infrared, covering several zenith angles, comparing hundreds of spectra, and using hyperspectral irradiance in addition to multispectral radiance measurements for comparison. Because many remote sensing retrievals of cloud optical thickness and effective radius rely on these single particle scattering models testing their spectral fidelity is an important validation. The accuracy of the models cannot be judged solely from remote sensing measurements as it implies some level of circularity because the scattering models themselves are necessary for the retrieval of optical thickness and effective radius. It would be preferable, for instance, to have an independent measurement of particle size that does not rely on ice scattering models. Particle size measurements, in situ, were made during TC^4, but are prone to crystal shattering [*McFarquhar et al.*, 2007, *Jensen and Toon*, 1994]. Even in the absence of in situ measurement errors like inlet shattering, issues of cloud volume sampling -small and usually deep within a cloud for in situ measurements-large and near cloud top for radiation measurements also confound efforts at comparing the two. For these reasons, no in situ data were used.

A second focus of this study was a comparison of irradiance and radiance based

retrievals of cloud optical properties. Satellite remote sensing retrievals are, by necessity, radiance based and implement observations from discrete wavelength bands distributed across the solar and terrestrial spectrum. A selection of channels from radiance-based remote sensing instruments is, by itself, insufficient to completely determine the effects of clouds on the Earth's radiation budget. In practice, irradiance cannot be measured directly from space-borne platforms in low Earth orbit. It is, however, measured from aircraft. To bridge the fundamental geometrical and spectral differences between satellite measurements of discrete-band radiance and the more energetically relevant quantity, continuous spectral irradiance, field campaigns deploying instruments that measure discrete-band radiance and hyperspectral irradiance have been conducted: the Ice Regional Study of Tropical Anvils and Cirrus Layers-Florida Area Cirrus Experiment (CRYSTAL-FACE) [*Jensen et al.*, 2004]; and the focus of the present study, the Tropical Composition, Cloud and Climate Coupling experiment (TC^4) [*Toon et al.*, 2010]. In TC^4 the high altitude NASA ER-2 flew with the SSFR, which measured spectrally continuous solar irradiance (400-2200 nm), and the MODIS Airborne Simulator (MAS), a discrete-band imaging spectrometer that measured solar reflected and thermal emitted radiance (550-14200 nm).

This paper is organized as follows: (1) the measurements of spectral irradiance from the SSFR and radiance imagery from MAS, (2) models of single scattering optical properties and their incorporation into a radiative transfer model along with the method employed for retrieving the optical thickness, effective radius, and albedo, (3) cloud optical thickness and effective radius retrieved from MAS radiance and SSFR irradiance using two currently available ice single scattering libraries, (4) the spectral albedo calculated from a two-wavelength SSFR retrieval compared with the measured spectral albedo and also the spectral albedo calculated from a two-wavelength MAS radiance retrieval compared with the measured spectral albedo, (5) individual spectra for high and low optical thickness and effective radius from each case, and (6) a summary of the

work.

4.2 Measurements of radiance and irradiance during TC^4

The NASA ER-2 was instrumented with the SSFR and either the MODIS Airborne Simulator (MAS) [*King et al.*, 2004] or the MODIS/ASTER (MASTER) airborne simulator [*Hook et al.*, 2001] for thirteen flights together over the course of the experiment. These flights covered a wide variety of cloud types, including extensive fields of low marine stratus, tropical convective systems, and high tropical ice clouds-the focus of this paper. Because only data from the MAS instrument was ultimately used in this work, only the MAS instrument will be described in detail.

4.2.1 Solar Spectral Flux Radiometer (SSFR)

The SSFR consists of two spectrometers connected via a fiber optic to a miniature integrating sphere mounted on the top (zenith viewing) and bottom (nadir viewing) of the NASA ER-2. The integrating spheres provide the cosine response over the wide wavelength range of the SSFR that is required to make a measurement of spectral irradiance. The wavelength range of the instrument, 350 to 2150 nm, encompasses 90% of incident solar radiation. The spectral resolution as measured by the full-width-half-maximum (FWHM) of a line source is 8 nm from 400 to 1000 nm with 3 nm sampling and 12 FWHM from 1000 to 2200 nm with 4.5 nm sampling The SSFR records a nadir and zenith spectrum every second.

The spectrometers are calibrated in the laboratory with a NIST-traceable blackbody (tungsten-halogen 1000 W bulb). The radiometric stability of the SSFR is carefully tracked during the course of a field experiment with a portable field calibration unit with a highly stable power source and 200 W lamps. The calibration has generally held to the 1 to 2% level over the course of a several week field mission as it did during TC^4. The radiometric calibration was adjusted for minor fluctuations measured by the field

calibration from flight to flight. In addition, the data were filtered using the aircraft navigation and ephemeris data to eliminate time periods when the aircraft attitude was not level (e.g. turns, takeoff and landing, turbulence). The estimated uncertainties in the absolute calibration of the instrument are 5%. We note that when retrieving cloud optical properties with albedos, as was done here, error in the absolute calibration cancel. Errors from unknown offsets in aircraft navigation data or reflections from clouds may remain however. For a more complete description of the SSFR instrument see *Pilewskie et al.* [2003].

4.2.2 MODIS Airborne Simulator (MAS)

The MAS instrument is an imaging spectrometer with 50 discrete bands distributed throughout the solar reflected and thermal emitted parts of the spectrum. Twenty-two of the bands in the solar region overlap with the SSFR from 461 to 2213 nm. The spectral bandpass of MAS in the visible and near-infrared channels are in the range of 40-50 nm, it has a 2.5 mrad instantaneous field of view (IFOV), and 16-bit analog to digital conversion. MAS is typically preflight and postflight calibrated in the laboratory with an integrating sphere and uses an integrating hemisphere in the field for stability monitoring. For details on MAS calibration issues and investigations during TC^4, see *King et al.* [2010]. Because it is an imager, it provides excellent spatial context ($\approx$25 m nadir pixel resolution with $\approx$17 km swath width for typical TC^4 ice cloud heights) with which to help interpret the measurements of irradiance from SSFR.

All thirteen flights and all flight legs therein were examined with the MAS or MASTER cloud products which includes cloud optical thickness, cloud phase, cloud top height, and temperature information. The flight legs used in this study were selected based on several criteria: the abundance of ice clouds; legs that were only over open ocean to simplify the input of surface spectral albedo into the radiative transfer calculations; the apparent absence of low level clouds which might make the retrieval of ice cloud

properties more complicated and prone to error (an example of this which occurred frequently in the data are low level cumulus clouds, presumably liquid water, beneath an optically thin layer of ice cloud); and finally, stable, level flight which is required for the measurement of irradiance. Four flight tracks from 17 July 2007 (the ER-2 was equipped with MAS instrument that day) met these criteria and were used for analysis in this work. The cosine of the mean solar zenith angle (denoted by μ) for the four flight legs were 0.60, 0.82, 0.88, and 0.92. For the remainder of this paper the four cases will be distinguished by their cosine of solar zenith angle. (i.e. the μ=0.82 case, the μ=0.88 case, etc). Of these cases three (μ=0.60, 0.82, 0.88) had low to moderate optical thickness (3-15) and one case (μ=0.92) had high optical thickness (40-50)

4.2.3 Radiative transfer calculations of irradiance

Analysis of solar spectral irradiance from SSFR has led to the development of a radiative transfer code optimized for the spectral characteristics of the SSFR and for flexibility in specifying cloud and aerosol radiative properties [*Bergstrom et al.*, 2003, *Coddington et al.*, 2008]. The molecular absorption by species such as water vapor, oxygen, ozone, and carbon dioxide, are calculated using the correlated-k method [*Lacis and Oinas*, 1991]. The band model was developed specifically for the SSFR by defining the spectral width of the bands by the slit function of the SSFR spectrometers, the half-widths of which were noted previously. The k-distribution is based on the HITRAN 2004 high resolution spectroscopic database [*Rothman*, 2005]. The model uses the discrete ordinate radiative transfer method (DISORT) [*Stamnes et al.*, 1988] to solve for the spectral irradiance and nadir and zenith radiance at each level. Molecular scattering optical thickness is calculated using the analytical method of *Bodhaine et al.* [1999]. The model contains 36 levels. In this study albedo was calculated at 20 km, the nominal flight level of the ER-2. The albedo is defined as the ratio of upwelling to downwelling irradiance at the flight level. A standard tropical atmospheric profile of water vapor and

well mixed radiatively active gases was used. No attempt was made to fit the water vapor amount to match the measurements; this would be computationally prohibitive and unnecessary, because the absorption bands of water vapor, oxygen, etc. are avoided for inferring cloud optical properties. The wavelengths used for the cloud retrieval of optical thickness and effective radius are 870 and 1600 nm. These wavelength channels are free of strong gaseous absorption.

No aerosol was included in the model because these are tropical, high level clouds, and are unlikely to contain much aerosol. The top of the atmosphere (TOA) solar spectrum is given by the Kurucz spectrum *Kurucz* [1992]. The input surface albedo (always ocean) was specified by constant value of 0.03 [*Jin et al.*, 2004].

The input to the radiative transfer model first requires that the phase function of the ice particles be represented in terms of a Legendre polynomial series where the number of terms is set to the number of streams used in the DISORT calculation. All of the DISORT calculations for this study were done with 16 streams with Delta-M scaling [*Wiscombe*, 1977] to account for the strong forward scattering peak in the phase function typical of large size parameters. For the accurate calculation of irradiance at least six streams are required; streams are the number of quadrature points in the angular integration of scattering. We used the technique of *Hu et al.* [2000] to fit the phase function with the Legendre coefficients for input into the radiative transfer

Clouds heights for these cases were examined using the MAS cloud height product and were found to vary from between 8 to 12 km. A cloud height sensitivity test was performed by setting a cloud deck to 12 and to 8 km, for the retrieval of cloud optical properties. Little to no change in the retrieved values was found, so that the calculation was set to 10 km for all of the cases. This is the result of using 870 nm as one of the retrieval wavelengths. The molecular scattering is reduced at this wavelength and the effect on the retrieval of cloud height was small. The use of a shorter wavelength (e.g. 500 nm) would likely show a greater sensitivity to cloud height.

The effects of cloud vertical [*Platnick*, 2000] and horizontal [*Platnick*, 2001] inhomogeneity on the retrieval of cloud optical properties have been investigated previously. For clouds with varying vertical and or horizontal microphysical structure, the use of different wavelengths in the inversion procedure may result in different values of retrieved effective radius. However, these differences are typically small compared to retrieval errors [*Platnick*, 2000, *Ehrlich et al.*, 2009]. In this paper, all calculations were done assuming plane-parallel, homogenous (vertically and horizontally) clouds. The impact of vertical or horizontal cloud in homogeneities on retrievals of optical thickness and effective radius was not investigated in this work.

4.2.4 Ice particle single scattering models

The ice crystal single scattering models used here are the same ones used for the MODIS Collection 4 [*Baum et al.*, 2000, *Platnick et al.*, 2003, *Yang and Liou*, 1998], henceforth C4, and Collection 5 cloud products [*Baum et al.*, 2005], henceforth C5. The C4 models consist of plates, hollow and solid columns, 2-D bullet rosettes, and aggregates consisting of solid columns. The C4 ice crystal scattering model provide scattering properties for 5 size bins and were integrated over 12 particle size distributions. The range of effective radii in C4 is 6.7 to 59 μm with a total of twelve effective radii. The small particles in C4 are assumed to be compact hexagonal ice particles. The results from C4 (Figures 4.6 and 4.7 and plotted in blue), used in the MODIS collection 4 [*Platnick et al.*, 2003] are shown primarily because it has continuous spectral coverage from 400 to 1695 nm and fills in some of the spectral regions not covered in C5. The resultant albedo spectra produced using C4 and C5 ice particle scattering models produced very similar spectra (figures 4.6 and 4.7) as will be shown.

The more recently developed C5 models consist of mixtures of different ice particle shapes (e.g. droxtals, solid and hollow columns, plates, 3-D bullet rosettes, and aggregates of columns). The scattering properties for each of these particles are avail-

able for 45 individual size bins. For both sets of bulk models, all particles are smooth except for the aggregate, which is roughened. The roughening parameter is 0.3 [B. A. Baum, personal communication, 2009]. For C5 the ice particles range in size from 5 to 90 microns in a step size of ten microns for a total of eighteen different effective radii. The wavelength coverage is from 400 to 2200 nm, matching the SSFR coverage. The database contains some spectral gaps, in the regions 1000-1200 nm, 1700-1800 nm, and 1950-2050 nm. Outside of the gaps the spectral sampling is 10 nm. Each size regime in the model consists of a different mixture; the smallest consists of only droxtals for C5, the largest is predominantly bullet rosettes. Intermediate sizes are varying mixtures of shapes. The relative contribution of each particle shape to the size distribution is different between C5 and C4; *Yang et al.* [2007] gives a detailed summary of each.

The single scattering properties include a scattering phase function defined at 498 angles between 0 and 180 degrees, asymmetry parameter, extinction efficiency, extinction and scattering cross sections, single scattering albedo (ϖ_0), and a delta transmission factor (δ). The delta transmission factor is wavelength dependent and is used to scale the input optical thickness (τ) and single scattering albedo in the radiative transfer model according to equations 4.1 and 4.2.

$$\tau' = (1 - \delta\varpi_0)\tau \tag{4.1}$$

$$\varpi_0{}' = \frac{(1-\delta)\varpi_0}{1-\delta\varpi_0} \tag{4.2}$$

The primed quantities are the delta-scaled values of optical thickness and single scattering albedo. The delta-transmission factor is used to account for transmission through plane parallel ice particle planes in the forward direction i.e. at a scattering angle of zero degrees [*Joseph et al.*, 1976, *Takano and Liou*, 1989]. The effective radius is defined by equation 4.3. where <V> is the mean particle geometric volume and <A>

is the orientation-averaged projected area for the ice crystal size distribution [*Mitchell*, 2002].

$$r_{eff} = \frac{3}{4}\frac{< V >}{< A >} \tag{4.3}$$

The panel on the left hand side of Figure 4.1. shows an example of the library phase function at 870 nm for the largest (solid line) and smallest (dash-dot line) effective radii in C5. On the right hand panel of Figure 4.1 the single scattering albedo wavelength spectra of a smallest and largest size effective radii (C5) are shown. The phase function for the largest size exhibits ice halo features at 22 and 46 degrees; the phase function for the smallest particle size is notably smoother. The differences in phase functions are a result of both particle size, shape, and the differences in particle mixtures which are different for each effective radius. In the shortwave-infrared the single scattering albedo for the largest size is reduced below that of the smallest size, as expected from simple geometric optics [*Bohren and Huffman*, 1983]. This forms the basis for the retrieval of effective radius in this spectral regime. Ice is essentially non-absorbing in the visible.

To generate an albedo library for each case, a series of cloud optical thicknesses, thirty in total, were calculated for each of the four solar zenith angles. Optical thickness step sizes range from 0.5 at the smallest optical thickness, to 2 to 5, at intermediate optical thickness, and 10 at the highest optical thickness (50-100). All optical thickness values given in this paper are for 870 nm. The resolution in the calculation of the various effective radii was given by the single scattering ice library employed; eighteen in the case of the C5, twelve for the C4 library. The C4 library is not evenly spaced in effective radius; it contains finer sampling in the range of 25 to 40 μm. At this resolution, the spectra are sufficiently smooth so they can be interpolated with a high degree of accuracy to generate a finer optical thickness and effective radius grid. The optical thickness grid was linearly interpolated to increments of 0.1 from endpoints of the calculations, 0-100. The effective radii were linearly interpolated to a step size of 0.2 from the range of 5

to 90 μm in the C5 library and 6.7 to 59 μm in the C4 library. Figure 4.2 shows a range of optical thickness and effective radius of the calculated albedo spectra. The optical thicknesses are color coded and the effective radii are line style coded. Note that the spectra group by color in wavelengths between 400 and 1000 nm and contain information about optical thickness; the spectra cluster by line style for the wavelengths 1500 to 2150 nm, and contain information about effective radius.

4.3 Retrieval of optical thickness and effective radius from SSFR and MAS

For the retrieval of optical thickness and effective radius at least two wavelengths are chosen to determine a best fit to the calculated spectra. Previous work with retrievals from the SSFR has included up to five wavelengths [*Coddington et al.*, 2008]. Others have investigated the utility of including more than two wavelengths [*Cooper et al.*, 2006, *Baran et al.*, 2003]. The authors of these studies have advocated the use of more than two wavelengths in the retrieval of cloud optical properties for a more robust result. Because wavelength selection was not the focus of this study and comparison of SSFR and MAS retrievals was desired, we have chosen to follow the technique used in satellite retrievals and use the MAS wavelengths: 870 nm (water non-absorbing) and 1600 or 2130 nm (water absorbing). Measurement to measurement variation was smaller at 1600 nm for SSFR, so it was chosen for the water-absorbing wavelength applied in this analysis. A two step process was implemented as follows. The first step is an initial estimate from the uninterpolated data to determine the range that the measurement falls in; that range is used to constrain the retrieval in the interpolated data. This greatly increases the speed at which a minimum in the least squares fit is found, over the search of the entire high resolution library for each measurement. The "best-fit" is determined by minimizing the residual in a least squares sense (equation 4.4), of the measurement to calculated albedo

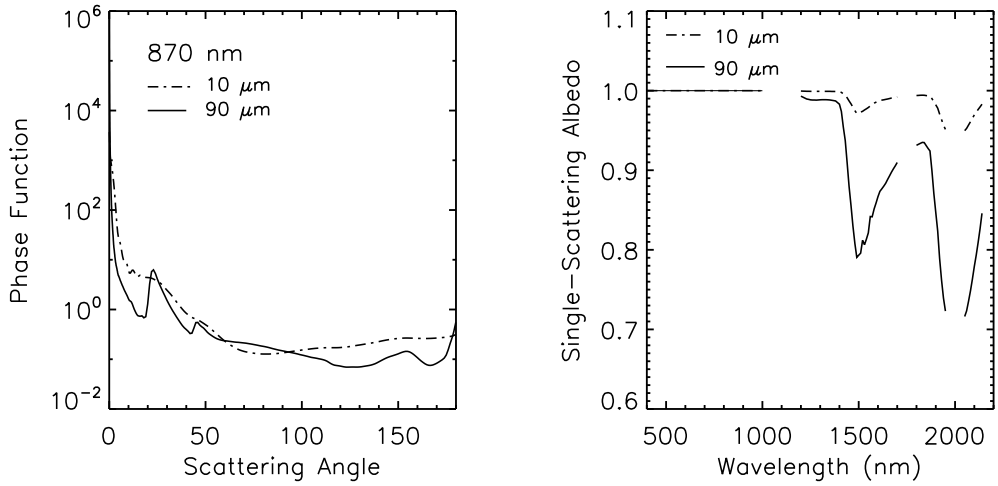

Figure 4.1: Phase functions of 870 nm from the C5 library for the largest (90μm, solid line) and smallest (10μm, dash-dot line)(right). Single-scattering albedo spectra for the largest (solid line) and the smallest (dash-dot) effective radii from the C5 library.

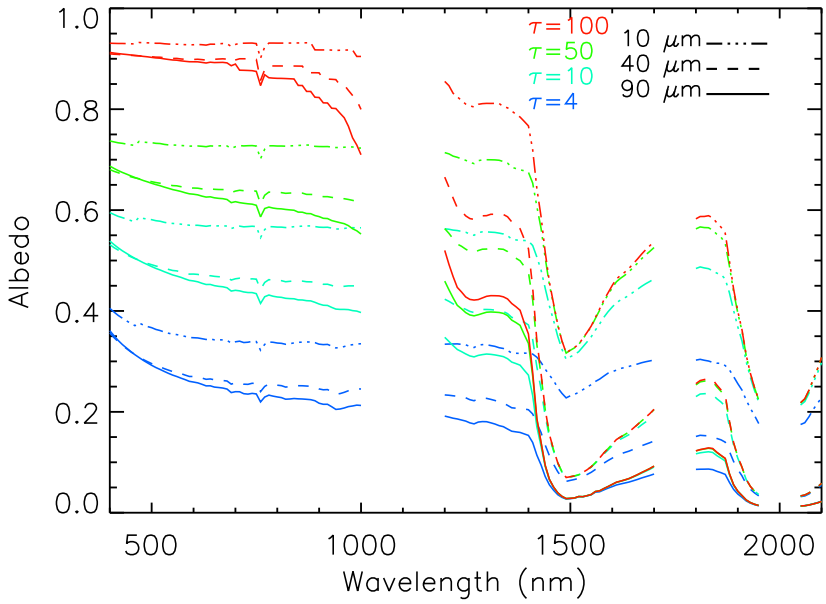

Figure 4.2: The results of the C5 library in the radiative transfer calculations of albedo spectra for three different effective radii and four different optical thicknesses. The spectra cluster by color (optical thickness) in the 400-1000 nm wavelength range, and by line style (effective radius) in the 1500-2150 nm wavelength range.

value at the given wavelengths.

$$residual = (vis_{measured} - vis_{modeled})^2 + (nir_{measured} - nir_{modeled})^2 \tag{4.4}$$

The calculation of optical thickness and effective radius for MAS is given by the MAS algorithm [*King et al.*, 2004] and is identical to that used for MODIS derived cloud optical properties. The MAS derived optical thickness and effective radius are the results of the NASA retrieval scheme and use the MODIS Collection 5 (C5) ice properties. No separate attempt was made to retrieve cloud optical properties with the MAS radiance data.

4.4 Analysis of spectral albedo properties

To test the ability of single scattering models to accurately reproduce the observed spectral albedo, we retrieved the optical thickness and effective radius using SSFR albedo at two wavelengths from each spectrum coincident with the MAS flight legs. The retrieved optical thickness and effective radius were then used to calculate the entire spectrum with the radiative transfer model. The left-most plot in Figure 4.3a is the MAS 650 nm radiance for the μ=0.82 case; time (UTC) is along the y-axis, the cross-track swath of MAS along the x-axis. The second from the left, (4.3b) is the spectral albedo measured by the SSFR. Wavelengths varies along the x-axis, time is on the y-axis. Note the strong water vapor absorption in the measurements at 1400 nm and 1900 nm, and weaker bands at 940 and 1140 nm, all represented by vertical bands in the image. The approximate band centers (940, 1140, 1400 and 1900 nm) of water vapor are over plotted with black dashed lines. Figure 4.4 shows a typical SSFR albedo spectrum with the water vapor band centers and band widths shown to aid in interpreting the spectra. The third panel (Figure 4.3c) image is the spectral albedo reconstructed from the 2-wavelength SSFR retrieval of the cloud optical thickness and effective radius. The white bands are the aforementioned spectral gaps in the ice-crystal model data (C5).

There is little evidence of water vapor absorption in this image. A comparison of the second and third panel images provides evidence that an insufficient amount of water vapor was used in the model but it is of no consequence in the present analysis because those bands were avoided in the retrievals. The image in the bottom panel shows the difference between the reconstructed albedo and the SSFR measured albedo. In this flight segment the optical thickness varied from 5 to 15 (see Figure 4.9 for the time series) and the effective radius varied from 25 to 35 μm. The difference image varies little over this change in optical thickness and effective radius, indicating that the single scattering optical properties given in C5 capture the range of possible single scattering properties needed to accurately reproduce the spectral albedos that were encountered during the flights examined here. Indeed, the difference plots for the μ=0.88 and μ=0.60 cases (not shown) are virtually identical to the μ=0.82 case shown here. The μ=0.92 case is somewhat different as will be discussed later in the paper when examining individual spectra.

In general, the differences outside of strong molecular gaseous absorption bands fall within 0.05 of the measured albedo. Larger differences occur in water vapor bands. These bands are highly variable and no effort was made to vary the standard tropical water vapor profile. All four cases examined here fall within moderate to high optical thicknesses. For the cloud optical thicknesses examined here, all substantially greater than unity, the spectral albedo is only weakly sensitive to particle shape [*Wendisch et al.*, 2005]. The effects of absorption are amplified through multiple scattering while angularly dependent scattering features are diminished. In Figure 4.5 the differences for all times are plotted at each wavelength showing the entire range of differences for all wavelengths (the small black dots that in aggregate form a line). Superimposed (red diamonds) is the calculated mean albedo difference at each wavelength. The albedo differences are typically less than 0.05, with some exception. Many of largest deviations occur on the edges of strong molecular absorbers such as the 1400 and 1900 nm water vapor wings or

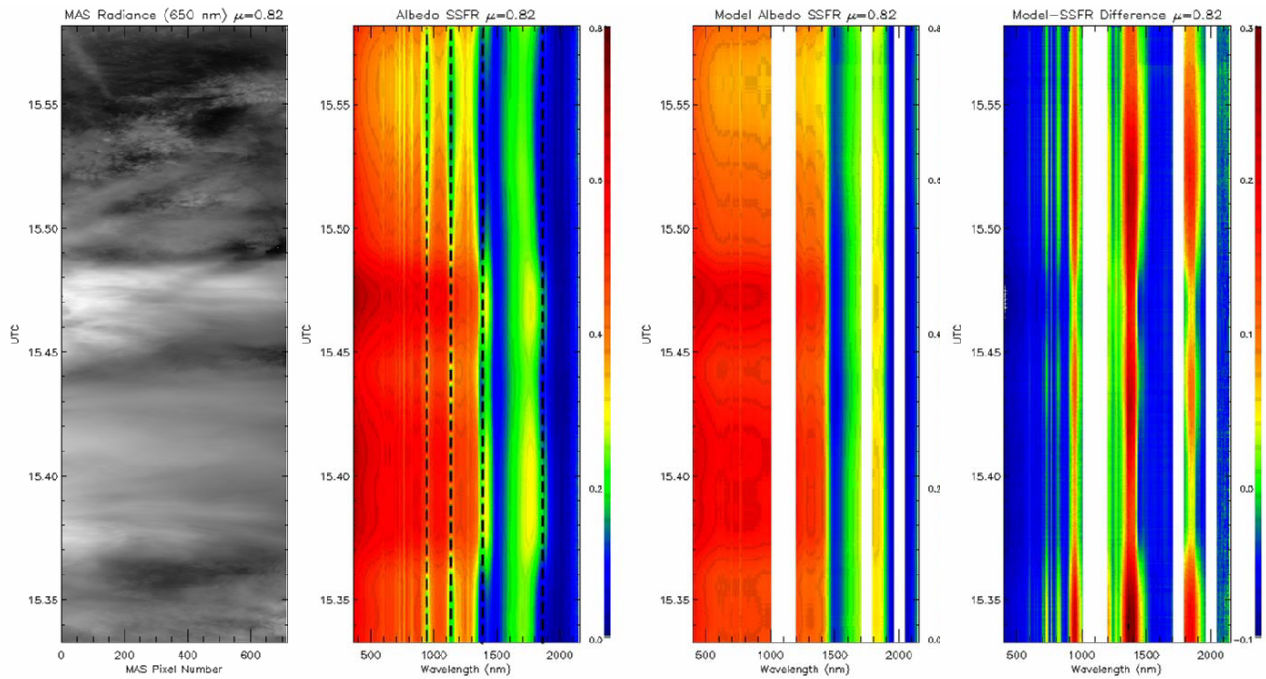

a. b. c. d.

Figure 4.3: Two-dimensional representations of the μ=0.82 case (a) MAS radiance at 650 nm. (b)SSFR-measured albedo with wavelength on the x-axis. (c)Calculated albedo using optical thickness and effective radius retrieved from SSFR. (d)Difference image between Figures 4.3b and 4.3c.

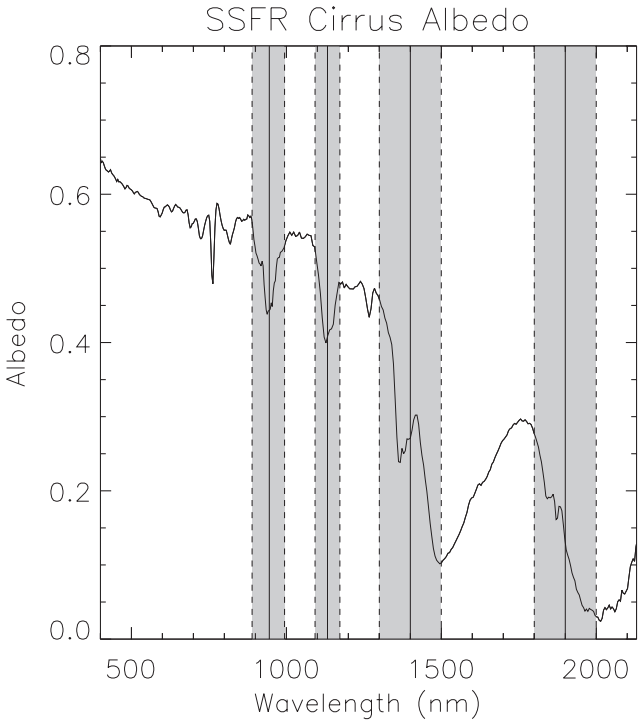

Figure 4.4: A typical SSFR cloud albedo spectrum is plotted with the major water vapor band centers (940, 1140, 1400, and 1900 nm) overplotted with vertical lines. The approximate band widths are the shaded regions bounded by the dashed lines.

the strong oxygen band at 763 nm and are the result of gaseous absorption.

The μ=0.88 case is the most spatially uniform, albeit short in duration, of the flight legs examined here; it has the smallest retrieved range and standard deviation in optical thickness. In terms of determining systematic differences between model and measurement, this is perhaps the best of the flight legs because spatial homogeneity is greatest. Wavelength to wavelength consistency (spectral shape) is similar for all the cases, although the variation within a particular wavelength may be greater (μ=0.92) or lesser (μ=0.82). The differences at the shortest wavelengths could be explained by differences in molecular scattering and/or the presence of aerosols. However, further examination of the lidar data showed no evidence of aerosols above the clouds for these cases and the molecular scattering component appears to be well modeled in the three moderate optical thickness cases. Because these errors are typically less than 0.03, and close to measurement error, no further refinement of the modeling was undertaken.

The exception to this is the μ=0.92 case that had optical thicknesses substantially higher (33-46) than the other cases (3-15). At the shortest wavelengths the differences are 0.07-0.08. The spectral shape of the differences is similar to the others cases, but the magnitude is greater. This is true only of the shorter wavelengths; for the wavelengths longer than 1500 nm the agreement is within 0.02-0.03. The reason for this difference is unresolved. The largest systematic difference between measurement and model in all cases, outside of strong gas absorption, occurs in the 1200 to 1300 nm range. Although this region does contain a relatively narrow collision band of oxygen at 1270 nm the mismatch is much broader. This mismatch increases with increasing optical thickness, and is most evident for the μ=0.92 case that has substantially higher optical thickness than the other cases. This may indicate that the single-scattering albedo is too high in this spectral region as multiple scattering (high optical thickness) amplifies absorption. The ice single-scattering properties in C4 and C5 used the *Warren* [1984] compilation for the ice optical constants. A new compilation by *Warren and Brandt* [2008] contains

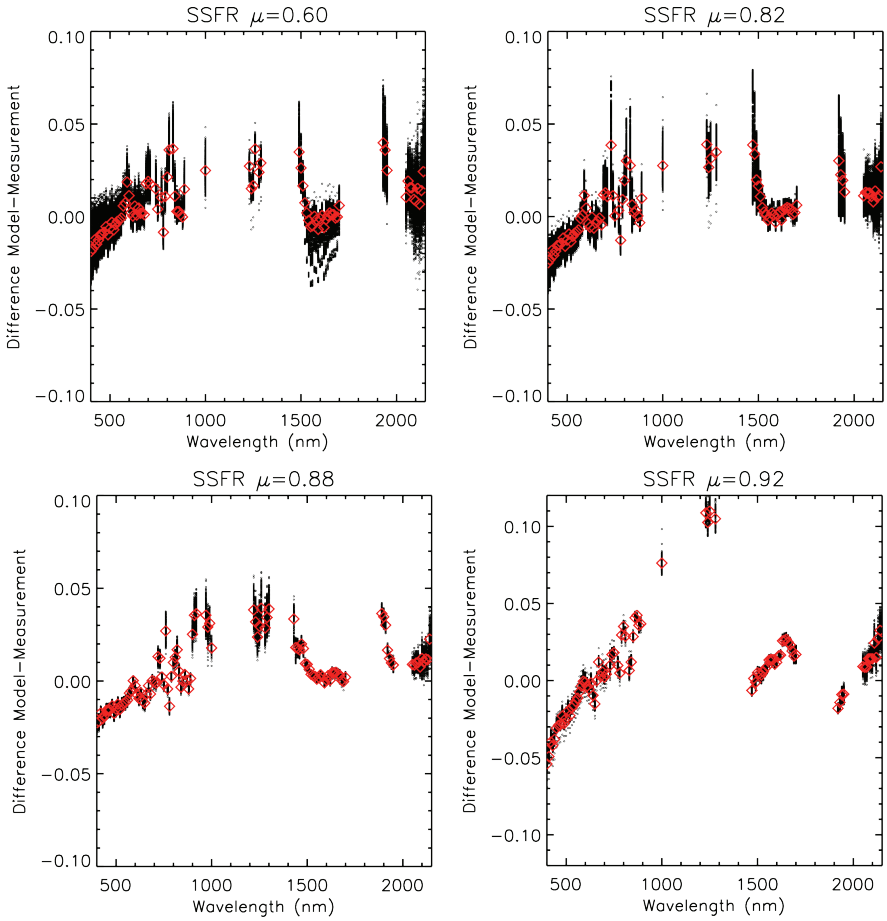

Figure 4.5: For each of the four cases the differences between modeled (C5) and measured albedo using optical thickness and effective radius derived from SSFR are shown. The black dots which aggregate to form lines are the differences for every line in the MAS flight track, and the red diamonds are the mean differences.

substantial changes in the near-infrared complex part of the index of refraction. In particular, the spectral range in the 1500 to 2000 nm spectral range has changed. The imaginary part of the complex index of refraction has increased at 1600 nm (one of the retrieval wavelengths) and decreased from 1700 to 1900 nm. The reanalysis of the measurements used in *Warren* [1984], better accounting for surface reflections, resulted in the changes made in *Warren and Brandt* [2008]. These changes have been implemented in the most recent single-scattering ice calculations by the developers of C4 and C5, but were not available for this analysis. Simple calculations indicate that these changes alone are probably not sufficient to account for the differences in the measurement and model, thus the explanation for this discrepancy remains unresolved. In addition, the spectral region from 1000 to 1300 nm has not changed in the new compilation.

A more detailed representation of the differences between the highest and lowest retrieved values of optical thickness and effective radius (four in total) for each of the four segments and its corresponding spectral albedo from SSFR is plotted in Figures 4.6 and 4.7. SSFR albedo spectra are plotted in black and are continuous; the red spectra were the reconstructed using C5, and the blue spectra C4. The regions of best agreement are from 1500 to 2100 nm, excluding the strong water vapor band at 1900 nm. For the case μ=0.92, the high optical thickness and height of the cloud reduce the water vapor absorption to the point where it ceases to interfere with the measurement of cloud albedo. This is because the column water vapor above these high altitude clouds is low and the contribution of water vapor absorption from below the cloud layer (due to its high optical thickness) is small. In the lower optical thickness cases, we are seeing "through" the cloud layer and the contribution of water vapor absorption from below the cloud layer is much greater. The agreement is quite similar (0.02) to the surrounding spectrum where water vapor does not interfere with the ice cloud albedo. Note that in all the cases, as the optical thickness becomes larger, the mismatch between the modeled and measured spectra becomes larger in the 1200-1300 nm spectral region.

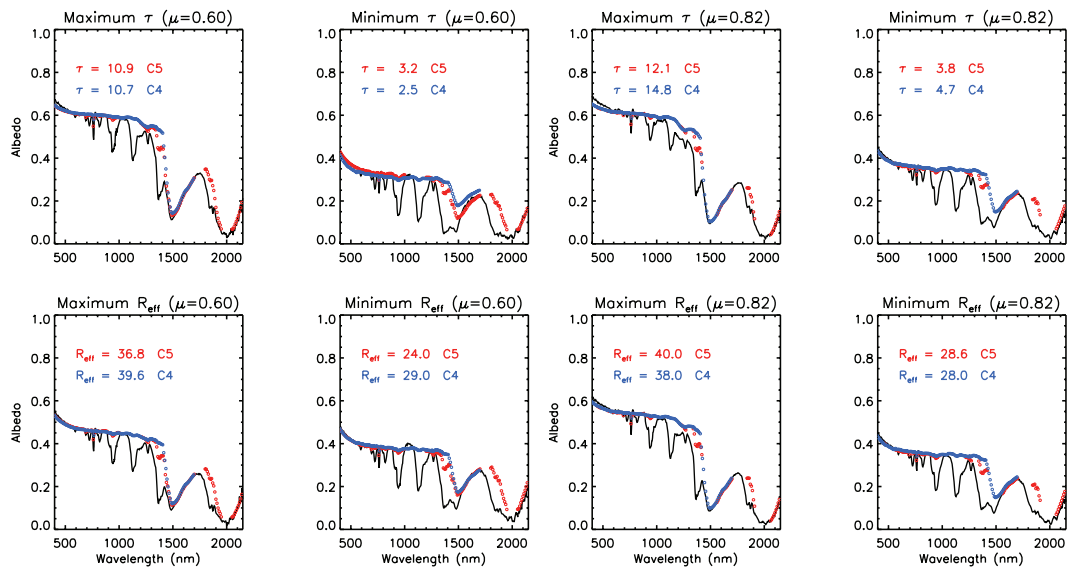

Figure 4.6: For cases μ=0.60 and μ=0.82 the highest and lowest optical thickness and effective radius albedo spectra are plotted with the full wavelength spectra as predicted from the single-scattering properties from C5 (red) and C4 (blue). Note the excellent agreement in all cases in the longer wavelengths. As the optical thickness increases, the agreement becomes worse in the shorter wavelengths and in the 1200-1300 nm range.

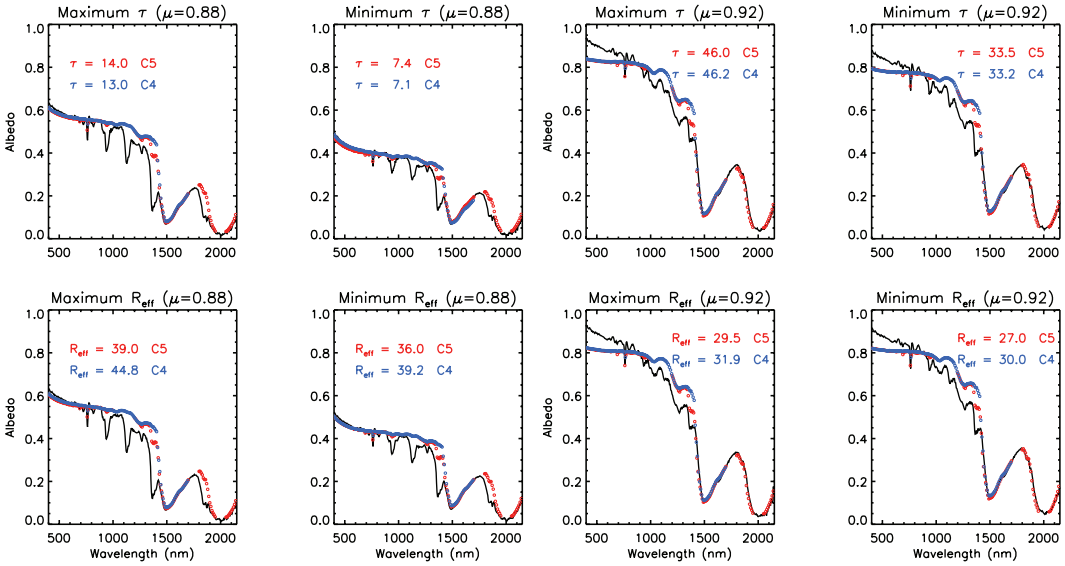

Figure 4.7: Same as Figure 4.6 but for the cases μ=0.88 and μ=0.92.

The effective radii for the C5 based retrieval are smaller in general than those from C4. The optical thicknesses are generally greater for C5 than C4. This is in agreement with a comparison done for the MODIS 4 and MODIS 5 collections (based in part on C4 for MODIS 4 and C5 for MODIS 5) by *Yang et al.* [2007] that showed average optical thickness is greater by 1.2 from C5 (MODIS 5 collection) and an average greater effective radius from C4 (MODIS 4 collection) of 1.8 μm

4.5 Comparison of irradiance and radiance derived optical properties

The comparison of irradiance measurements (SSFR) and radiance (MAS) is challenging for several reasons. Perhaps the greatest of these is the difference in spatial sampling of the cloud field. MAS measures radiance over a finite swath width, 37 km at the ground. The SSFR measures the cosine weighted radiance integrated over the upward and downward hemispheres centered at the aircraft. To compare measurements from the two instruments the MAS radiance was spatially averaged following the analysis of *Schmidt et al.* [2007]. The technique averages MAS radiance over the half power point of the SSFR signal. The diameter of the SSFR half power point is approximately the MAS swath width, 17 km for a cloud deck at 10 km and an ER-2 altitude of 20 km. Figure 4.8 shows the retrieved MAS optical thickness and effective radius from μ=0.88. The circle overlying the left part of the image represents the half-power region of an SSFR measurement. For the time series of retrieved optical properties, Figure 4.8, the circle was stepped down the image by one scan line, and a new average calculated. This time (flight) series of averages are compared for the two different instruments. Unlike the SSFR, which uses measured downward irradiance to calculate the albedo, the MAS-derived reflectance relies on absolute radiometric calibration and a top-of-atmosphere solar irradiance spectrum.

In Figure 4.9 the time series of retrieved optical thickness and effective radius are

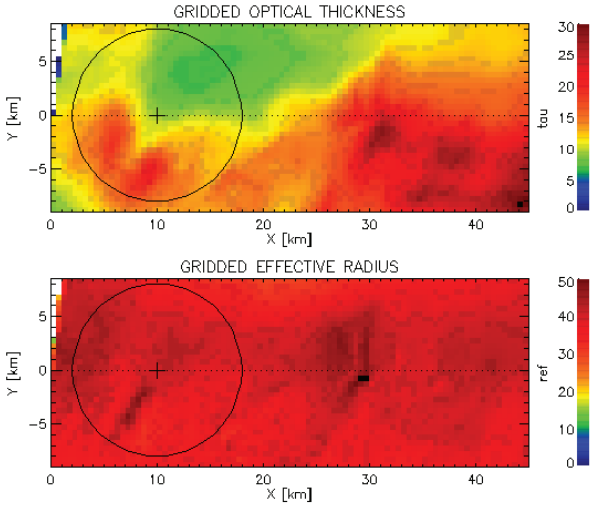

Figure 4.8: The MAS retrieval of optical thickness and effective radius are shown (μ=0.88) with the SSFR half-power point (circle) overplotted.

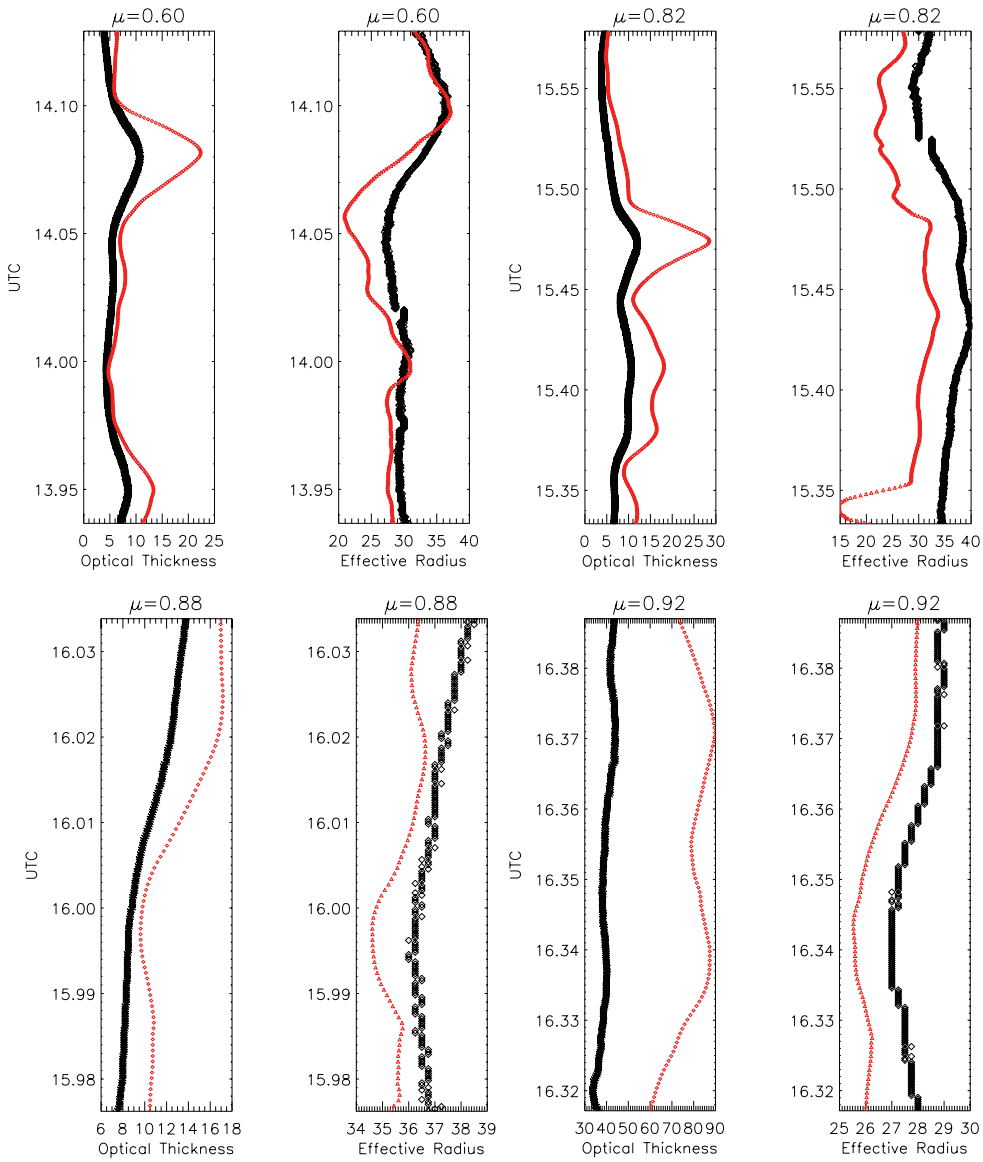

Figure 4.9: The time series of optical thickness and effective radius retrieved by SSFR (black) and MAS (red) are shown for the four cases.

shown for the four cases. For all cases, MAS optical thickness retrievals are greater than those from SSFR; conversely, effective radius retrieved by SSFR is nearly always greater. Because SSFR views an entire hemisphere, in nearly all cases this includes some unknown fraction of open water. GOES visible imagery near coincident with the flight of the ER-2 confirms that this was the case for the three moderate optical thickness cases. This may explain the consistent bias of higher optical thickness retrieved by MAS relative to SSFR. In general these differences are small; the average difference is 2-3 in optical thickness and 2-3 μm in effective radius. For short periods of time the differences can reach up to 12. The largest absolute difference occurs in the high optical thickness case μ=0.92. The GOES image for the high optical thickness case had a much more extensive and uniform cloud field and spatial sampling differences is a less likely explanation for the differences between MAS and SSFR. As the optical thickness increases, the albedo approaches its asymptotic limit. This means that small changes in albedo or reflectance (or radiometric calibration) produce large changes in retrieved optical thickness. This is consistent with the finding here that the largest differences in optical thickness were found at relatively high values of optical thickness. For the high optical thickness case, a 10% change in the SSFR irradiance (10% reduction in downwelling irradiance or a 10% increase in the upwelling irradiance or some combination thereof) is needed to bring it into general agreement with the MAS measurements of optical thickness. A summary of the average differences between the irradiance- and radiance-based retrievals and their standard deviations is given in Table 4.1. The 5% SSFR uncertainty has been propagated in the retrieval to estimate the uncertainty range of the optical thickness and effective radius derived from the SSFR measurements. The MAS uncertainties, expressed as percentages, were averaged in the same way that the values of optical thickness and effective radius were and a grand average of the flight track for each case is quoted. For the moderate optical thickness cases the MAS uncertainties in optical thickness are approximately 20%. For the high optical case the uncertainty reaches 99%. This

is a result of the large retrieval sensitivity in that part of the optical thickness space (e.g. [*Pincus et al.*, 1995]) and should not be taken as quantitatively meaningful. The uncertainties for MAS effective radius are 7-10 μm in all cases. The uncertainties for both MAS and SSFR are included in Table 4.1.

The variability of optical thickness and effective radius over a flight segment is higher for MAS, indicating that even after averaging the MAS values, the radiative smoothing from SSFR is greater still. This is not unexpected, as a large fraction of the energy incident on the SSFR originates from outside the swath of MAS. In addition, because the effects of scattering are more pronounced at the shortest wavelengths (conservative scattering), the variation in retrieved optical thickness is greater due to a greater contribution to the signal from outside the view of MAS. Figure 4.10 shows the differences between measured spectral albedo from SSFR from modeled spectral albedo derived using the MAS-retrieved optical thickness and effective radius. The differences are greater than those derived from the 2-wavelength SSFR retrievals (Figure 4.5). The bias in optical thickness retrieval produces a MAS-derived spectral albedo that is generally higher in the visible. For the moderately absorbing spectral region from 1500 to 2100 nm the differences are reduced and are generally within 0.05; for μ=0.88 case the differences are even lower, between 0.01-0.02. Condensed water is weakly absorbing at these wavelengths so scattering is reduced, resulting in smaller contributions from outside of the MAS swath and better agreement. This is likely scene dependent, with the presence or absence of clouds outside the MAS field of view also determining in part the level of agreement.

In Figure 4.11, the SSFR and MAS retrievals of optical thickness and effective radius are compared for each case. The order is sequential in cosine of solar zenith angle: the top row is μ=0.60, the bottom row μ=0.92. The left column shows comparisons of retrieved optical thicknesses, the middle column the retrieved effective radii, and the right column ratios of the effective radii retrieved by SSFR to that retrieved by

Table 4.1: Summary of Optical Thickness and Effective Radius for the Four Cases.

(μ)	MAS Optical Thickness	MAS Effective Radius	SSFR Optical Thickness	SSFR Effective Radius	Optical Thickness Difference (SSFR-MAS)	Effective Radius Difference (μm)	SSFR Optical Thickness ±5% Mean Uncertainty	SSFR Effective Radius ±5% Mean Uncertainty	MAS Optical Thickness Mean Uncertainty (%)	MAS Effective Radius Mean Uncertainty (%)
0.60	8.29 (4.39)	27.95 (4.05)	5.63 (2.02)	30.43 (2.53)	-2.67 (2.55)	2.48 (2.50)	5.17-6.15	29.26-31.31	20.0	7.9
0.80	12.40 (5.53)	27.53 (4.55)	7.64 (2.47)	30.57 (3.06)	-4.85 (3.32)	3.04 (3.11)	8.82-10.47	29.45-31.80	20.2	10.6
0.88	12.92 (2.96)	35.74 (0.63)	10.19 (2.07)	36.93 (0.63)	2.73 (1.07)	1.19 (0.43)	9.58-11.11	35.66-38.17	18.5	7.2
0.92	80.42 (7.47)	26.63 (0.89)	39.92 (2.65)	27.91 (0.70)	-40.48 (1.30)	1.28 (0.07)	32.44-53.24	26.77-29.03	99.4	8.4

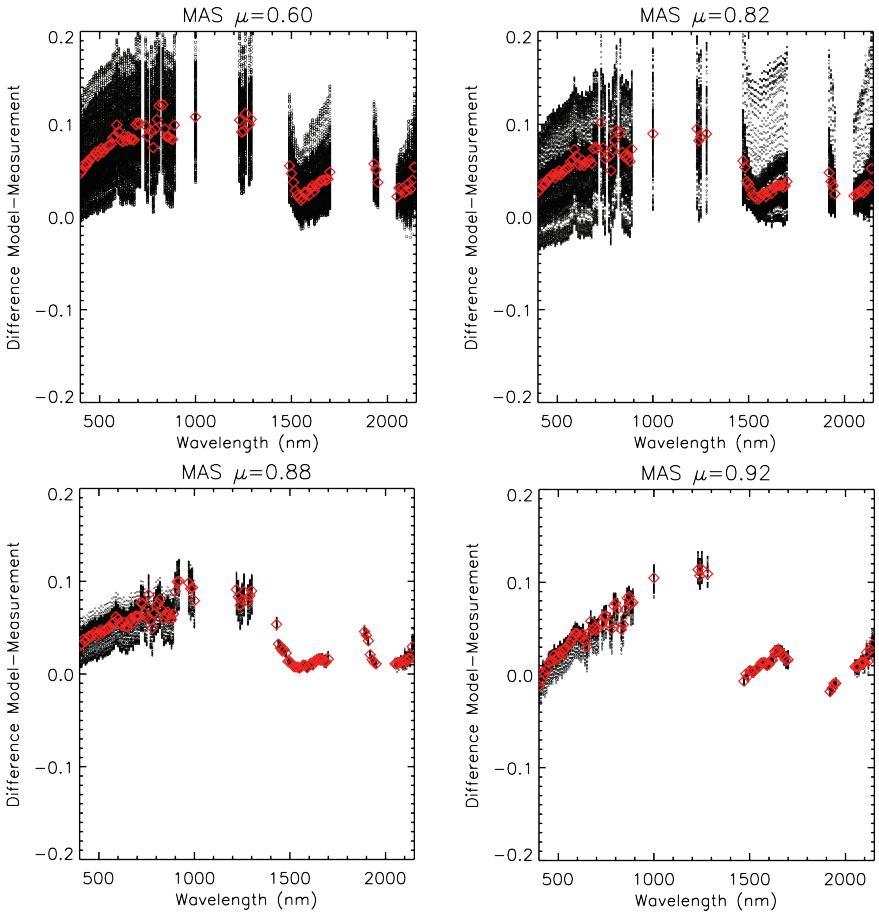

Figure 4.10: For each of the four cases the differences between modeled (C5) and measured albedo using MAS-derived optical thickness and effective radius are shown. The black dots are the differences for every line in the MAS flight track, and the red diamonds are the mean differences.

MAS plotted against the retrieved optical thickness from MAS. The plots of retrieved optical thicknesses show a bias of higher optical thickness retrieved from MAS; this bias increases as the optical thickness increases. This is most evident in the last row (μ=0.92) where the optical thicknesses are 3-4 times greater than those in the other three cases and deviation from the one to one line is substantial. The effective radius plots (center column), also indicate a bias, as was stated previously, of larger effective radii retrieved by SSFR. In the effective radii ratios versus optical thickness (right column), for optical thicknesses less than 20 the differences in effective radii are large, up to 50%, (excluding the brief departure of 200% in the μ=0.82 case which may be the result of underlying liquid water clouds). As the optical thickness increases the agreement in effective radius becomes better. This is true in every case, even the high optical thickness case (μ=0.92) which agrees to within 10% at an optical thickness of 60 and is within 5% at an optical thickness of 90. For all cases, the agreement is 10% or better when the optical thickness is 22 or greater. For low optical thickness, the influence of surface albedo (dark ocean) is greater, biasing the results to a larger effective radius. The MAS retrieval of cloud optical properties, because it is spatially resolved, rejects pixels that are cloud free. As optical thickness increases, in relatively planar ice clouds, the effects of cloud heterogeneity and surface albedo are less important and the agreement becomes better. Despite the differences in the spatial averaging, and potential differences in radiometric calibration, the MAS retrievals reproduce the observed spectral albedo to within 0.10 across the entire spectrum. In the most spatially uniform case (μ=0.88) the differences are considerably smaller. A radiometric offset between SSFR and MAS would also contribute to the differences in the retrievals between the two instruments. Similar comparisons to those presented in this study could be made with MODIS coverage to provide a better spatial context with which to judge the total contribution of cloud to the SSFR signal but would be hampered by differences in temporal sampling. The coincidence of satellite, aircraft, and cloud conditions did not allow for such a comparison

in this study.

4.6 Summary

Optical remote sensing of the microphysical and optical properties of ice clouds from satellites has focused on the retrieval of the two cloud properties necessary, but not always sufficient, to completely specify the inputs into radiative transfer models to recreate the spectral albedo: cloud optical thickness and effective cloud particle radius. These retrievals ultimately rely on models of bulk ice cloud single scattering properties of ice particles to determine the values of optical thickness and effective radius. If the single scattering parameters are correct or at least spectrally consistent and the retrieval is robust, then the retrieval results can be used in radiative transfer models to correctly model the complete spectral albedo.

In the first part of this work, a test of the ice crystal single scattering properties used in MODIS Collection 4 and Collection 5 ice scattering libraries was performed. The optical thickness and effective radius were retrieved using a two-wavelength fit similar to that used by satellites (MODIS) or its airborne proxy (MAS). The retrieved values were derived from the SSFR measurements to remove biases due to spatial sampling differences between SSFR and MAS. In addition, SSFR measured upwelling and downwelling irradiance, reducing the errors that might occur from absolute radiometric calibration errors. This was a more rigorous test of the model ice single scattering properties. The retrieved effective radius and optical thickness were subsequently used to predict the measured spectral albedo. The measured and modeled spectral albedo were found to be in very good agreement, especially for the longer wavelengths (1500-2100 nm) where the albedo differences were within 0.02-0.03 over the four flight segments, with a range in effective radius from 25 to 40 μm. The optical thicknesses showed larger differences, yet produced differences between modeled and measured albedo spectra that were within 0.05.

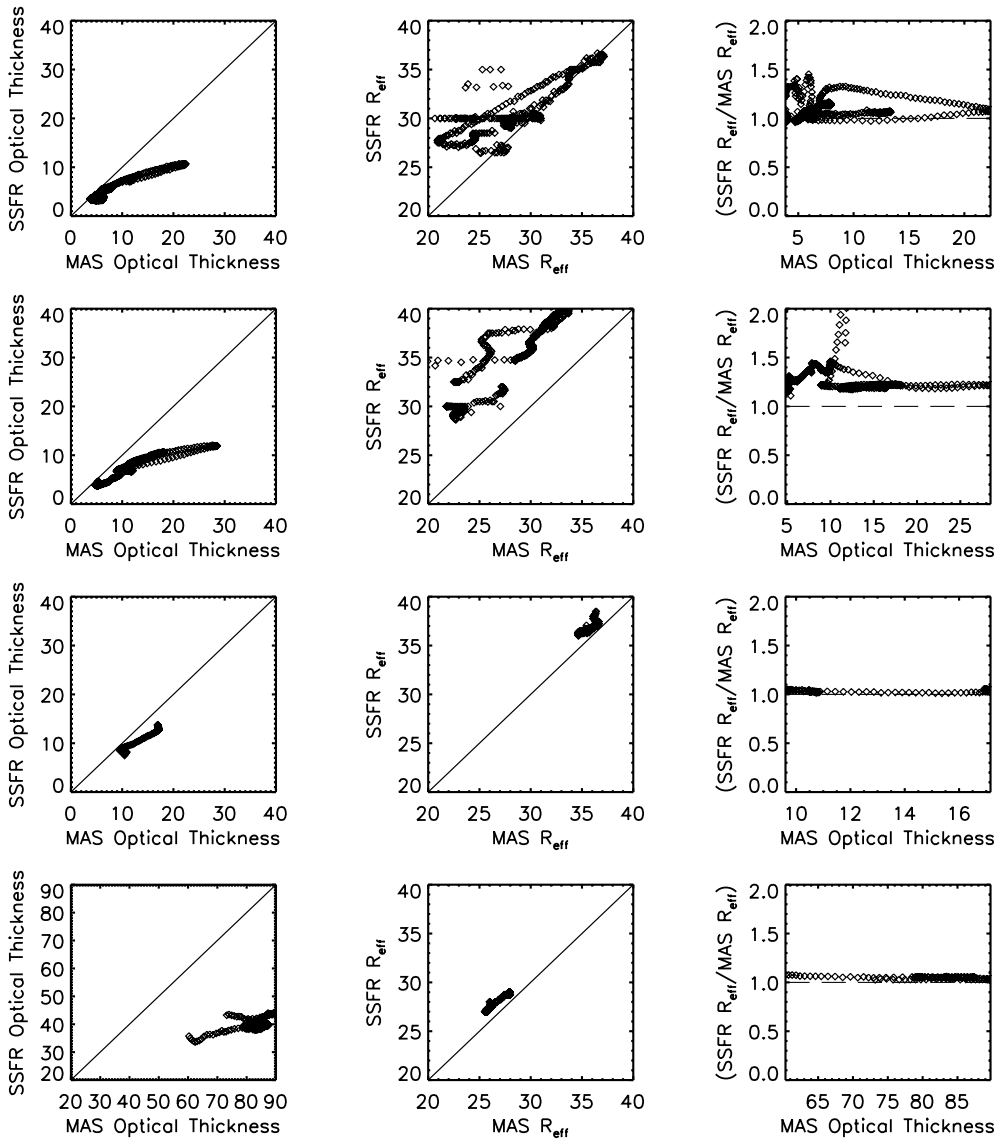

Figure 4.11: Optical thickness and effective radius as retrieved by SSFR and MAS are plotted against each other as is the ratio from SSFR and MAS against optical thickness. The first row is μ=0.60, the second row μ=0.82, the third row μ=0.88, and the fourth row μ=0.92.

In general the disagreement was largest at shorter wavelengths, up to 0.09 for the high optical thickness case (μ=0.92). Examination of lidar data for this case did not contain evidence of aerosol above the cloud layer. The spectra for the three lower optical depth cases show good agreement in the shortest wavelengths indicating that the molecular scattering was likely correctly calculated in the radiative transfer model. Ice scattering properties may be a source of error although at lower optical thickness the model and measurements agree quite well. Another possible explanation for the discrepancy is the effect a spherical atmosphere which is not accounted for in the calculations performed in this study [*Loeb et al.*, 2002]. This will be investigated with a radiative transfer code that includes the effects of a spherical atmosphere. In any case, it is difficult to draw a firm conclusion based on a single high optical thickness case.

The greatest systematic discrepancy between the measurements and models was for the wavelength region between 1200 nm and 1300 nm. In the lowest optical thickness cases the agreement was consistent with adjacent spectral bands. As the optical thickness increased, the differences were more pronounced. In the highest optical thickness case, the albedo bias approached 0.10. The increasing error with increasing optical thickness may suggest that the model single-scattering albedo is too high in this spectral region. The increase in multiple scattering amplifies absorption and could lead to a discrepancy such as is seen here. The updated refractive indices for ice have not changed in the 1000 to 1300 nm spectral range with the new compilation of *Warren and Brandt* [2008] although the values have changed in longer wavelengths 1400 to 2200 nm spectral range. The reason for this discrepancy remains unresolved.

In the second part of this paper we examined the retrievals from MAS, a satellite-like sensor. The MAS retrievals of optical thickness and effective radius were used with the radiative transfer model to predict the spectral albedo. This is a more challenging task for two reasons: unlike the SSFR, the MAS instrument relies on its absolute radiometric calibration to accurately predict reflectance and to determine optical thickness

and effective radius. It also measures radiance over a finite swath width, whereas SSFR measures irradiance over a hemisphere. This introduces spatial sampling differences which cannot be completely resolved. Nevertheless, averaging the derived optical properties over the half-power point of SSFR, reproduces the majority of spectral albedo to within 0.05 with the greatest differences occurring in the 400-1200 nm wavelength range where scattering is greatest and the differences in spatially sampling are exacerbated. For the longer wavelengths, greater than 1500 nm, the agreement is better, in the range of 0.03 or less. A comparison of the retrieved optical thickness and effective radius from SSFR and MAS shows an average absolute deviation of 2.76 in optical thickness and 2.24 μm in effective radius for the three cases of low to moderate optical thickness. The high optical thickness case shows a much greater difference of 40.5 in optical thickness and 1.3 μm in effective radius. At these high optical thicknesses, the retrieval (optical thickness value) is highly sensitive to small changes in radiance (irradiance) as albedo reaches its asymptotic limit. The differences are systematic between MAS and SSFR with MAS nearly always retrieving a higher optical thickness and SSFR nearly always retrieving a larger effective radius. This could be explained by a radiometric calibration error; small differences in the radiometric calibration would produce the largest changes in optical thickness when optical thickness is already high. Additionally, the SSFR hemispherical field of view nearly always includes some fraction of open water. Examination of GOES satellite data confirmed this was the case for the three low to moderate optical thickness cases. This would also lead to SSFR retrieving a smaller optical thickness and a larger effective radius compared to MAS. The high optical thickness case showed a more extensive cloud field and open water within the view of the SSFR instrument was reduced or absent. Spatial sampling differences prevent any definitive answer to this discrepancy, and in any case, the overall effect was relatively small when calculating spectral albedo.

The role of single scattering properties of ice crystals are crucial in satellite retrievals of ice cloud properties and ultimately for radiative transfer calculations and their

inclusion in ice cloud modeling in climate models. We have examined here the spectral consistency of these properties within the solar spectrum and over a range of solar zenith angles and optical thicknesses encountered during TC^4. We have validated the fidelity of the derived properties of optical thickness and effective radius based on ice single scattering properties to recreate the spectral albedo when used in a radiative transfer model. Spectral irradiance is the fundamental unit of energy balance; by comparing multispectral retrievals of cloud optical thickness and effective radius, with hyperspectral irradiance we can be confident that the ice single scattering properties are robust. These calculations are of importance for cloud radiative budget studies and ultimately climate models. It is through tests such as the one performed here that we can be confident that satellite retrievals of optical thickness and effective radius can be accurately extrapolated to spectral albedo for the entire solar spectrum. New models from the same authors of the single scattering properties used here have been developed for ice crystals with varying surface morphologies, from smooth to rough and substantially roughened ice crystals. These models will have continuous spectral sampling over the range of the SSFR instrument. They also include updated values for the ice optical constants. These new libraries will be compared with the same cases shown here to determine their ability to accurately reproduce spectral albedo and to examine the impact on the retrieval of ice cloud optical properties.

Chapter 5

Solar spectral absorption by marine stratus clouds: Measurements and modeling

The measurement of cloud absorption from aircraft has been a controversial subject largely because broadband measurements provide little insight into the physical mechanisms underlying the absorption. To partition and quantify the various mechanisms of cloud absorption, spectrally resolved measurements are required. Measurements of cloud solar spectral (400-2150 nm) absorption from airborne spectrometers are presented from two cases of extensive tropical marine stratus cloud fields. Radiative transfer modeling was used to retrieve the cloud optical thickness and cloud droplet effective radius from a best fit with the measured cloud spectral albedo. These values were used to estimate the cloud spectral absorptance. For the higher optical thickness case, the measurement-model agreement in absorptance across the spectrum is better than 0.05 and substantially better (within 0.01) at visible wavelengths unaffected by cloud absorption. For an optically thinner and more heterogeneous cloud field, the differences were higher, up to 0.07 in the near infrared. The standard deviations of cloud absorptance spectra show that the integrated absorbed irradiances, usually measured by broadband radiometers, are strongly affected by variations in the water vapor bands. Radiative transfer modeling is used to illustrate the spectral dependence of the absorption from radiatively important gases (e.g. water vapor), cloud liquid water, and absorbing aerosol particles. A novel sampling strategy, based on single aircraft measurements is demon-

strated as is the value of spectrally resolved measurements in partitioning the various mechanisms of cloud absorption including the possible effects of absorbing aerosols embedded in clouds.

5.1 Introduction

Cloud absorption has been a topic of debate from the earliest attempts at reconciling measurements with models of expected cloud absorption [*Fritz and MacDonald*, 1951]. Early studies indicated that clouds may absorb more solar radiation than predicted by models, or that the absorption-dependent retrieved cloud droplet size exceeded that measured in situ, the origin of the term anomalous absorption. *Stephens and Tsay* [1990] review the history surrounding cloud absorption as it was understood before the 1990s. Later in the mid 1990s the debate around how much solar radiation clouds absorb was again brought to the fore with several publications claiming evidence of much larger than expected absorption by clouds [*Cess et al.*, 1995, *Ramanathan et al.*, 1995, *Pilewskie and Valero*, 1995]. Soon afterwards, studies were published that either supported the existence of anomalous absorption [*Valero et al.*, 1997, 2000, *Zhang et al.*, 1997, *O'Hirok et al.*, 2000, *O'Hirok and Gautier*, 2003] or rejected the existence of any unaccounted for absorption in clouds [*Hayasaka et al.*, 1995, *Arking*, 1996, *Stephens*, 1996, *Taylor et al.*, 1996, *Francis et al.*, 1997, *Ackerman et al.*, 2003].

Explanations for a measured cloud absorption bias have focused on several possibilities. Horizontal transport of photons (i.e. cloud 3-D effects) introducing biases in the measurements of cloud absorption [*Newiger and Baehnke*, 1981, *Rawlins*, 1989, *Marshak et al.*, 1999, 1998], the inclusion of absorbing aerosols in the cloud mixed either externally or internally with cloud particles [*Chylek et al.*, 1984, *Chylek and Hallett*, 1992, *Chylek et al.*, 1996, *Wendisch and Kiel*, 1999], the existence of large drops in the cloud [*Wiscombe et al.*, 1984], and enhanced water vapor absorption or water vapor continuum absorption [*Li et al.*, 1997, *Arking*, 1999, *Stephens and Tsay*, 1990] are a few examples.

Nearly all measurements of cloud absorption to date have utilized broadband radiometers, sometimes paired with a single visible channel filter radiometer to mitigate the effects of net horizontal photon transport [*Ackerman and Cox*, 1981]. *King et al.* [1990] expanded the wavelength sampling to include thirteen channels spread throughout the solar spectrum to measure cloud absorption but radiance rather than irradiance was measured in that study. Their results supported little excess unaccounted for (anomalous) cloud absorption, and was the first attempt to spectrally resolve absorption properties in extended water clouds.

More recently, with the development of radiometrically stable airborne spectrometers, spectrally resolved, contiguous measurements of cloud absorption over the majority of the solar spectrum have been made [*Schmidt et al.*, 2010]. Spectrally resolved measurements of cloud absorption allows for the attribution of the various components of cloud absorption [*Pilewskie and Valero*, 1995], namely cloud liquid or ice water absorption, water vapor and other gaseous absorption, and aerosols if they are present. Broadband measurements are fundamentally incapable of distinguishing the various contributions to cloud absorption because they provide only a single integrated value of absorbed irradiance.

The measurement of cloud absorption, or vertical flux divergence, from airborne radiometers has been traditionally carried out with stacked aircraft, each carrying upward and downward looking radiometers. During the Tropical Composition, Cloud and Climate Coupling (TC^4) Experiment [*Toon et al.*, 2010], stacked flights of the NASA ER-2 (high altitude) and NASA DC-8 (lower altitude) was undertaken for various clouds types. Both aircraft were equipped with Solar Spectral Flux Radiometers (SSFR) [*Pilewskie et al.*, 2003]. In a related TC^4 study *Schmidt et al.* [2010], reported the results from an ice cloud case. The spectral dependence of apparent ice cloud absorption was identified and 3-D radiative transfer modeling of the cloud scene was undertaken to explain both the observed absorption spectrum and point by point single wavelength

absorption time series from the two aircraft during stacked flight. Ice clouds are perhaps more challenging to measure and to model than liquid water clouds because of their inherent heterogeneity and because ice particle single scattering properties cannot be derived from Mie theory. Ice particle single scattering properties rely on numerical calculations of the phase function and single scattering albedo [*Yang and Liou*, 1998], and use a variety of representative ice particle shapes that are combined into representative ice particle mixtures [*Baum et al.*, 2005]. Contrastingly, liquid water clouds are modeled as spheres with Lorenz-Mie theory, an exact solution of the scattering and absorption for a given sphere radius and complex index of refraction of liquid water.

During TC^4, the NASA aircraft also sampled low-level marine stratus. Marine stratus clouds are climatically important because they cover large regions of the Earth's oceans, they are typically optically thick and persistent, and they occur at low altitude, thus strongly influencing the planetary albedo with only a weak greenhouse (infrared) warming effect. Low-level tropical stratus were identified as having the largest impact on net cloud forcing [*Hartmann et al.*, 1992] of the various clouds types categorized in that study. Large marine stratus systems are as close to an ideal homogenous cloud system that occurs, making them amenable to simpler and faster plane parallel radiative transfer calculations. The influence of surface (in these cases, open ocean) albedo is uniform and small [*Chiu et al.*, 2004]. Errors due to cloud 3-D effects (net horizontal divergence) are substantially reduced for a marine stratus layer of large horizontal extent with no overlying higher-level clouds provided that the clouds are well sampled by the aircraft [*Oreopoulos et al.*, 2003]. Likewise, the cloud particle single scattering properties can be readily calculated from Mie theory over all of the wavelengths measured by the SSFR.

In this paper we report the cloud layer spectral absorption from two large marine stratus cloud complexes encountered during TC^4. In one case the NASA DC-8 flew above, in and below the cloud deck, while the NASA ER-2 flew above the cloud deck. In the second case, only the DC-8 sampled the cloud. We present a technique for estimating

cloud absorption from a single aircraft based on the method of conditional sampling proposed by *Marshak et al.* [1999] and show that for the case of stacked aircraft with large vertical separation (as was the case with the DC-8 and ER-2 for these marine boundary layer clouds) that single aircraft measurements can give a more reliable estimate of the true cloud absorption. Detailed plane parallel radiative transfer model calculations combined with Mie calculations of cloud droplet optical properties are compared over the complete spectral wavelength range of the SSFR for both cases. Neither of these two cases exhibited any substantial absorption from aerosols mixed in the cloud layer. We present results from a model of absorbing aerosol embedded in a cloud layer to demonstrate the expected spectral signature and magnitude of absorption from aerosols.

The structure of the paper is as follows: i) the SSFR is described and its use during TC^4 outlined, ii) two examples found suitable for flux divergence measurements of marine stratus are described from TC^4 and the sampling strategy is described, iii) radiative transfer modeling of the marine stratus clouds is described, iv) detailed comparisons between model and measurements of cloud absorption are presented, v) the expected effects of an absorbing aerosol embedded in a cloud layer are presented, vi) summary and conclusions.

5.2 The Solar Spectral Flux Radiometer

The Solar Spectral Flux Radiometer measures upwelling and downwelling spectral irradiance from 350 to 2150 in more than 400 contiguous spectral channels. The instrument consists of two spectrometers, one for the visible to very near-infrared (350-1000 nm) and one for the near and shortwave-infrared (1000-2200 nm). The spectrometers are connected by a fiber optic bundle to miniature integrating spheres mounted on the top and bottom of the aircraft. The integrating sphere provides the necessary cosine response over the wide range of wavelengths measured by the SSFR. The spectrometers were radiometrically calibrated in the laboratory with a NIST traceable standard

of spectral irradiance. The calibration was frequently tracked after integration into the aircraft with a field calibration unit over the duration of the experiment. Over numerous field campaigns the SSFR has demonstrated the ability to maintain its absolute radiometric calibration to 1-2% level over the duration of a field experiment, typically one month, as it did during TC^4. For a more complete description of the instrument the reader is directed to *Pilewskie et al.* [2003]. The estimated accuracy of the SSFR, from uncertainties in the absolute radiometric calibration, instrument attitude, and angular response is 7% [*Schmidt et al.*, 2010]. The conditional sampling strategy, described in section 5.4, likely reduces this value to the level of the precision of the instrument, 0.5

5.3 Marine stratus cases

During the TC^4 experiment several flights encountered large marine stratus systems. The DC-8 flew both above, in, and below these stratus systems for extended periods of time. Two such systems, identified from the forward video data from the DC-8 were identified as being excellent case studies for cloud spectral flux divergence measurements. They were large in horizontal extent, relatively homogenous, and with no high-level clouds overhead that would make the interpretation of flux divergence more difficult. Figure 5.1 shows representative images of the clouds viewed from above and below as seen from the DC-8 forward camera. In both cases the DC-8 flew for extended periods (50 km or more) above and below the cloud deck. The cases identified occurred on 29 July 2007 (Figure 5.1) and 6 August 2007 over the eastern tropical Pacific Ocean. The cases will be referred to as the 29 July or the 06 August case for the remainder of the paper. On 29 July in addition to the DC-8, the ER-2 flew over the clouds in near stacked formation with the DC-8 underneath the cloud deck. The mean solar zenith angle for the above cloud measurements was approximately 38° (μ=0.792) for the 29 July case and 43° (μ=0.731) for the 06 August case. Figure 5.2 shows the mean SSFR albedo spectrum with ± one standard deviation for the two cases.

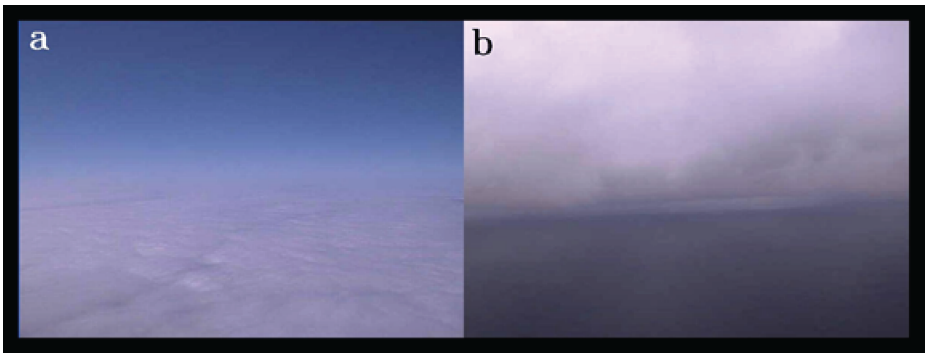

Figure 5.1: Images taken from the NASA DC-8 forward video camera above (a) and below (b) the marine stratus cloud deck encountered on 29 July 2007 during TC^4.

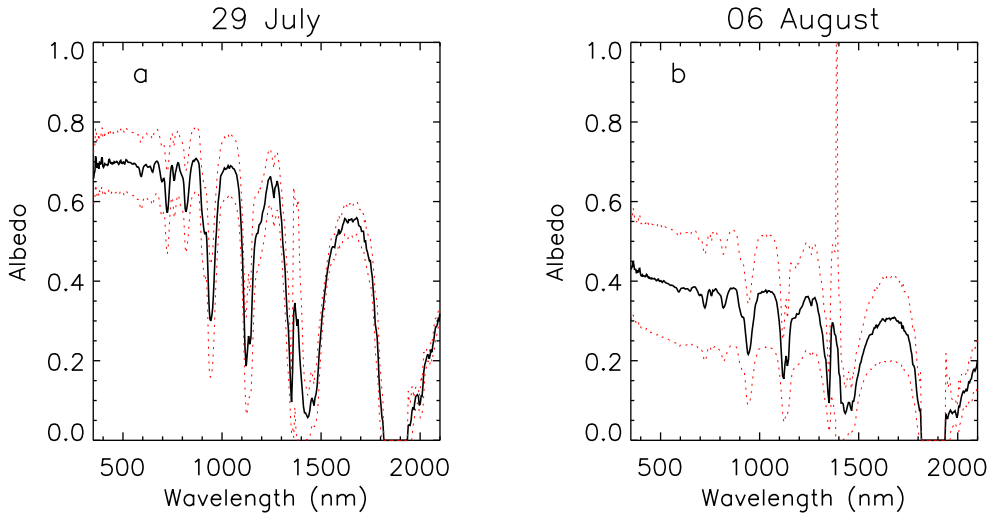

Figure 5.2: The mean (solid black lines) and ± one standard devaition (dashed red lines) SSFR albedo spectra are plotted for the two cases. The 06 August case was thinner and more heterogeneous, thus the higher variations in the measurements.

5.4 Sampling strategy for cloud absorption measurements

The measurement of cloud absorption, or flux divergence, is usually performed with coordinated stacked flight of aircraft positioned above and below the cloud deck. The 1-D flux divergence (F_{div}) of a cloud layer is obtained by differencing the net flux above and below the cloud layer:

$$F_{div} = F_{net,above} - F_{net,below} = (F_{\downarrow above} - F_{\uparrow above}) - (F_{\downarrow below} - F_{\uparrow below}) \tag{5.1}$$

In this paper we also report spectral absorptance, the result of normalizing equation 5.1 by the downward irradiance above-cloud:

$$Absorptance = \frac{(F_{\downarrow above} - F_{\uparrow above}) - (F_{\downarrow below} - F_{\uparrow below})}{F_{\downarrow above}} \tag{5.2}$$

In theory, the measurement is simple; in practice, obtaining robust results has proven problematic. Equations 5.1 and 5.2 represent true cloud absorption only when horizontal flux divergence vanishes, as it does in horizontally homogenous and semi-infinite plane layers. Clouds are never homogenous, nor are they infinite. Non-vanishing horizontal divergence leads to errors in estimating true absorption from vertical flux divergence. Several authors have examined how to best estimate cloud absorption in the presence of cloud inhomogeneity [*Ackerman and Cox*, 1981, *Marshak et al.*, 1999, *Titov*, 1998]. Some [*Valero et al.*, 1997, *Ramanathan and Vogelmann*, 1997] have advocated averaging measurements over long flight legs (>50 km) to reduce cloud 3-D effects. Although averaging over flight tracks may reduce the 3-D induced absorption errors, there is no guarantee that it will [*Marshak et al.*, 1999].

An approach to correct absorption estimates proposed by *Ackerman and Cox* [1981] exploited the spectral behavior of bulk water absorption. A single wavelength irradiance measurement at a non-absorbing wavelength (e.g., 500 nm) was used to correct broadband measurements of cloud flux divergence. The underlying assumption was

that the effects of cloud inhomogeneities were strongly correlated for absorbing and non-absorbing wavelengths. *Marshak et al.* [1999] offered two variations based on the Ackerman-Cox type correction. The first proposed method was a point-by-point subtraction of "apparent" (i.e. due to cloud 3-D effects) absorption. The apparent absorption measured at the non-absorbing wavelength was used to remove the apparent absorption from the broadband measurements and the data were further refined with radiative smoothing theory to better obtain true absorption.

The second proposed method, called conditional sampling, essentially filtered the data to remove the net irradiances in a non-absorbing wavelength that exceeded the specified error threshold for above and below cloud net irradiances. Both of these techniques assumed stacked, two aircraft experiments. In our study, only the 29 July case employed two aircraft. The second aircraft was the ER-2 that flew at 20 km, far above these low level clouds ($\approx$1 km cloud top height). We will show that the difference in aircraft height introduces errors that result in non-physical negative absorption in the shortest wavelengths. Therefore, we have taken the conditional sampling approach and adapted it for use with a single aircraft.

In both cases, the DC-8 forward camera video data were examined to determine the suitable range of above-cloud and below-cloud data from the time series. This resulted in hundreds of downwelling and upwelling irradiance spectra from above and below the cloud layer acquired in series rather than parallel, as they would be in a stacked flight. From these, the net irradiance spectra, above and below cloud, were calculated and the conditional sampling technique was applied for all of the spectra. For the 29 July case, the DC-8 above cloud measurements started at 4.2 km above the cloud layer, for the 06 August case 2.5 km.

As an example, the 29 July case had 596 above cloud net irradiance spectra and 400 below cloud net irradiance spectra. All of the below cloud net spectral irradiances were compared to all of the above cloud net spectral irradiances, 238400 possible combinations,

and those that could be matched with a net irradiance difference no greater than 0.01 W m^{-2} nm^{-1} at 500 nm (the error tolerance) were retained. Those spectra were used to derive the statistics for the spectral absorption of the cloud layer. Instead of a time-flight series of absorption that would be produced with stacked flight, we produced a randomized sampling of the entire cloud scene. Using the rather stringent threshold value of 0.01 W m^{-2} nm^{-1} the 29 July case yielded 7345 flux divergence spectra from which statistics of cloud absorptance were derived. The same technique applied to the 06 August case resulted in 4118 flux divergence spectra. The use of a single aircraft has the advantage that the absolute radiometric accuracy is identical for both above and below cloud net irradiances, almost certainly not the case for a two aircraft experiment.

5.4.1 Observations of cloud spectral absorptance

Figure 5.3 shows the mean spectral absorptance and $\pm$ one standard deviation obtained following the modified conditional sampling technique outlined in the previous section (that is, data from the DC-8 aircraft only) for the two cases and using equation 5.2. The large absorption features that dominate these spectra at 724, 816, 940, 1140, 1400, and 1900 nm are due to water vapor. Smaller absorption features in the wavelength region less than 1000 nm are due to oxygen. Although ozone also absorbs in this spectral region, the concentrations of ozone at these altitudes are too low to produce measurable absorption. The 29 July case exhibits essentially zero absorptance throughout the visible portion of the spectrum as would be expected for a pure liquid water cloud. The single-scattering albedo of liquid cloud droplets is unity (non-absorbing) in the visible, departing from unity at wavelengths greater than about 900 nm. The expected effect of aerosols on the absorptance in the visible spectral region is considered in section 5.8. The 06 August absorptance spectrum shows a distinct slope and non-physical negative absorptance in the wavelength range 400-500 nm. These negative absorptances are small, approximately 0.025 at 400 nm and are within the measurement uncertainty. In

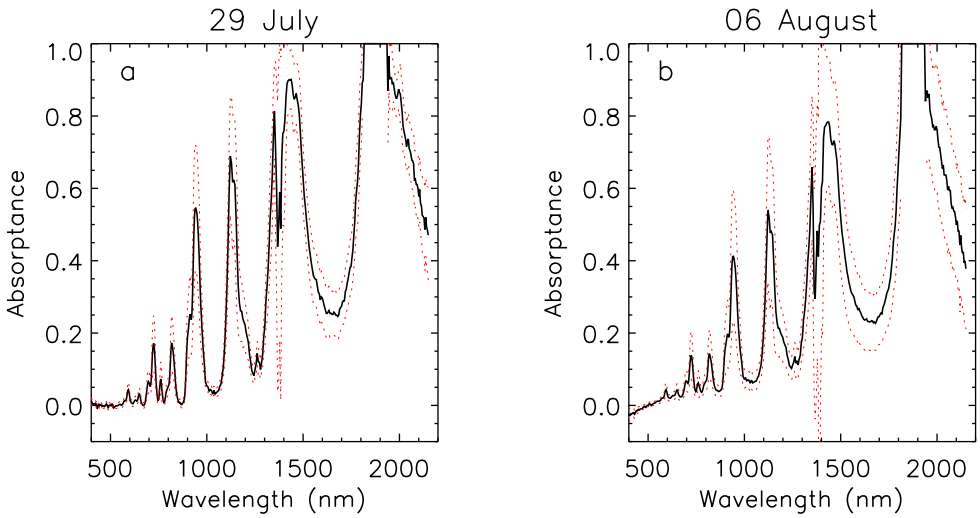

Figure 5.3: The mean (solid black lines) and ± one standard deviation (dashed red lines) SSFR absorptance spectra for the two cases are shown.

addition, the cloud field from 06 August was optically thinner than that from 29 July and contained more gaps. This can be seen in a plot of the albedo spectra from the two cases in Figure 5.2. The overall albedo on 06 August is considerably lower with a larger standard deviation, indicating an optically thinner, more heterogeneous cloud layer. The retrieved optical thickness for 06 August is several times smaller than 29 July as will be shown in section 5.6. The derivation of absorption from aircraft radiometric measurement, a difficult task at the start, is inherently more difficult for a thinner and more inhomogeneous cloud such as the one encountered on 6 August, so errors such as small negative absorptances are not surprising. Flux divergence is the small difference of four large quantities; the greater the absorption, the larger this difference. Additionally, the measurement is less sensitive to the effects of surface albedo for an optically thick cloud layer.

The slope across the visible part of the absorptance spectrum observed in the 06 August case has been observed previously. *Schmidt et al.* [2010] obtained a similar slope in high altitude ice cloud flux divergence measurements made with the SSFR during TC^4. Figure 5.4 shows the cloud absorptance derived from the DC-8 and ER-2 and the cloud albedo measured by the ER-2 for the same cloud scene on 29 July. The aircraft flew over identical geographical coordinates, with the ER-2 arriving a few minutes prior to the DC-8 and it completed its run a few minutes earlier. The same conditional sampling technique described above was performed for the stacked aircraft but the number of above and below cloud spectra meeting the sampling requirement was very small in comparison to the previous case using only the DC-8; only 87 spectral pairs were below the threshold. The absorptance and albedo spectra are plotted in Figure 5.4. Both the absorptance and albedo spectra are notably different from obtained from the DC-8 only. The absorptance spectrum contains much greater water vapor and oxygen absorption because the measured layer extended from below the cloud to the flight level of the ER-2, 20 km. At the shortest wavelengths, below 500 nm the absorptance is negative,

with a positive slope. This slope is similar to that seen in the 06 August case and to the ice cloud case from *Schmidt et al.* [2010]. No such slope is evident in the absorptance measurement derived from the low altitude DC-8 aircraft of the same cloud scene on 29 July (Figure 5.3(a)). Plane parallel radiative transfer modeling of pure liquid water clouds (to be shown) did not show any such absorption, as expected. Also noticeable is the slope in the visible from the albedo measurements, decreasing albedo with increasing wavelength (Figure 5.4(b)). This too has been observed previously in ice clouds during TC^4 [*Kindel et al.*, 2010]. Currently the explanation for this is unknown. Based on the observations of the same cloud from the DC-8, it would seem to be a geometrical or 3-D effect, and not related to true cloud absorption or albedo. One possibility is the effects of spherical atmosphere not explicitly accounted for in a plane parallel model is non-negligible at the ER-2 altitude of 20 km. This is currently an area of active investigation. The overall albedo of the cloud scene is somewhat lower than that measured by the DC-8. One plausible explanation is that at the ER-2 high altitude the much larger irradiance footprint may have extended over darker, open water, thus lowering the magnitude of albedo from its lower altitude DC-8 counterpart.

5.5 Radiative transfer modeling of cloud absorptance

Radiative transfer modeling of the cloud absorption was undertaken to determine the level of agreement between a state of the art radiative transfer model and the measured cloud absorptance spectra. The model used in this study was developed specifically for use with the SSFR and was designed to include cloud and/or aerosol layers. The molecular absorption by radiatively active gases (H_2O, O_2, CO_2, O_3, and CH_4) in this wavelength range (400-2200 nm) was computed using the correlated-k method [*Lacis and Oinas*, 1991]. The k-distribution was based on the HITRAN 2004 [*Rothman*, 2005] line-by-line spectral database and the model spectral resolution was matched to the slit function of the SSFR. The molecular scattering optical thickness was calculated using

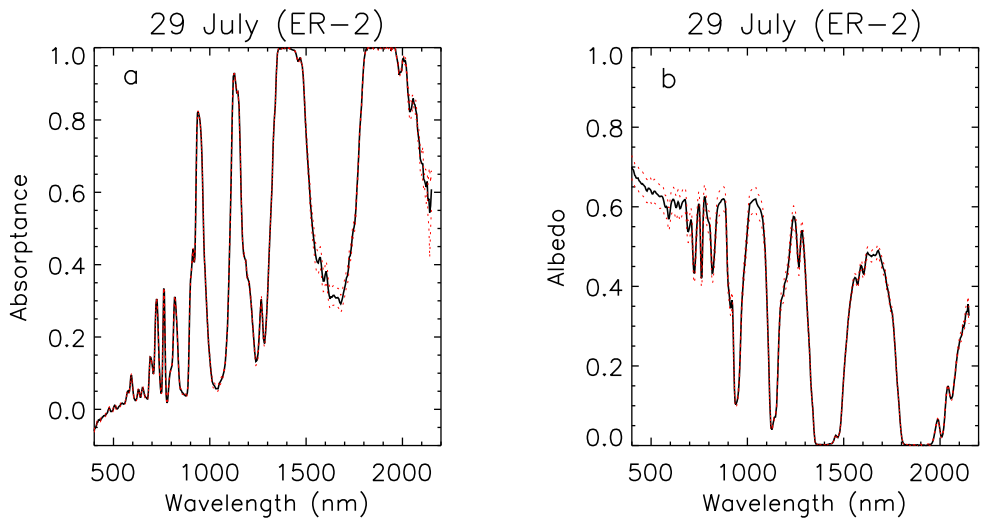

Figure 5.4: The mean (solid black lines) and ± one standard deviation (dashed red lines) for the absorptance (a) and albedo (b) for the 29 July case as measured by the ER-2. The DC-8 data were used for the under cloud measurements of absorptance.

the analytical method of *Bodhaine et al.* [1999]. The model computed the upwelling and downwelling spectral irradiance with DISORT [*Stamnes et al.*, 1988] at 36 predefined levels in the atmosphere. Levels lower in the atmosphere, including those with the cloud layer, were vertically spaced more closely than those high in the atmosphere. The model used a standard tropical atmospheric profile modified to include dropsonde data of the vertical profile of temperature, pressure, and relative humidity. Dropsonde data were taken only for altitudes below 11 km, the maximum altitude at which the DC-8 flew. Above this altitude standard tropical atmosphere data were used. The input sea surface albedo was taken from measurements on 29 July when the aircraft flew low over the ocean under clear skies. The modeling for the two cases presented here includes no aerosol. The expected effects of an absorbing aerosol on cloud absorption are examined in section 5.8. The cloud absorptance from the model was calculated in the identical way that it was calculated from the aircraft measurements: the net irradiance in the layers just above and below the cloud layer were differenced and then normalized by the downwelling irradiance from above the cloud. The cloud height and geometrical thickness were estimated from the DC-8 forward video data.

5.5.1 Mie calculations of cloud droplet optical properties

The single scattering properties of cloud liquid water droplets necessary for inclusion into the radiative transfer model are the single-scattering albedo (ϖ_0) and the phase function or its first moment, the asymmetry parameter (g). For irradiance calculations, an integrated value of (cosine weighted) radiance over all angles in a hemisphere, the asymmetry parameter was used with the Henyey-Greenstein phase function instead of a Legendre polynomial expansion of the phase function. The wavelength dependent values of single-scattering albedo, asymmetry parameter, and extinction were calculated from the Mie code that is a part of the SHDOM atmospheric radiative transfer software package [*Evans*, 1998]. The Mie code calculates the extinction, single-scattering albedo, and

the phase function from which the asymmetry parameter is derived for a given effective radius. For the results shown here, the calculation assumed a gamma distribution for the droplet size as is often done for clouds [*Hansen and Travis*, 1974] (and references therein) and a liquid water content of 1.0 g m^{-3}. The complex part of the index of refraction for liquid water is a composite of several sources depending on the wavelength interval [*Hale and Querry*, 1973, *Palmer and Williams*, 1974, *Downing and Williams*, 1975].

The Mie code was used to calculate the scattering properties for cloud droplet effective radii ranging from 5 to 30 μm in 1.0 μm increments. The wavelength sampling was every nanometer over the wavelength range of the SSFR. Figure 5.5 shows the resultant asymmetry parameter and single-scattering albedo spectra for the largest and smallest effective radii. Note the large change in the single-scattering albedo between the two sizes in the near-infrared (>1200 nm) that produces large changes in the near-infrared absoprtance spectra in wavelengths outside of water vapor absorption. The single scattering co-albedo is proportional to the drop size as expected from geometric optics [*Twomey and Cocks.*, 1982]. This can be seen in Figure 5.6, in which the resultant spectra from the radiative transfer code with the cloud Mie calculations are shown for the two effective radii with a large range (5-100) of optical thickness. For the small effective radius (Figure 5.6(a)), even an optically thick cloud of 100 does not produce any appreciable liquid water absorption for wavelengths less than 1600 nm. For the large effective radius (Figure 5.6(b)) the liquid water absorption can been seen to start at wavelengths greater than 1000 nm and produces very large changes in the absorptance spectra in wavelengths greater than 1600 nm. For the wavelengths less than 1000 nm, where the single-scattering albedo is essentially unity for all effective radii (Figure 5.5(b)), all absorption is due to either water vapor or oxygen.

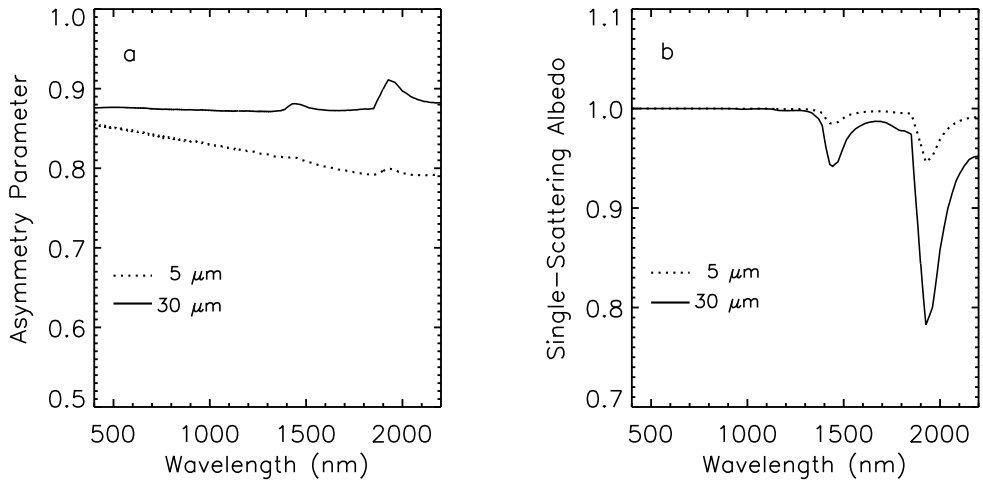

Figure 5.5: The asymmetry parameter spectra (a) for the smallest and largest effective radii used in the modeling are plotted on the left. On the right (b) are single-scattering albedo spectra for the same sizes.

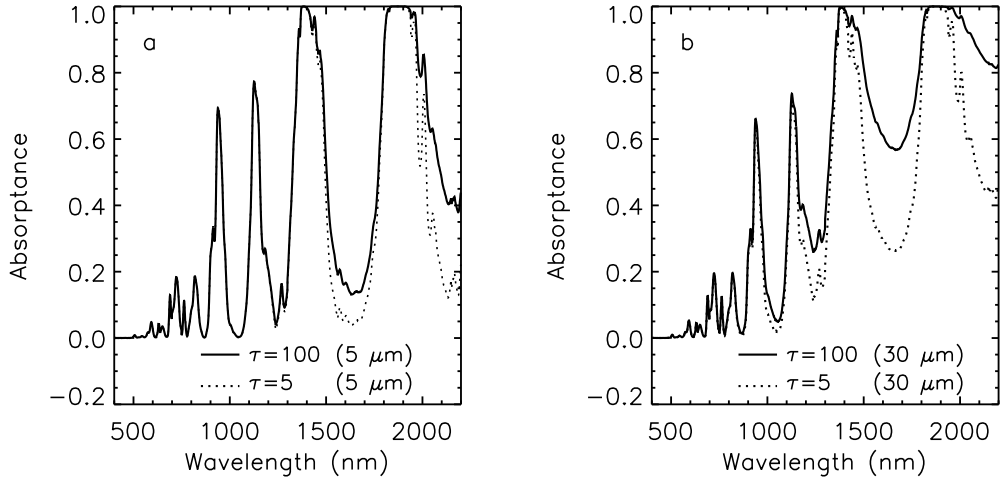

Figure 5.6: The range of modeled cloud absorptances due to the coupled effects of optical thickness and effective radius are shown. The absorptance for an effective radius of 5 μm and optical thickness of 5 and 100 are plotted on the left (a). The same plot but for and effective radius of 30 μm is shown on the right (b).

5.6 Retrieval of cloud optical thickness and effective radius

The comparison of cloud absorptance from the aircraft measurements and radiative transfer model calculations (e.g. those shown in Figure 5.6) requires that cloud optical thickness and effective radius be specified. The retrieval of optical thickness and effective radius is routinely done by satellite or aircraft measurements of reflected radiance [*Platnick et al.*, 2003, *King et al.*, 1992]. The retrieval relies on visible, or very near infra-red wavelengths for information on the optical thickness and near infrared water absorption features in the longer wavelengths [*Nakajima and King*, 1990, *Twomey and Cocks.*, 1982] for information on the particle size. Retrievals of optical thickness and effective radius have previously been done using SSFR irradiance [*Coddington et al.*, 2010, *Kindel et al.*, 2010]. Here we have followed a similar technique but with an expanded wavelength range to improve the match between measured and modeled albedo. The radiative transfer model was run at low spectral sampling (50 nm) over the SSFR spectral range and optical thicknesses from 1 to 100 with finer sampling at the lower optical thickness values. For each optical thickness the effective radius was varied from 5 to 30 μm in 1 μm increments. A least squares fit between the observed albedo and the model albedos were calculated for a subset of the wavelengths free of gaseous absorption. In Figure 5.7 the SSFR albedos are plotted with the results of the least-squares fit of the model. The best-fit model albedo values for the wavelengths used in the retrieval are plotted with black circles. Plotted in Figure 5.7(a) is the 29 July case albedo; the retrieval gave an optical thickness of 26 and an effective radius of 11 μm. Plotted in Figure 5.7(b) is the 06 August albedo and resulted in an optical thickness of 7 and an effective radius of 20 μm. The fit of the model to the measurement was quite good with a mean absolute deviation across the all retrieval wavelengths of 2% for the 29 July case. The 06 August was not quite as good (5.1%); as was pointed out previously the cloud was thinner and more heterogeneous which could explain the slightly larger discrepancies.

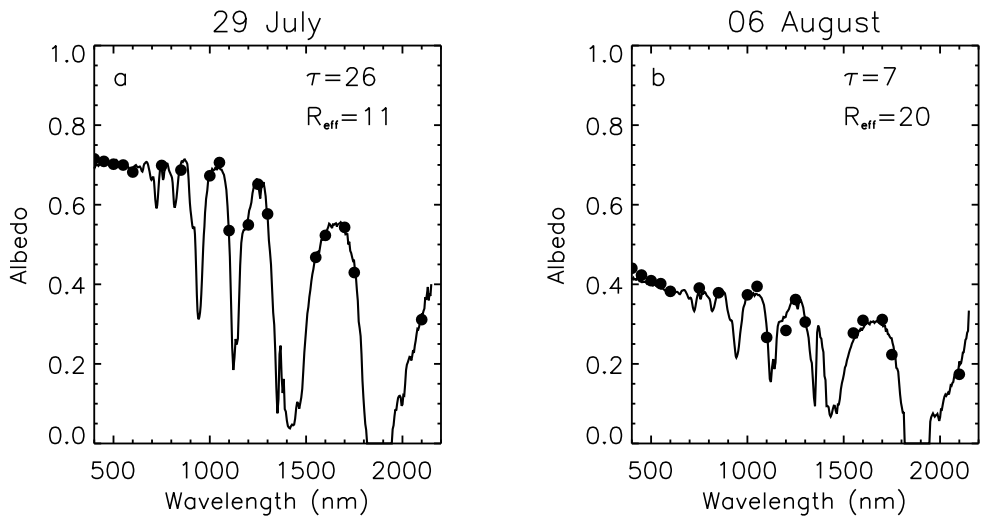

Figure 5.7: The mean SSFR albedo spectra are plotted (solid black line) for the 29 July (a) and 06 August (b) cases. The model albedo values for the 19 retrieval wavelengths are plotted with black circles. The retrieved optical thickness and effective radius is given in the upper right corner of each plot.

The optical thickness and effective radius for both of the cases presented here were also retrieved from the MODIS satellite and the MODIS/Advanced Spaceborne Thermal Emission and Reflection Radiometer (ASTER) Airborne Simulator (MASTER) for the two cases presented here [*King et al.*, 2010]. The optical thickness retrieved by MASTER and MODIS were significantly smaller, 13-14, for the 29 July case and somewhat higher , 11-12, for the 06 August case. The MASTER and MODIS imagery (see *King et al.* [2010]) of optical thickness for both cases indicate large portions of the flight line have optical thicknesses in closer agreement to the SSFR so this is likely a sampling issue related to where the DC-8 measurements were taken above the cloud layer. The MASTER and MODIS imagery of retrieved effective radius is far more homogenous in both cases and accordingly the effective radius retrievals are nearly identical to the SSFR retrievals, 10-11 μm, for the 29 July and 18-19 μm (within 1-2 μm of SSFR) for the 06 August case. This is typical of comparisons of optical thickness and effective radius retrievals when comparing SSFR and airborne MODIS simulator retrievals. A previous study of ice clouds from TC^4 showed similar results, with sometimes large discrepancies in optical thickness but generally very good agreement in effective radius [*Kindel et al.*, 2010]. The SSFR-retrieved (at course spectral resolution) optical thickness and effective radius were used to model the absorptance at much higher spectral sampling.

5.7 Comparison of measured to modeled cloud spectral absorptance

After determining the optical thickness and effective radius from the low spectral resolution model of albedo, the model was run at one nanometer sampling over the entire wavelength range for the two cases. These spectra were then convolved with the SSFR slit function for direct comparison with the measurements. In Figure 5.8, the mean SSFR absorptance spectrum and $\pm$ one standard are plotted with the results of the radiative transfer modeling (small diamonds). In Figure 5.9, the difference spectra (measurement minus model) are plotted.

The overall agreement is quite good, mostly within 0.05 in absorptance (outside of strong molecular absorbers like water vapor) and considerably better for the 29 July case. The 29 July case had much higher optical thickness, more than three times that of the 06 August case. The 29 July case was also more homogeneous as shown by the substantially lower variation in the albedo statistics (Figure 5.2). A thicker more homogenous cloud layer presents inherently more robust conditions in which to measure true cloud absorption, so better agreement with the model is expected for the reasons discussed in section 5.1. The spectral regions with the poorest agreement are those corresponding to water vapor bands. This is not unexpected, despite the use of dropsonde data to determine the water vapor profile. Water vapor is highly variable both spatially and temporally; the water vapor bands from the absorptance measurements demonstrate this with their large standard deviations. In any case, most of the modeled water vapor bands fall within one standard deviation of the measurements.

The visible spectral region, from 400 to 600 nm shows virtually no absorption with very small wavelength-to-wavelength standard deviations, less than 0.01. This agrees with the modeling that showed no absorptance (ϖ_0=1.0) regardless of effective radius or optical thickness. It also demonstrates the high precision of the instrument. Although these data have been selected to agree to 0.01 W m^{-2} nm^{-1}at 500 nm, this in no way guaranteed that the spectral shape (i.e. visible wavelengths greater than or less than 500 nm) should be so stable and agreed with the model to the level that it did. In wavelengths between 600 and 1000 nm the presence of weak water vapor and oxygen bands resulted in larger variations in the spectra, but in the atmospheric window region around 850-880 nm the absorptance again approached zero. In the wavelengths 1000-1200 nm where single-scattering albedo drops below one and cloud liquid water absorption begins, cloud liquid water absorption was somewhat greater than predicted from the model and outside the standard deviation of the measurements. In the longer wavelengths (1200-1300, 1500-1800, and 2000-2200 nm) the agreement was again quite

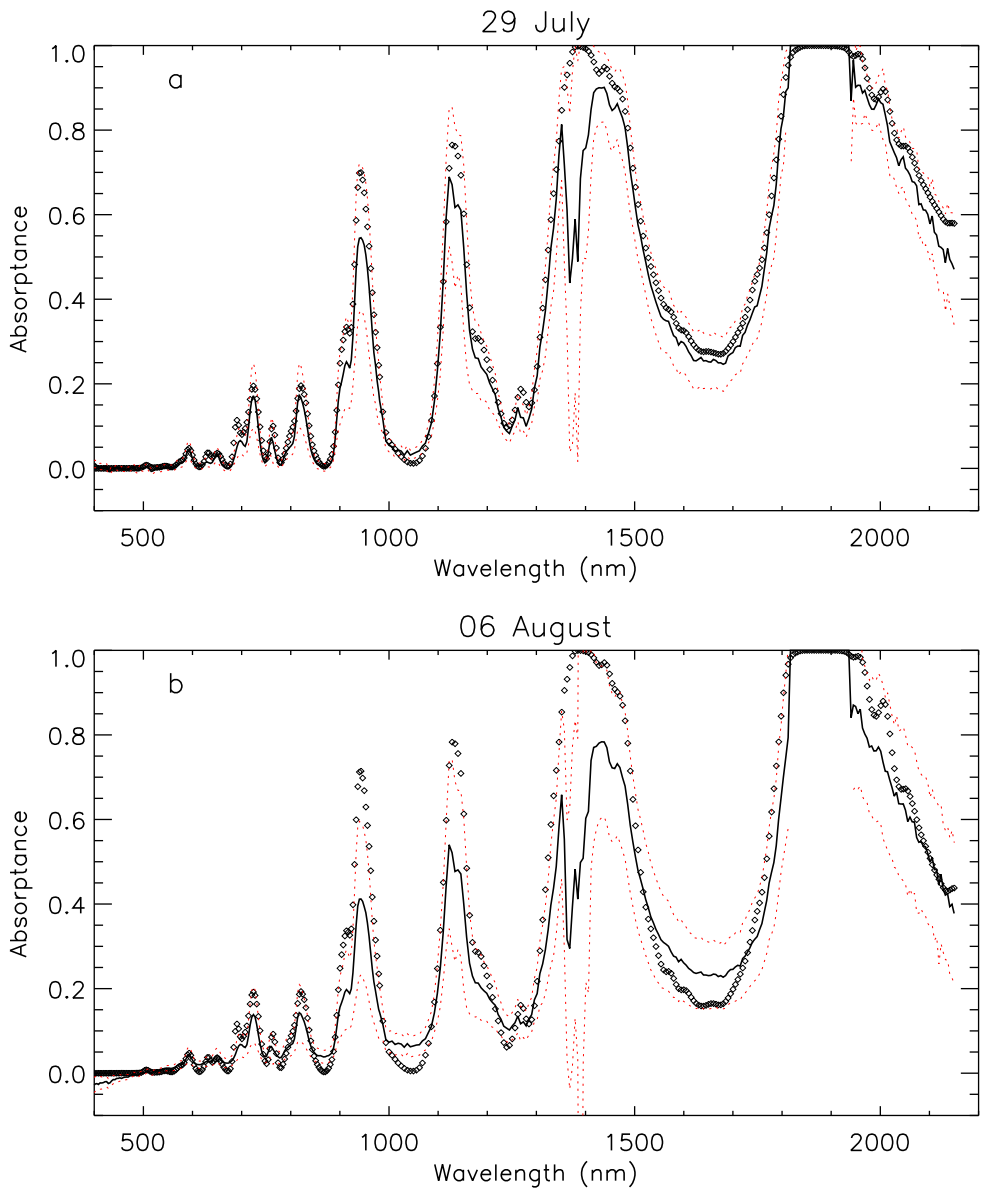

Figure 5.8: The SSFR measured absorptance spectra (solid black lines) and ± one standard deviation (dashed red lines) for the 29 July (a) and 06 August (b) are plotted. The results of the model predicted absorptance, using the optical thickness and effective radius retrieved from the albedo measurements, are plotted with diamonds.

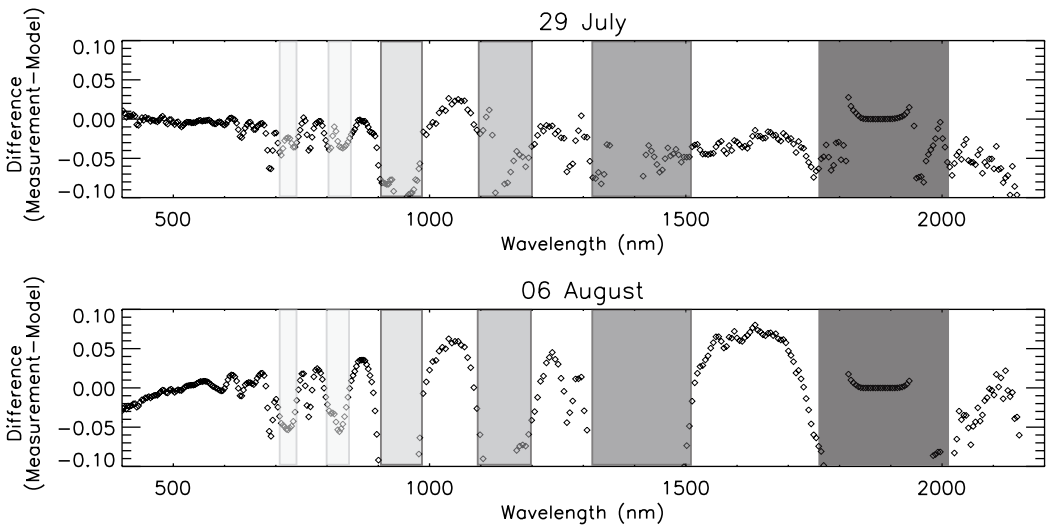

Figure 5.9: The absorptance residual spectra (measurement minus model) are plotted for the two cases. The approximate band centers and widths of water vapor are shaded. The variation in shading indicates relative band absorption strength with stronger bands shaded more darkly.

good, typically in the 0.03 range.

In the 06 August case the measurements do not agree quite as well with the model. The visible spectral band exhibits a distinct slope (increasing absorptance with increasing wavelength) with non-physical negative absorptances in the wavelength region short of 500 nm. Overall the disagreement between measurement and model was generally greater than in the 29 July case, but the differences fell within 0.07 across the entire wavelength range and were within 0.03 in the visible. As was pointed out previously, it is inherently more difficult to make a measurement of cloud absorption when the cloud is thinner and more heterogeneous. In addition to cloud horizontal heterogeneity, cloud droplet size vertical distribution may also bias the retrieval of effective radius from albedo measurements [*Platnick*, 2000]. The retrieval of cloud effective radius is weighted more heavily towards cloud top for albedo retrievals, while absorptance is a measure of the entire cloud volume.

The measured and modeled irradiance spectra were integrated across the wavelength range 400-2150 nm. The integrated measured mean absorbed irradiance for 29 July was 83.8 W m^{-2} ($\pm$33.8) out of approximately 811 W m^{-2} incident at cloud top. For 06 August, 61.5 W m^{-2} ($\pm$27.8) out of 772.0 W m^{-2} incident irradiance at the cloud top was absorbed. The integrated modeled values are: 29 July 100.4 W m^{-2} absorbed from 807 W m^{-2} incident at cloud top and 83.7 W m^{-2} absorbed and 737.6 W m^{-2} downwelling at cloud top for the 06 August case. The differences in the integrated measured and modeled values can be largely attributed to water vapor (Figure 5.8), and the modeled water vapor bands fell mostly within one standard deviation of the measured results in both cases as did the integrated values.

To demonstrate the relative effects of the various components of cloud absorption, the model for the 29 July case has been separated into: the clear sky, the enhancement of gaseous absorption from multiple scattering within the cloud, and the cloud liquid water. This was accomplished by removing the cloud layer from the model to calculate

the clear sky absorption and then computing the absorption from a cloud with the cloud droplet single-scattering albedo set to unity in all wavelengths. The enhanced gaseous absorption and cloud liquid water spectra were obtained by subtracting the three model results. Enhanced gas absorption is the difference between the non-absorbing cloud and the clear sky and the cloud liquid water is the difference between the absorbing and non-absorbing cloud. Figure 5.10(a) shows the absorbed irradiance spectrum (at model resolution) for the cloud with its integrated value of 100.4 W m^{-2}. In this plot we have left the spectra in units of irradiance to include the weighting of absorption by the solar spectrum. This is the identical spectrum to the Figure 5.8(a) model spectrum prior to normalization by the downwelling above cloud irradiance. Figure 5.10(b) contains the expected absorbed irradiance for the same atmospheric layer but without cloud. Figure 5.10(c) is the absorption by gases, enhanced by cloud scattering. Figure 5.10(d) is the absorbed irradiance due to liquid water cloud droplets. The spectrum in Figure 5.10(a) is the sum of the three remaining spectra (b-d) in Figure 5.10 as are the integrated values. The cloud liquid water absorbed irradiance (25.2 W m^{-2}) is about 1.5 times that due to the enhancement of absorption of gases due to the multiple scattering environment of the cloud layer (16.4 W m^{-2}), despite the fact that the latter occurs mostly nearer the peak of the solar spectrum. The two largest water vapor bands at 1400 and 1900 nm contribute little to the absorption here because the layer is low in the atmosphere and the bands are already near saturated at the top of the layer (1 km). Despite their relative weakness compared to other solar bands, the water vapor bands at 940 and 1140 nm are most significant because they are unsaturated and occur closer to the peak of the solar spectrum. *Davies et al.* [1984] showed similar results from a modeling study with regards to the importance of the weaker near-infrared water vapor bands for low level stratus clouds.

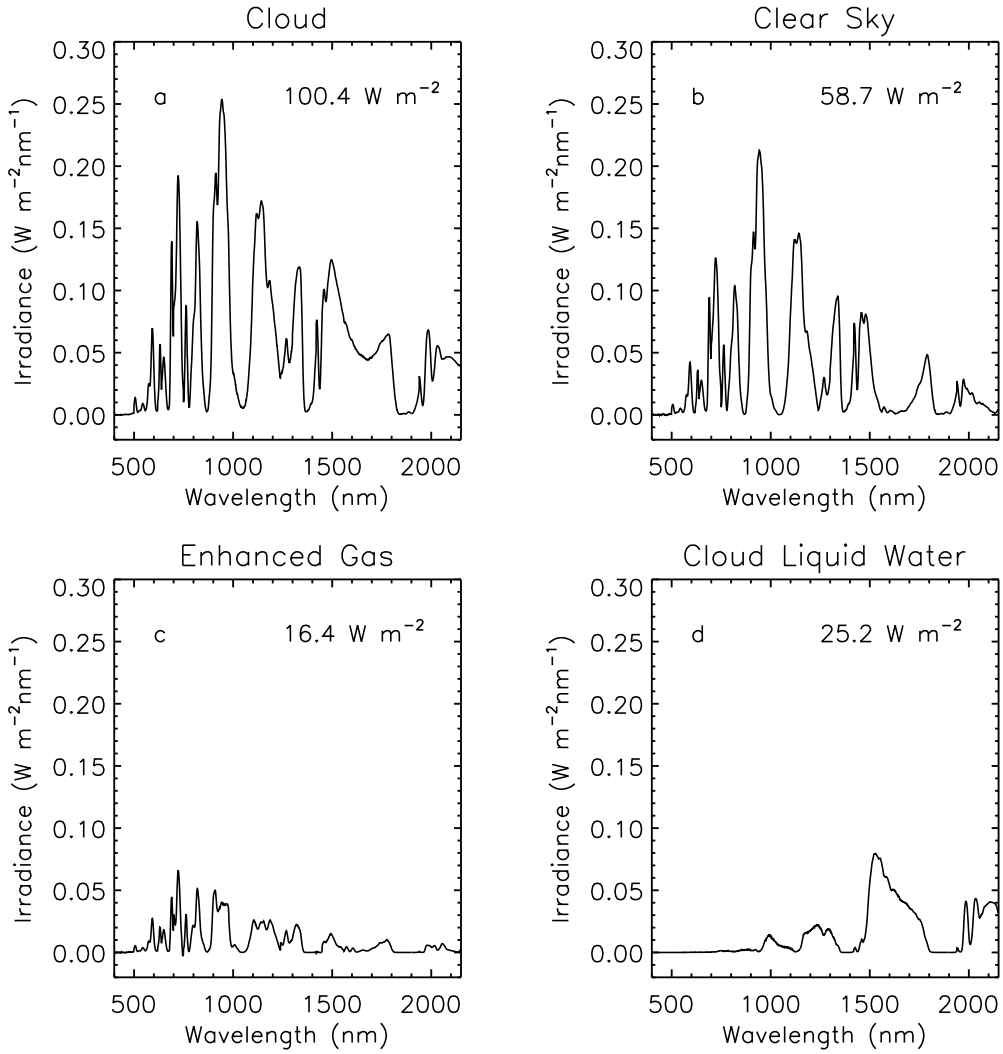

Figure 5.10: The model absorbed irradiance for the 29 July is separated into its various components. Total cloud absorbed irradiance is plotted in (a). This is the identical spectrum to Figure 5.8(a) before normalization by the above cloud downwelling irradiance. The clear sky spectrum (b) is the model absorbed irradiance for the same atmospheric layer without a cloud. The enhanced gaseous absorbed irradiance is (c) and the cloud liquid water (d). The cloud spectrum (a) is the sum of (b), (c) and (d)..

5.8 Spectral cloud absorption with absorbing aerosol

The effect of aerosol, in particular a strongly absorbing aerosol like black carbon (BC) on cloud absorption was considered beginning with the work of *Danielson et al.* [1969] and later by *Chylek et al.* [1984], *Chylek and Hallett* [1992], *Chylek et al.* [1996]. Increased absorption by clouds may shorten cloud lifetime [*Ackerman et al.*, 2000], increase water vapor, and decrease precipitation [*Jacobson*, 2001]. *Grassl* [1975] estimated radiative heating of clouds by absorbing aerosols. The absorptance measurements shown in this work were accurately modeled with Mie calculations of cloud liquid water using the refractive index of pure water. There was no evidence of aerosol absorption in these measurements. Previously, the effect on spectral absorptance of varying cloud droplet effective radius coupled with optical thickness was demonstrated (Figure 5.6(a-b)). The effect of water vapor can be seen in the large variations in the water vapor bands measured by the SSFR and the concomitant large range in the integrated values of irradiance. For completeness, here we perform some simple modeling to demonstrate what the expected spectral signature of an absorbing aerosol (BC) embedded in a liquid water cloud would be for cloud spectral flux divergence measurements made by the SSFR.

Th model used here is the same as that discussed in section 5.5. In addition to cloud layers, the model allows the incorporation of aerosol layers that can be embedded externally in a cloud layer [*Liu et al.*, 2001]. The radiative transfer model requires as input for the aerosol layer, optical thickness, asymmetry parameter, and single-scattering albedo. The aerosol extinction and absorption optical thicknesses (τ_{ext},τ_{ab_s}) and single-scattering albedo ϖ_0 are wavelength dependent. The dependence of optical thickness with wavelength is frequently modeled by the Ångström law of turbidity. Equation 5.3 gives the wavelength dependence of the aerosol optical thickness:

$$\tau_{ext}(\lambda) = \tau_{ext}(550_{nm}) \left[\frac{\lambda}{\lambda_{550nm}} \right]^{-\alpha} \tag{5.3}$$

The Ångström exponent α describes the decrease of aerosol optical thickness with wavelength. Similarly, the wavelength dependence of absorption optical thickness has been described with an Absorption Ångström Exponent (AAE) denoted with β here [*Bergstrom et al.*, 2007, *Bond*, 2001].

$$\tau_{abs}(\lambda) = \tau_{abs}(550_{nm}) \left[\frac{\lambda}{\lambda_{550nm}} \right]^{-\beta} \tag{5.4}$$

The absorption optical thickness is the product of the extinction optical thickness and the single-scattering co-albedo:

$$\tau_{abs} = \tau_{ext}(1 - \varpi_0) \tag{5.5}$$

The single-scattering albedo for BC decreases with increasing wavelength [*Bergstrom et al.*, 2007, *Dubovik et al.*, 2002]. The complex part of the index of refraction of BC is a poorly constrained value [*Bond and Bergstrom*, 2006], and the wavelength sampling is limited. To estimate the spectral dependence of the single-scattering albedo of BC, the AAE (equation 5.4), was combined with the Ångström extinction optical thickness (equation 5.3) and equation 5.5 to give the single-scattering albedo wavelength dependence:

$$\varpi_0(\lambda) = 1 - \left[\frac{\lambda}{\lambda_{550nm}} \right]^{\alpha-\beta} (1 - \varpi_{550nm}) \tag{5.6}$$

No single refractive index can describe all of the compositional complexities of elemental carbon particles in the atmosphere nor can a representative average [*Bond and Bergstrom*, 2006]. The modeling done here is simply to give a representative example of the expected magnitude and spectral signature of absorptance for a cloud with an externally mixed absorbing aerosol. The effect on the single-scattering albedo and asymmetry parameter between externally and internally mixed BC particles in cloud liquid droplets has been shown to be small [*Liu et al.*, 2001], simplifying the radiative

transfer calculations.

The retrieved values of an optical thickness (26) and effective radius (11 μm) from the 29 July case were used as the starting point for the modeling of an absorbing aerosol. The atmospheric profile of state variables, cloud height, and geometrical thickness were identical to that used previously for the 29 July case. The values of the Ångström exponent α=1.25 and β=1.0 were typical of the examples given in *Bergstrom et al.* [2007] that reported examples of AAE, derived in part from SSFR measurements, from several field experiments. The aerosol optical thickness at 550 nm was specified with the values: 0.01, 0.10, 0.20, 0.30, 0.40, and 0.50. The single scattering albedo was set to 0.93 at 550 nm, a typical value of absorbing aerosols [*Bergstrom et al.*, 2007] and the spectral dependence for all other wavelengths was specified by equation 5.6. The aerosol was placed entirely within the cloud layer.

Figure 5.11(a) shows the results over the entire wavelength range; Figure 5.11(b) is the visible to very near infrared range for the same model results. The top most spectrum in each panel of Figure 5.11 is with an aerosol optical thickness of 0.50; the bottom most spectrum is for 0.01. The absorptance increases with increasing aerosol optical thickness. The largest changes in absorptance occur in the visible wavelengths. The largest absorptance in the visible occurs at the shortest wavelengths despite decreasing single scattering albedo with wavelength. The decreasing optical thickness with wavelength has a greater effect on absorption than the change (decrease) in single-scattering albedo. At longer wavelengths in the near infrared (e.g., 1600 nm), the aerosol absorption is negligible regardless of the aerosol optical thickness; cloud absorption dominates at these wavelengths.

The slope of the visible absorptance due to aerosols makes spectrally resolved measurements especially useful. The use of an Ackerman-Cox type correction to cloud flux divergence measurements assumes that absorption at these wavelengths is zero. For a cloud with an absorbing aerosol this is not the case. Presumably, spectrally resolved

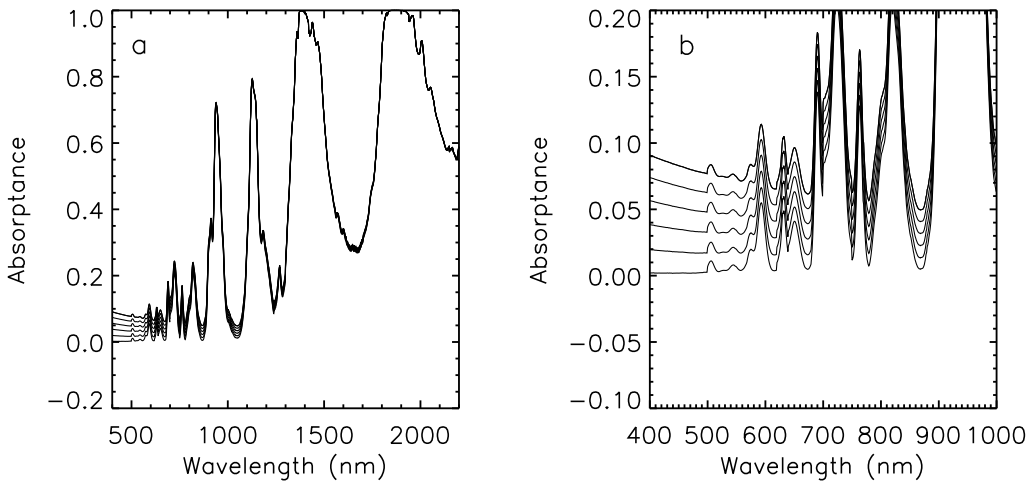

Figure 5.11: The results of the 29 July cloud case with varying amounts of an absorbing aerosol embedded in the cloud. The six spectra correspond to the six aerosol optical thicknesses used in the model; the highest absorptance is for the largest aerosol optical thickness.

measurements like those shown here could identify cases contaminated by aerosols as indicated by this slope. The utilization of a longer wavelength, less impacted by aerosol and still unaffected by cloud absorption (e.g. 850 nm) would mitigate the effects of aerosols. Note that the slope present in the 06 August case (see Figure 5.6(b)) is opposite of what is predicted from the aerosol modeling. The slope in the 06 August case is positive not negative as was predicted from modeling. Based on this result, it would be difficult to explain the slope in the absorptance spectrum from 06 August with absorption by aerosol particles.

5.9 Summary and conclusions

Deriving cloud absorption from airborne measurements of net vertical irradiance is difficult to make and the results, particularly those derived from broadband measurements, are often difficult to interpret. This has contributed to a controversy about the magnitude and nature of cloud absorption. With spectrally resolved measurements of cloud absorption the underlying mechanisms can largely be separated and the various absorption processes quantified. We have presented the results from two marine stratus cases observed during TC^4. These were chosen because they represented near-ideal conditions for the spectrally resolved measurement and modeling of cloud absorptance. The cloud layers were large in horizontal extent, relatively uniform, were cloud-free above, with a dark uniform surface (ocean) albedo below. For one of the cases, the optical thickness of the cloud was substantial and the cloud was relatively uniform, which also leads to a more robust measurement of absorptance.

Cloud flux divergence has frequently been applied to measurements from a pair of stacked aircraft. The results of this study demonstrate that measurements made by a single aircraft can lead to a more reliable estimate of cloud absorptance using a variation of conditional sampling. This does not produce a flight-time series of cloud absorption but rather a statistical estimation of cloud absorptance of the entire cloud field. With this

method errors due to calibration errors of the radiometers or spectrometers are reduced. Stacked aircraft with large vertical separation can produce spectrally dependent errors in absorptance measurements as was shown, albeit for a rather large vertical offset from the high altitude ER-2.

Mie calculations of liquid water droplets combined with a plane-parallel radiative transfer code were used first to retrieve the cloud optical thickness and effective radius from measurements of spectral albedo. The retrieved values of optical thickness and effective radius were then used as input at much higher spectral sampling to predict the spectral absorptance. The results from the 29 July case show that the spectral cloud absorptance measurements agreed with the modeled absorptance to within 0.05 over the entire spectral range (400-2150 nm) outside of water vapor absorption bands, well within the uncertainties of the measurements. The agreement is substantially better than 0.05 in much of the spectrum, and is better than 0.01 in the visible to very near infrared where absorptance is always zero regardless of the optical thickness or effective radius and thus is insensitive to the retrieval of these values from the albedo spectra. Agreement is somewhat poorer in the near-infrared, approximately 0.03. The absorption in near infrared is highly sensitive to the retrieval of optical thickness and effective radius and this may explain some of the discrepancy. The 06 August had slightly larger differences between the model and measurement spectral absorptance, up to 0.02-0.03 in the visible and 0.05-0.07 in the near-infrared, but this cloud layer was much thinner and more heterogeneous, making absorption measurements less reliable.

The integrated values of measured absorbed irradiance varied by 40-45% (one standard deviation) from the mean. The large standard deviations of SSFR absorptance spectra for both cases show that the large range in integrated absorbed irradiance is largely attributed to variation in water vapor. Model results of an absorbing aerosol embedded in a cloud layer indicate that greatest effect on absorbed irradiance occurs in the visible part of the spectrum and that the spectra contain a slope in the visible that is

diagnostic of the presence of aerosols. This slope is opposite in sign to that observed in the 06 August case and in other measurements made by the SSFR. Thus is not thought to be the result of aerosols. The cause for the slope is a topic of current investigation. It has been observed several times now with the SSFR, but for these two cases it occurred in the low optical thickness case not the high optical thickness, more uniform cloud case. This suggests that is not related to true cloud absorption.

Chapter 6

Summary and Outlook

In this thesis solar spectral irradiance measurements were used to investigate the spectral radiative properties of ice and liquid water clouds. The TC4 field experiment based in Costa Rica during July and August of 2007 provided unique opportunities to examine the spectral radiative properties of both ice and liquid water clouds from multiple aircraft equipped with Solar Spectral Flux Radiometers. Included in this thesis is the refinement of spectral irradiance measurements with the redesign of the baffle used in the airborne integrating sphere and the design, construction, and performance of a solar irradiance system for the NCAR HIAPER aircraft.

In the first chapter of this thesis the spectral irradiance component of the HAIPER Atmospheric Radiation Package is described. The radiometric precision, stability and accuracy of the spectrometers were shown to be in the 1-3% range. This was demonstrated with both laboratory and flight experiments. The largest source of error was shown to be in the cosine response of the light collector (integrating sphere). The errors for some angles reached 15-20%, a "hotspot". The redesign of the baffle in the light collector is the subject of chapter three of this thesis. A new baffle design was predicted by a Monte Carlo model to have a substantially improved cosine response. The construction and testing of this new design confirmed the results of the model. The hotspot was reduced three-fold from the original design.

In chapter 4 of this thesis, a detailed study of ice cloud spectral albedo from TC^4

is presented. Single-scattering properties of ice crystals are critical to satellite retrievals of cloud radiative properties. A satellite-like two channel retrieval of optical thickness and effective radius was used to model the complete solar spectral albedo as a method of validating the wavelength dependent ice crystal single-scattering properties. The model results were compared with the measured spectral albedo from SSFR. For the lower optical depth cases (5-15) the differences were generally within 0.05 in albedo. For an optically thicker case (46-90) the differences between the measurement and model were greater, up 0.10 in albedo. These differences were most notable in the 400-600 nm and 1200-1300 nm wavelength ranges. Larger differences were found when using MODIS airborne simulator retrievals of optical thickness and effective radius but these comparisons were hampered by differences in spatial sampling between the two instruments.

In chapter 5 the topic of cloud absorption of solar radiation is examined. This has been a contentious topic from the earliest attempts at deriving cloud absorption from aircraft. Because previous work has been limited to broadband measurements, little insight into the mechanisms of cloud absorption has been possible. With spectrally resolved measurements of irradiance, such as the ones presented in this thesis, the causes of absorption can be distinguished. Detailed radiative transfer calculations combined with Mie calculations of liquid water cloud droplets were compared with the flux divergence of a marine stratus cloud layers encountered twice during TC^4. Modeling was used to delineate the various components of absorption in a cloud layer and included the spectral signature of an absorbing aerosol embedded in the cloud layer, although no such evidence of aerosol absorption was found in the cases presented in this thesis. Large deviations in the integrated absorbed irradiance could be attributed to water vapor variations in the cloud layer. Additionally, a novel technique for using a single aircraft for the measurement of vertical flux divergence was demonstrated.

Further work includes the further improvement in the cosine response of the integrating sphere used for solar spectral irradiance measurements. Additionally, new

single-scattering ice crystal properties are currently under development with complete wavelength coverage, updated values of ice optical constants, and varying surface morphologies. These can be tested in the identical way presented here. Questions also remain about the spectral albedo of ice clouds in the visible wavelengths and the possible effects of a spherical atmosphere not included in the plane-parallel calculations performed in this thesis. Lastly, the spectral dependence of apparent absorption likely due to cloud 3-D effects, seen in one of the cases presented in chapter five, has also been observed for ice cloud flux divergence and its cause has not been fully explained.

Bibliography

Abbot, C. G., and F. E. Fowle, Income and outgo of heat from the Earth, and the dependence of its temperature thereon., *Ann. Astrophys. Observ.*, *2*, 159–176, 1908.

Ackerman, S. A., and S. K. Cox, Aircraft observations of shortwave fractional absorptance of non-homogeneous clouds, *J. Appl. Meteorol.*, *20*, 1510–1515, 1981.

Ackerman, T. P., O. B. Toon, D. E. Stevens, A. J. Heymsfield, V. Ramanathan, and E. J. Welton, Reduction of tropical cloudiness by soot, *Science*, *288*, 1042–1047, 2000.

Ackerman, T. P., D. M. Flynn, and R. T. Marchand, Quantifying the magnitude of anamalous solar absorption, *J. Geophys. Res.*, *109(D9)*, 4273–, 2003.

Arking, A., Absorption of solar energy in the atmosphere: Discrepancy between model and observations, *Science*, *273*, 779–782, 1996.

Arking, A., The influence of clouds and water vapor on atmospheric absorption, *Geophys. Res. Lett.*, *26*, 2729–2732, 1999.

Baran, A., A review of the light scattering properties of cirrus, *J. Quant. Spect. Rad. Tran.*, *110*, 1239–1260, 2009.

Baran, A., J. S. Havemann, P. N. Francis, and P. D. Watts, A consistent set of single-scattering properties for cirrus cloud: Tests using radiance measurements from a dual-viewing multi-wavelength satellite-based instrument, *J. Quant. Spectrosc. Radiat. Transfer*, *79*, 549–567, 2003.

Baran, A. J., and P. N. Francis, On the radiative properties of cirrus cloud at solar and thermal wavelengths: A test of model consistency using high-resolution airborne radiance measurements, *Q. J. R. Meteorol. Soc*, *130*, 763–778, 2004.

Baran, A. J., and L.-C. Labonnote, A self consistent scattering model for cirrus. I: the solar region, *Q. J. R. Meteorol. Soc.*, *133*, 1899–1912, 2007.

Baum, B. A., D. P. Kratz, P. Yang, S. C. Out, Y. Hu, P. F. Soulen, and S. C. Tsay, Remote sensing of cloud properties using MODIS airborne simulator imagery during SUCCESS, data and models, *J. Geophys. Res.*, *105*, 11,781–11,792, 2000.

Baum, B. A., P. Yang, A. J. Heymsfield, S. Platnick, M. D. King, Y.-X. Hu, and S. T. Bedka., Bulk scattering properties for the remote sensing of ice clouds: Part II: Narrowband models, *J. Appl. Meteorol.*, *44*, 1896–1911, 2005.

Bergstrom, R. W., P. Pilewskie, B. Schmid, and P. B. Russell, Estimates of the spectral aerosol single scattering albedo and aerosol radiative effects during SAFARI 2000, *J. Geophys. Res.*, *108*(D13), doi:10.1029/2002JD002435, 2003.

Bergstrom, R. W., P. Pilewskie, P. B. Russell, J. Redemann, T. C. Bond, P. K. Quinn, and B. Sierau, Spectral absorption properties of atmospheric aerosols, *Atmos. Chem. Phys.*, *7*, 5937–5943, 2007.

Bierwirth, E., Airborne measurements of the spectral surface albedo over Morocco and its influence on the radiative forcing of Saharan dust, Ph.D. thesis, Johannes Gutenberg-University, 2008.

Biggar, S. F., P. Slater, and D. Gellman, Uncertainties in the in-flight calibration of sensors with reference to measured ground sites in the 0.4 to 1.1 μm range, *Remote Sens. Environ*, *48*, 245–252, 1994.

Bodhaine, B. A., N. B. Wood, E. G. Dutton, and J. R. Slusser, On Rayleigh optical depth calculations, *J. Atmos. and Ocean. Tech.*, *16*, 1854–1861, 1999.

Bohren, C. F., and D. R. Huffman, *Absorption and Scattering of Light by Small Particles*, Wiley-Interscience, 1983.

Bond, T., Spectral dependence of visible light absorption by carbonaceous particles emitted from coal combustion, *Geophys. Res. Lett.*, *28*, 4075–4078, 2001.

Bond, T. C., and R. W. Bergstrom, Light absorption by carbonaceous particles: An investigative review, *Aerosol Sci. and Technol.*, *40*, 27–67, 2006.

Bony, S., R. Colman, V. M. Kattsov, R. P. Allan, C. S. Bretherton, J. L. Dufresne, A. Hall, S. Hallegatte, M. M. Holland, W. Ingram, D. A. Randall, B. J. Soden, G. Tselioudis, and M. J. Webb, How well do we understand and evaluate climate change feedback processes?, *J. of Climate*, *19(15)*, 3445–3482, 2006.

Born, M., and E. Wolf, *Principles of Optics*, Cambridge University Press, 1999.

Budde, W., Integrating sphere for the photometry of the sky, *Appl. Opt.*, *3*, 939–941, 1964.

Cess, R. D., M. H. Zhang, P. Minnis, L. Corsetti, E. G. Dutton, B. W. Forgan, D. P. Garber, W. L. Gates, J. J. Hack, E. F. Harrison, X. Jing, J. T. Kiehl, C. N. Long, J. J. Morcrette, G. L. Potter, V. Ramanathan, B. Subasilar, C. H. Whittlock, D. F. Yound, and Y. Zhou, Absorption of solar radiation by clouds: Observations versus models, *Science*, *267*, 496–499, 1995.

Chen, T., W. B. Rossow, and Y. C. Zhang, Radiative effects of cloud-type variations, *J. Climate*, *13*, 264–286, 2000.

Chiu, J.-Y., A. Marshak, and W. J. Wiscombe, The effect of surface heterogeneity on cloud absorption estimates, *Geophys. Res. Lett.*, *31*, 2004.

Chylek, P., and J. Hallett, Enhanced absorption of solar radiation by cloud droplets containing soot particles in their surface, *Q. J. R. Meteorol. Soc.*, *118*, 167–172, 1992.

Chylek, P., V. Ramaswamy, and R. J. Cheng, Effect of graphitic carbon on the albedo of clouds, *J. Atmos. Sci.*, *41*, 3076–3084, 1984.

Chylek, P., G. B. Lesins, G. Videen, J. G. D. Wong, R. G. Pinnick, D. Ngo, and J. D. Klett, Black carbon and absorption of solar radiation by clouds, *J. Geophys. Res.*, *101*, 23,365–23,371, 1996.

Coddington, O. M., K. S. Schmidt, P. Pilewskie, W. J. Gore, R. W. Bergstrom, M. Román, J. Redemann, P. B. Russell, J. Liu, and C. C. Schaaf, Aircraft measurements of spectral surface albedo and its consistency with ground-based and spaceborne observations, *J. Geophys. Res.*, *113*(D17209), doi:10.1029/2008JD010089, 2008.

Coddington, O. M., P. Pilewskie, J. Redemann, S. P. P. B. Russell, K. S. Schmidt, W. J. Gore, J. Livingston, G. Wind, and T. Vukicevic, Examining the impact of overlying aerosols on the retrieval of cloud optical properties from passive remote sensing, *J. Geophys. Res.*, *115*, 2010.

Cooper, S. J., T. S. L'Ecuyer, P. Gabriel, A. J. Baran, and G. L. Stephens, Objective assessment of the information content of visible and infrared radiance measurements for cloud microphysical property retrievals over the global oceans. Part II: Ice clouds, *J. App. Meteorol. and Climatology.*, *45*, 42–62, 2006.

Crowther, B. G., Computer modeling of integrating spheres, *Appl. Opt.*, *35*, 5880–5886, 1996.

Crowther, B. G., The design, construction, and calibration of a spectral diffuse/global irradiance meter, Ph.D. thesis, University of Arizona, 1997.

Crowther, B. G., K. J. Thome, S. F. Biggar, and C. J. Burkhart, Internally-baffled integrating sphere cosine collector, *Proc. SPIE*, *3117*, 246–252, 1997.

Danielson, R. E., D. R. Moore, and H. C. van de Hulst, The transfer of visible radiation through clouds, *J. Atmos. Sci.*, *26*, 1078–1087, 1969.

Davies, R. W., W. L. Ridgway, and K.-E. Kim, Spectral absorption of solar radiation in cloudy atmospheres: A 20 cm-1 model, *J. Atmos. Sci.*, *41*, 2126–2137, 1984.

de la Casiniere, A., T. Cabot, and S. Benmansour, Measuring spectral diffuse solar irradiance with non-cosine flat-plate diffusers, *Solar Energy*, *54*, 173–182, 1995.

Downing, H. D., and D. Williams, Optical constants of water in the infrared, *J. Geophys. Res.*, *80(12)*, 1656–1661, 1975.

Dubovik, O., B. N. Holben, T. F. Eck, A. Smirnov, Y. Kaufman, M. D. King, D. Tanre, and I. Slutsker, Climatology of atmospheric aerosol absorption and optical properties in key locations, *J. Atmos. Sci.*, *59*, 590–608, 2002.

Ebert, E. E., and J. A. Curry, A parameterization of ice cloud optical properties for climate models, *J. Geophys. Res.*, *97*, 3831–3836, 1992.

Edwards, J. M., S. Havemann, J. Thelen, and A. J. Baran, Parameterization for the radiative properties of ice crystals: Comparison with existing schemes and impact in a GCM., *Atmos. Res.*, *83*, 19–35, 2007.

Ehrlich, A., M. Wendisch, E. Bierwirth, J.-F. Gayer, G. Minoche, A. Lampert, and B. Mayer, Evidence of ice crystals at cloud top of Arctic boundary-layer mixed-phase clouds derived from airborne remote sensing, *Atoms. Chem. Phys*, *9*, 9401–9416., 2009.

Evans, F. K., The spherical harmonic discrete ordinate method for three-dimensional atmospheric radiative transfer, *J. Atmos. Sci.*, *55*, 429–446, 1998.

Francis, P. N., J. P. Taylor, P. Hignett, and A. Slingo, On the question of enhanced absorption of solar radiation by clouds, *Q. J. R. Meteorol. Soc.*, *123*, 419–434, 1997.

Franke, H., and D. Schell, *Documentation for HARP stabilized platforms on HIAPER*, enviscope GmbH, D-60489 Frankfurt, Germany, 2007.

Fritz, S., and T. H. MacDonald, Measurements of absorption of solar radiation by clouds, *Bull. Amer. Meteorol. Soc.*, *32*, 205–209, 1951.

Fu, Q., A new parameterization of an asymmetry factor of cirrus clouds for climate models, *J. Atmos. Sci.*, *64*, 4140–4150, 2007.

Goebel, D. G., Generalized integrating-sphere theory, *Appl. Opt.*, *6*, 125–128, 1967.

Grassl, H., Albedo reduction and radiative heating of clouds by absorbing aerosol particles, *Contrib. to Atmos. Phys.*, *48*, 199–210, 1975.

Hale, G. M., and M. R. Querry, Optical constants of water in the 200 nm to 200 mm wavlength region, *Applied Optics*, *3*, 555–563, 1973.

Hansen, J. E., and L. D. Travis, Light scattering in planetary atmospheres., *Space Sci. Rev.*, *16*, 1974.

Harrison, L., J. Michalsky, and J. Berndt, Automated multifilter rotation shadow-band radiometer: An instrument for optical depth and radiation measurements, *Appl. Opt*, *33*, 5118–5125, 1994.

Hartmann, D. L., M. E. Ockert-Bell, and M. L. Michelsen, The effect of cloud type on Earth's energy balance: Global analysis, *J. Geophys. Res.*, *5*, 1281–1304, 1992.

Havemann, S., and A. J. Baran, Calculation of the phase matrix elements of elongated hexagonal ice columns using the T-matrix method, *J. Quant. Spectrosc. Radiat. Transfer*, *89*, 87–96, 2004.

Hayasaka, T., N. Kikuchi, and M. Tanaka, Absorption of solar radiation by stratocumulus clouds: Aircraft measurements and theoretical calculations, *J. App. Meteorol.*, *34*, 1047–1055, 1995.

Hong, G., P. Yang, B. A. Baum, A. J. Heymsfield, and K.-M. Xu, Parameterization of shortwave and longwave radiative properties of ice clouds for use in climate models, *J. of Climate*, *22*, 6287–6312, 2009.

Hook, S. J., K. J. Thome, M. Fitzgerald, and A. B. Kahle, The MODIS/ASTER airborne simulator (MASTER) - a new instrument for earth science studies., *Rem. Sens. Envrn.*, *76*, 93–102, 2001.

Hu, X.-Y., B. Wielicki, B. Lin, G. Gibson, S.-C.Tsay, K. Stamnes, and T. Wong, A fast and accurate treatment of particle scattering phase functions with weighted singular-value decomposition least-squares fitting, *J. Quant. Spectrosc. Radiat. Transfer.*, *65*, 681–690, 2000.

Jackson, R. D., T. R. Clarke, and M. S. Moran, Bidirectional calibration results for 11 Spectralon and 16 $BaSO_4$ reference reflectance panels,, *Remote Sens. Environ.*, *40*, 231–239, 1992.

Jacobson, M. Z., Strong radiative heating due to the mixing state of black carbon in atmospheric aerosols, *Nature*, *409*, 695–697, 2001.

Jensen, E. J., and O. B. Toon, Tropical cirrus cloud radiative forcing: Sensitivity studies, *Geophys. Res. Lett.*, *21*, 2023–2026, 1994.

Jensen, E. J., D. Starr, and O. B. Toon, Mission investigates tropical cirrus clouds, *Eos Trans. AGU*, *85*, 45–49, 2004.

Jiang, J. H., H. Su, S. T. Massie, P. Calarco, M. Schoeberl, and S. Platnick, Aerosol-CO relationship and aerosol effect on ice cloud particle size: Analyses from Aura MLS and Aqua MODIS observations., *J. Geophys. Res.*, *114*, 2009.

Jin, Z., T. P. Charlock, W. L. Smith, and K. Rutledge, A parameterization of ocean surface albedo, *Geophys. Res. Lett.*, *31*, 2004.

Joseph, J. H., W. J. Wiscombe, and J. A. Weinman, The delta-Eddington approximation for radiative flux transfer, *J. Atmos. Sci.*, *33*, 2452–2459, 1976.

Kiehl, J. T., J. J. Hack, M. H. Zhang, and R. D. Cess, Sensitivity of a GCM climate to enhanced shortwave cloud absorption, *J. Climate*, *8*, 2200–2212, 1995.

Kindel, B. C., K. S. Schmidt, P. Pilewskie, B. Baum, P. Yang, and S. Platnick, Observations and modeling of ice cloud shortwave spectral albedo during the Tropical Composition, Cloud and Climate Coupling Experiment, *J. Geophys. Res.*, *115*, 2010.

King, M. D., L. F. Radke, and P. V. Hobbs, Determination of the spectral absorption of solar radiation by marine stratocumulus clouds from airborne measurements within clouds, *J. Atmos. Sci.*, *47*, 894–907, 1990.

King, M. D., Y. J. Kaufman, W. P. Menzel, and D. Tanre, Remote sensing of cloud, aerosol, and water vapor properties from the moderate resolution imaging spectrometer (MODIS), *IEEE Trans. Geosci. Remote Sens.*, *30*, 1992.

King, M. D., S. Platnick, P. Yang, G. T. Arnold, M. A. Gray, J. C. Riedi, S. A. Ackerman, and K. N. Liou, Remote sensing of liquid water and ice cloud optical thickness and effective radius in the Arctic: Application of airborne multispectral MAS data, *J. Atmos. Oceanic Technol.*, *21*, 857–875, 2004.

King, M. D., S. Platnick, G. Wind, T. Arnold, and R. T. Dominguez, Remote sensing of the radiative and microphysical properties of clouds during TC^4: results from MAS, MASTER, MODIS, and MISR, *J. Geophys. Res.*, *115*, 2010.

Kurucz, R. L., Synthetic infrared spectra, in *Infrared Solar Physics*, edited by D. M. Rabin and J. T. Jeffries, 154, IAU Symposium, Kluwer Acad., Norwell, Mass, 1992.

Lacis, A. A., and V. Oinas, A description of the correlated-k distribution method for modeling nongray gaseous absorption, thermal emission, and multiple scattering in vertically inhomogeneous atmospheres, *J. Geophys. Res.*, *96*, 9027–9063, 1991.

Laursen, K. K., D. P. Jorgensen, G. P. Brasseur, S. L. Ustin, and J. R. Hunning, The next generation NSF/NCAR reasearch aircraft, *Bull. Amer. Meteorol. Soc.*, *87*, 896–909, 2006.

Li, Z., and H. G. Leighton, Global climatology of the solar radiation budgets at the surface and in the atmosphere from 5 years of ERBE data, *J. Geophys. Res.*, *98*, 4919–4930, 1993.

Li, Z., Q. L. Moreau, and A. Arking, On solar energy disposition: A perspective from observation and modeling, *Bull. Amer. Meteorol. Soc.*, *78*, 53–70, 1997.

Liu, L., M. I. Mishchenko, S. Menon, A. Macke, and A. A. Lacis, The effect of black carbon on scattering and absorption of solar radiation by cloud droplets, *J. Quant. Spect. Rad. Tran.*, *74*, 195–204, 2001.

Loeb, N. G., S. Kato, and B. A. Wielicki, Defining top-of-the-atmosphere flux reference level for Earth radiation budget studies, *J. of Climate*, *15*, 3301–3309, 2002.

Lynch, D. K., *Cirrus*, Oxford, 2002.

Macke, A., J. Muller, and E. Raschke, Single scattering properties of atmospheric crystals, *J. Atmos. Sci.*, *53*, 2813–2825, 1996.

Marshak, A., A. Davis, W. J. Wiscombe, W. Ridgway, and R. Cahalan, Biases in shortwave column absorption in the presence of fractal clouds, *J. Climate*, *11*, 431–446, 1998.

Marshak, A., W. J. Wiscombe, A. Davis, L. Oreopoulos, and R. Cahalan, On the removal of the effect of horizontal fluxes in two-aircraft measurements of cloud absorption, *Q. J. R. Meteorol. Soc.*, *125*, 2153–2170, 1999.

McFarquhar, G. M., J. Um, M. Freer, D. Baumgardner, G. Kok, and G. Mace, Importance of small ice crystals to cirrus properties: Observations from the Tropical Warm Pool International Cloud Experiment (TWP-ICE), *Geophys. Res. Lett.*, *34*, 2007.

Michalsky, J., Q. Min, J. Barnard, R. Marchand, and P. Pilewskie, Simultaneous spectral albedo measurements near the Atmospheric Radiation Measurement Southern Great Plains (ARM SGP) central facility, *J. Geophys. Res.*, *108*(D8), 2003.

Mie, G., Beiträge zur optik trüber medien, speziell kolloidaler metallösungen, *Ann. Physik*, *25*, 377–445, 1908.

Mishchenko, M., W. Rossow, A. Macke, and A. Lacis, Sensitivity of cirrus cloud albedo, bidirectional reflectance and optical thickness retrieval accuracy to ice particle shape, *J. Geophys. Res.*, *101*, 16,973–16,985, 1996.

Mitchell, D. L., Effective diameter in radiation transfer: General definition, applications, and limitations, *J. Atmos. Sci.*, *59*, 2330–2346, 2002.

Murrow, J. H., M. S. Duhig, and C. R. Booth, Design and evaluation of a cosine collector for a SeaWiFS-compatible marine reflectance radiometer., *Proc. SPIE*, *2258*, 879–886, 1994.

Nakajima, T., and M. D. King, Determination of the optical thickness and effective particle radius of clouds from reflected solar radiation measurements I: Theory, *J. Atmos. Sci.*, *47*, 1878–1893, 1990.

Newiger, M., and K. Baehnke, Influence of cloud composition and cloud geometry on the absorption of solar radiation, *Contrib. to Atmos. Phys.*, *54*, 370–382, 1981.

O'Hirok, W., and C. Gautier, Absorption of shortwave radiation in the cloudy atmosphere: Observed and theoretical estimates during the second Atmospheric Radiation Measurement Enhanced Shortwave Experiment (ARESE), *J. Geophys. Res.*, *108*, 2003.

O'Hirok, W., C. Gautier, and P. Ricchiazzi, Spectral signature of column solar radiation absorption during the Atmospheric Radiation Measurement Enhanced Shortwave Experiment (ARESE), *J. Geophys. Res.*, *105*, 17,471–17,480, 2000.

Oreopoulos, L., A. Marshak, and R. F. Cahalan, Consistency of ARESE II cloud absorption estimates and sampling issues, *J. Geophys. Res.*, *108*, 2003.

Palmer, K. F., and D. Williams, Optical properties of water in the near infrared, *J. Opt. Soc. Am.*, *64*, 1107–1110, 1974.

Pilewskie, P., and F. P. J. Valero, Response to 'how much solar radiation do clouds absorb?' by G. L. Stephens, *Science*, *271*, 1134–1134, 1995.

Pilewskie, P., A. F. H. Goetz, D. A. Beal, R. W. Bergstrom, and P. Mariani, Observations of the spectral distribution of solar irradiance at the ground during SUCCESS., *Geophys. Res. Lett.*, *25(8)*, 1141–1144, 1998.

Pilewskie, P., J. Pommier, R. Bergstrom, W. Gore, S. Howard, M. Rabbette, B. Schmid, P. V. Hobbs, and S. C. Tsay, Solar spectral radiative forcing during the Southern African Regional Science Initiative, *J. Geophys. Res.*, *108*(D13), 8486, doi:10.1029/2002JD002411, 2003.

Pincus, R., M. Szczodrak, J. Gu, and P. Austin, Uncertainty in cloud optical depth made from satellite radiance measurements, *J. Climate*, *8*, 1453–1462., 1995.

Platnick, S., Vertical photon transport in cloud remote sensing problems, *J. Geophys. Res.*, *105*, 22,919–22,935, 2000.

Platnick, S., Approximations for horizontal photon transport in cloud remote sensing problems, *J. Quant. Spectrosc. Radiat. Transfer*, *68*, 75–99, 2001.

Platnick, S. E., M. D. King, S. A. Ackerman, W. P. Menzel, B. A. Baum, J. C. Riedi, and R. A. Frey, The MODIS cloud products: Algorithms and examples from Terra, *IEEE Transactions on Geoscience and Remote Sensing*, *41*(2), 459–473, doi:10.1109/TGRS.2002.808301, 2003.

Rabbette, M., and P. Pilewskie, Principal component analysis of Arctic solar irradiance spectra., *J. Geophys. Res.*, *107(C10)*, 2002.

Ramanathan, V., and A. M. Vogelmann, Greenhouse effect, atmospheric solar absorption and Earth's radiation: From the Arrenhius-Langley era to the 1990s, *Ambio*, *26*, 38–46, 1997.

Ramanathan, V., R. D. Cess, E. F. Harrison, P. Minnis, B. R. Barkstrom, E. Ahmad, and D. Hartmann, Cloud-radiative forcing and climate-Results from the Earth Radiation Budget Experiment, *Science*, *243*, 57–63, 1989.

Ramanathan, V., B. Subasilar, G. J. Zhang, W. Conant, R. D. Cess, J. T. Kiehl, H. Grassl, and L. Shi, Warm pool heat budget and shortwave cloud forcing: A missing physics?, *Science*, *267*, 499–503, 1995.

Rawlins, F., Aircraft measurements of the solar absorption by broken cloud fields: A case study, *Q. J. R. Meteorol. Soc.*, *115*, 365–382, 1989.

Rothman, L. S., The HITRAN 2004 molecular spectroscopic database, *J. Quant. Spect. Rad. Tran.*, *96*, 139–204, 2005.

Schiffer, R. A., and W. B. Rossow, The International Satellite Cloud Climatology Project (ISCCP). The first project of the World Climate Research Programme., *Bull. Amer. Meteorol. Soc.*, *64*, 779–784, 1983.

Schmidt, K. S., P. Pilewskie, S. Platnick, G. Wind, P. Yang, and M. Wendisch, Comparing irradiance fields derived from Moderate Resolution Imaging Spectroradiometer airborne simulator cirrus cloud retrievals with solar spectral flux radiometer measurements, *J. Geophys. Res.*, *112*, 2007.

Schmidt, K. S., G. Feingold, P. Pilewskie, H. Jiang, O. Coddington, and M. Wendisch, Irradiance in polluted cumulus fields: Measured and modeled cloud-aerosol effects, *Geophys. Res. Lett.*, *36*(L07701), doi:10.1029/2008CL036848, 2009.

Schmidt, K. S., P. Pilewskie, B. Meyer, M. Wendisch, B. C. Kindel, S. Platnick, M. D. King, G. Wind, G. T. Arnold, L. Tian, G. Heymsfield, and H. Eichler, Apparent and real absorption of solar spectral irradiance in heterogeneous ice clouds, *J. Geophys. Res.*, *115*, 2010.

Slater, P., S. F. Biggar, K. J. Thome, D. Gelman, and P. R. Spyak, Vicarious radiometric calibrations of EOS sensors, *J. Atmos. Oceanic Technol.*, *13*, 349–359, 1996.

Soden, B. J., and I. M. Held, An assessment of climate feedbacks in coupled ocean-atmosphere models, *J. of Climate*, *19(14)*, 3354–3360, 2006.

Stamnes, K., S.-C. Tsay, W. Wiscombe, and K. Jayaweera, Numerically stable algorithm for discrete-ordinate-method radiative transfer in multiple scattering and emitting layered media, *Applied Optics*, *27*(12), 2502–2509, 1988.

Stephens, G. L., How much solar radiation do clouds absorb?, *Science*, *271*, 1131–1133, 1996.

Stephens, G. L., Cloud feedbacks in the climate system, *J. Climate*, *18(2)*, 237–273, 2005.

Stephens, G. L. ., and S.-C. Tsay, On the cloud absorption anomaly, *Q. J. R. Meteorol. Soc.*, *116*, 671–704, 1990.

Stephens, G. L., S.-C. Tsay, P. W. S. Jr., and P. J. Flatau, The relevance of the microphysical and radiative properties of cirrus clouds to climate and climatic feedback, *J. Atmos. Sci.*, *47*, 1742–1735, 1990.

Stith, J. L., V. Ramanathan, W. A. Cooper, G. C. Roberts, P. J. DeMott, G. Carmichael, C. D. Hatch, B. Adhikary, C. H. Twohy, D. C. Rogers, D. Baumgardner, A. J. Prenni, T. Campos, R. Gao, J. Anderson, and Y. Feng, An overview of aircraft observations from the Pacific Dust Experiment campaign, *J. Geophys. Res.*, *114(D5)*, 2009.

Takano, Y., and K. N. Liou, Solar radiative transfer in cirrus clouds part I: Single-scattering and optical properties of hexagonal ice crystals, *J. Atmos. Sci.*, *46*, 3–19, 1989.

Taylor, J. P., J. M. Edwards, M. D. Glew, P. Hignett, and A. Slingo, Studies with a flexible new radiation code II: Comparison with aircraft shortwave observations, *Q. J. R. Meteorol. Soc.*, *122*, 839–861, 1996.

Thome, K. J., B. G. Crowther, and S. F. Biggar, Reflectance and irradiance-based calibration of Landsat-5 Thematic Mapper, *Canadian J. of Rem. Sens.*, *23*, 309–317, 1997.

Titov, G. A., Radiative horizontal transport and absorption in stratocumulus clouds, *J. Atmos. Res.*, *55*, 2549–2560, 1998.

Toon, O. B., D. O. Starr, E. J. Jensen, P. A. Newman, S. Platnick, M. R. Schoeberl, P. O. Wennberg, S. C. Wofsy, M. J. Kurylo, H. Maring, K. W. Jucks, M. S. Craig, M. F. Vasques, L. Pfister, K. H. Rosenlof, H. B. Selkirk, P. R. Colarco, S. R. Kawa, G. G. Mace, P. Minnis, and K. E. Pickering, Planning, implementation, and first results of the Tropical Composition, Cloud and Climate Coupling Experiment (TC^4), *J. Geophys. Res.*, *115*, 2010.

Trenberth, K. E., J. T. Fasullo, and J. Kiehl, Earth's global energy budget, *Bull. Amer. Meteorol. Soc.*, *90(3)*, 311–323, 2009.

Twomey, S., and T. Cocks., Spectral reflectance of clouds in the near-infrared: Comparison of measurements and calculations, *J. Meteorol. Soc. Jpn.*, *60*, 583–592, 1982.

Twomey, S., and T. Cocks, Remote sensing of cloud parameters from spectral reflectance in the near-infrared, *Beitr. Phys. Atmos.*, *62*, 172–179, 1989.

Ulanowski, Z., E. Hesse, P. H. Kaye, and A. J. Baran, Light scattering by complex ice-analogue crystals, *J. Quant. Spectrosc. Radiat. Transfer*, *100*, 382–392, 2006.

Valero, F. P. J., R. D. Cess, M. Zhang, S. K. Pope, A. Bucholtz, B. Bush, and J. V. Jr., Absorption of solar radiation by the cloudy atmosphere: Interpretations of collocated aircraft instruments, *J. Geophy*, *103*, 29,917–29,927, 1997.

Valero, F. P. J., P. Minnis, S. K. Pope, A. Bucholtz, B. C. Bush, D. R. Doelling, W. L. S. Jr., and X. Dong, Absorption of solar radiation by the atmosphere as determined using satellite, aircraft, and surface data during the Atmospheric Radiation Measurements Enhanced Shortwave Experiment (ARESE), *J. Geophys. Res.*, *105*, 4743–4758, 2000.

Waliser, D. E., J.-L. Li, C. Woods, R. Austin, J. Bacmeister, J. Chern, A. D. Genio, J. Jiang, Z. Kuang, H. Meng, P. Minnis, S. Platnick, W. Rossow, G. Stephens, S. Sun-Mack, W. Tao, A. Tompkins, D. Vane, C. Walker, and D. Wu, Cloud ice: A climate model challenge with signs and expectations of progress, *J. Geophys. Res.*, *114*, 2009.

Walker, J. H., R. D. Saunders, J. K. Jackson, and D. A. McSparron, NBS Measurement Services: Spectral Irradiance Calibrations, *Tech. rep.*, U.S. Department of Commerce, 1987.

Warren, S. G., Optical constants of ice from the ultraviolet to the microwave, *Appl. Opt.*, *23*, 1206–1225, 1984.

Warren, S. G., and R. E. Brandt, Optical constants of ice from the ultraviolet to the microwave: A revised compilation., *J. Geophys. Res.*, *113*, 2008.

Wendisch, M., and A. Kiel, Discrepancies between measured and modeled solar and UV radiation within polluted boundary layer clouds, *J. Geophys. Res.*, *104*, 27,373–27,385, 1999.

Wendisch, M., D. S. D. Müller, and J. Heintzenberg, An airborne spectral albedometer with active horizontal stabilization., *J. Atmos. Oceanic Technol.*, *18*, 1856–1866, 2001.

Wendisch, M., P. Pilewskie, J. Pommier, S. Howard, P. Yang, A. J. Heymsfield, C. G. Schmitt, D. Baumgardner, and B. Mayer, Impact of cirrus crystal shape on solar spectral irradiance: A case study for subtropical cirrus, *J. Geophys. Res.*, *110*, 2005.

Wielicki, B. A., R. D. Cess, M. D. King, D. A. Randall, and E. F. Harrison, Mission to planet Earth: Role of clouds and radiation in climate, *Bull. Amer. Meteorol. Soc.*, *76(11)*, 2125–2153, 1995.

Wild, M., Short-wave and long-wave surface radiation budgets in GCMs: A review based on the IPCC-AR4/CMIP3 models, *Tellus*, *60A*, 932–945, 2008.

Wild, M., C. N. Long, and A. Ohmura, Evaluation of clear-sky solar fluxes in GCMs participating in AMIP and IPCC-AR4 from a surface perspective, *J. Geophys. Res.*, *111(D01104)*, 2006.

Wiscombe, W. J., The delta-M method: rapid yet accurate radiative flux calculation for strongly asymmetric phase functions, *J. Atmos. Sci.*, *34*, 1408–1422, 1977.

Wiscombe, W. J., R. M. Welch, and W. D. Hall, The effects of very large drops on cloud absorption, Part I: parcel models, *J. Atmos. Sci.*, *41*, 1336–1355, 1984.

Yang, P., and K. N. Liou, Single-scattering properties of complex ice crystals in terrestrial atmosphere, *Contrib. to Atmos. Phys.*, *71*, 223–248, 1998.

Yang, P., K. Liou, and W. Arnott, Extinction efficiency and single-scattering albedo for laboratory and natural cirrus clouds, *J. Geophys. Res.*, *102*, 21,825–21,835, 1997.

Yang, P., B. A. Baum, A. J. Heymsfield, Y. X. Hu, H.-L. Huang, S.-C. Tsay, and S. Ackerman, Single-scattering properties of droxtals, *J. Quant. Spectrosc. Radiat. Transfer*, *79*, 1159–1169, 2003.

Yang, P., L. Zhang, S. Nasiri, B. A. Baum, H.-L. Huang, M. King, and S. Platnick, Differences between collection 4 and 5 MODIS ice cloud optical/microphysical products and their impact on radiative forcing simulations., *IEEE Trans. Geosci. Remote Sens.*, *45*, 2886–2899, 2007.

Zemax, *Optical Design Program User's Manual*, 2009.

Zhang, M., R. D. Cess, and X. Jing, Concerning the interpretation of enhanced cloud shortwave absorption using monthly-mean Earth Radiation Budget Experiment/-Global Energy Balance Archive measurement, *J. Geophys. Res.*, *102*, 25,899–25,905, 1997.